POLITECNICO
MILANO 1863

Department of Physics
Doctoral Programme in Physics
XXX cycle

Femtosecond optically-triggered phenomena in layered metal-chalcogenide systems

Supervisor: Dr. Ettore CARPENE
Tutor: Prof. Dr. Claudia DALLERA
Coordinator: Prof. Dr. Paola TARONI

Doctoral dissertation of:
Davide BUGINI

XXX cycle

Femtosecond optically-triggered phenomena in layered metal-chalcogenide systems

Davide Bugini

Doctoral Programme in Physics, XXX cycle

To mo cuisle

Spin,spin
spin the black circle

Spin the black circle
from Vitalogy (1994), Pearl Jam

Ma guardate l'idrogeno tacere nel mare
Guardate l'ossigeno al suo fianco dormire
Soltanto una legge che io riesco a capire
Ha potuto sposarli senza farli scoppiare
Soltanto la legge che io riesco a capire

Un chimico
from Non al denaro
non all'amore
né al cielo (1971),
F. De André

Contents

Introduction

The down-sizing of electronic devices has almost reached the nanoscale, in which quantum phenomena play a fundamental role. From this perspective, material scientists and condensed matter physicists have dedicated large attention to low dimensional materials, ideal platform for possible applications in novel nanoscale quantum devices.
Layered metal chalcogenide systems are paradigmatic two-dimensional materials exhibiting peculiar electronic and magnetic properties driven by the anisotropy of the orbital bonds. Due to their reduced dimensionality, novel exotic phenomena arise in these layered compounds [1]. The discovery of the charge and spin density waves, of the puzzling high-Tc superconductivity and more recently of the topological insulating phase of matter are paradigmatic examples of the astonishing novel phenomena established in the last years in these compounds. Such exotic properties combined with their natural proclivity towards chip integration have established these materials as a promising platform for fundamental investigations and future devices.
In order to pursue integration in future technologies, a comprehensive understanding of the dynamical properties of these materials is essential. In the last decades, the emergence of mode-locked femtosecond pulsed lasers has triggered the development of new techniques to study the ultrafast electronic dynamics offering the opportunity to unfold opened questions about the light-matter interaction phenomena.
In this thesis, we have exploited high-temporal resolution time-resolved reflectivity (TR-Reflectivity) and time- and angle-resolved photoemission spectroscopy (TR-ARPES) to investigate ultrafast phenomena in two different classes of layered metal chalcogenides: (i) the topological insulators of the $Bi_xSb_{2-x}Te_ySe_{3-y}$ family and (ii) the charge density wave system 1T-$TiSe_2$. In particular, TR-ARPES measurements have been done using state-of-art Yb-based laser setup at the Ultrafast Photoemission and Optical Spectroscopy

(UPhOS) laboratory in the Physics Department of Politecnico di Milano [2]. Thanks to a cascade of non-linear optics processes (e.g. home-made Non-collinear Optical Parametric Amplifier (NOPA) and Sum Frequency Generation (SFG) stage), a sub 30 fs 1.8 eV pump beam and a sub 70 fs 6 eV probe beam are generated. Photoemitted electrons have been collected by a home-designed Time of Flight (ToF) analyzer. The resulting unique combination of temporal and energy resolution, 70 fs and 50 meV respectively, allowed us to address the physical origin of femtosecond optically-triggered phenomena in layered low dimensional materials.

Topological Insulators are a phase of matter characterized by an in-plane spin-polarized surface state (TSS) arising within the bulk insulating energy gap [3–5]. Electrons in the TSS are well described by the Dirac Hamiltonian and form a Dirac cone in reciprocal space. This leads to peculiar properties like the protection against spin-flip events [3, 4]. The capability to control the spin polarization using ultrashort light pulses [6, 7] together with the realization of an optically-triggered surface spin-current [8] opens new scenarios in the use of this class of materials for future opto-spintronic devices. Thus, TIs have become a hot-topic in the scientific community since they promise a new generation of faster devices. We deeply investigated the out-of-equilibrium properties of the $Bi_xSb_{2-x}Te_ySe_{3-y}$ topological insulator necessary for its sucessful implementation in spintronic devices.
Performing TR-ARPES measurements as a function of the stoichiometry, we have found that the position of the Dirac point (DP), i.e. the point in which the two branches of the Dirac cone cross, with respect to the Fermi level strongly affects the electronic relaxation dynamics of the Dirac fermions in the TSS. We have explained our observation in terms of Fermi's golden rule and bottleneck-effect due to the reduced phase space at DP. In particular, for stoichiometries where the Dirac point has a vanishing binding energy, we have observed a terrific long persistence of the electronic population in the TSS [9].
Exploiting the selective coupling of different circular helicities of light with spin in the presence of a non-zero spin-orbit interaction, we have investigated the microscopic origin of the spin-current that is optically-induced by circularly-polarized light in the Bi_2Se_3 prototypical topological insulator. We reported the first experimental evidence of a direct coupling between circular light and the empty topological surface state (ESS) located within a bulk-gap of the unoccupied states. We reported also the ultrafast build-up and flow of a spin-polarized electron population in the ESS [10, 11].
Combining TR-ARPES measurements performed at the University of British Columbia by prof. Damascelli's group and high-temporal resolution broad-

band TR-reflectivity measurements performed in Politecnico di Milano, we observed that a modification of the TSS wavefunction, as a consequence of optically-triggered phonon modes, leads to transient changes in the photoemission matrix elements. This is an important result because it raises doubts about the commonly-employed paradigm that the transient evolution of the TR-ARPES intensity is related directly to the intrinsic quasiparticle dynamics suggesting that a more careful interpretation of the non-trivial time-resolved photocurrent is required [12].

In the last decade, the discovery of Graphene boosted research in the field of low-dimensional materials. However, despite peculiar properties (such as the very high carrier mobility), the lack of a band-gap, fundamental for any operative electronics device, is a limiting factor in the implementation of Graphene. For this reason, low-dimensional materials exhibiting a metal-to-insulator transition attracted a lot of attentions in the material science community.
The layered 1T-$TiSe_2$ is an appealing system due to the experimental observation of a novel quantum state of matter: the excitonium, a macroscopic condensate of excitons, quasiparticles made by interacting electrons and holes [13].
In addition, 1T-$TiSe_2$ undergoes a (semi)metal-to-insulator transition below the critical temperature T_{CDW}=202 K driven by the formation of low energy excitation called charge density wave (CDW) together with a periodic lattice distortion [14]. Although this transition is well-known since the 70s, the underlying mechanism is not well-established and understood.
We investigated the photo-induced melting of CDW in 1T-TiSe2 single crystals by TR-ARPES and TR-Reflectivity. Our measurements reveal that after photo-excitation different dynamics arise in the closing of the electronic band-gap and in the melting of the charge order suggesting an excitonic-lattice cooperative model [15].

This thesis is organized as follow.
In Chapter 1 we present an overview of the properties of three-dimensional topological insulators. The state-of-art based on steady-state ARPES, circular dichroism and TR-ARPES experiments is discussed.

In Chapter 2, after a theoretical introduction about Charge Density Waves, we introduce the physics of the layered 1T-$TiSe_2$ system with particular attention to previous ARPES and TR-ARPES experiments.

In Chapter 3, we introduce the experimental techniques employed in this

thesis. After a theoretical introduction about the photoemission process, we present the time- and angle-resolved spectroscopies (TR-ARPES).

In Chapter 4, we show and discuss our data about out-of-equilibrium phenomena in topological insulators. In particular, we present our TR-ARPES as a function of stoichiometry in the $Bi_xSb_{2-x}Te_ySe_{3-y}$ family, the origin of the optically-induced spin-current in Bi_2Se_3 and the dynamical modification of the photoemission matrix elements.

In Chapter 5, we discuss the origin of the charge density waves phase in layered 1T-$TiSe_2$. Our fluence-dependence TR-ARPES and TR-Reflectivity measurements strongly hint to the key role played by the lattice in the (semi)metal-to-insulator transition suggesting a cooperative excitonic-lattice scenario.

Chapter 1

Topological Insulators

To send out a flare
This is an attempt to connect
Edify and dissect
Send a light
Send repair
From surface to air

From surface to air
from If Not Now, When? (2011), Incubus

Since their prediction and experimental discovery in 2009, topological insulators (TIs) created a large surge of research activities. Their peculiar properties such as a spin-polarized metallic transport at the surface suggest in fact possible spintronics applications. In addition, they are also ideal benchmark for quantum theories such as the realization of Majorana fermions. In the following chapter a review of the physics and of the properties of topological insulators will be presented. Particular attention will be given to angle-resolved photoemission spectroscopy (ARPES) experiments that characterized TIs properties. In addition, a state-of-art overview about out of equilibrium physics of TIs investigated by time-resolved ARPES will be given.

1.1 Introduction

Three dimensional topological insulators (TIs) represent a novel phase of condensed matter presenting unique quantum-mechanical properties. This class of materials is characterized by a bulk insulating behavior while the

surface is metallic due to the presence of a gapless surface state (the so-called topological surface state (TSS)) within the bulk insulating band gap. The mechanism at the origin of the TSS is the band inversion that consists in the reversal of the common band ordering of the bulk valence (VB) and conduction bands (CB) at the $\bar{\Gamma}$ point, i.e. the center of the Brillouin zone, due to a strong spin-orbit coupling (SOC) [3–5, 16]. To better clarify this mechanism, in the following discussion we focus on Bi_2Se_3, the prototypical three-dimensional TI. However, the derived properties and conclusions can be applied to all TIs.

The crystal structure of Bi_2Se_3 is shown in Fig. 1.1(a). Bi_2Se_3 has a rhombohedral structure consisting of five atomic layers stacked along the z-direction. This structure, usually called quintuple layer (QL), could be considered the fundamental brick of any three dimensional topological insulator. Inside a QL, strong chemical bonds couple an atomic layer to the first nearest neighbours. Between two different QLs instead the force is weaker and of Van der Waals type giving a natural cleavage plane. Starting from this crystal structure, the fundamental role of the SOC in the band structure could be clarified by considering the contribution of the Bi and Se orbitals to the VB and CB at the $\bar{\Gamma}$ point as shown in Fig. 1.1(b). Three different stages are considered: (I) is the largest energy scale representing the chemical bonds among Bi and Se atoms inside a QL, (II) includes the crystal field splitting and (III) represents the relativistic correction within the spin-orbit coupling. In (I), the formation of chemical bonds drops all the Se-states below the Fermi level while the Bi-states are shfted up above it. Thus, labeling the states according to their parity (labeled as $\pm$), conduction bands derive from two Bi p-orbitals and valence bands consists of three Se p-orbitals. The crystal field removes degeneracy of p_z orbitals from $p_{x,y}$ (stage (II) in Fig. 1.1b); the p_z orbitals are now the closest ones to the Fermi level. Turning on SOC (stage (III)), it leads to a repulsion between states with the same parity but opposite spin and angular momentum character. The energy of the Se-p_z state is then lifted above the Fermi level while the energy of the p_z state of the Bi atoms is pushed down [3, 17]. Due to this inversion of the usual order, a metallic surface state necessarily appears to connect the state with the same parity at the interface with an ordinary insulator (e.g. the vacuum) with the trivial band order as shown in Fig. 1.1(c)
This mechanism infers the role of the topology of the electronic states wave functions and it is the reason why this new class of materials has been labeled as *topological*. Without going deep in details, in TIs the wave function is mapping the **k**-space in a *manifold* of the Hilbert space with a non trivial topology due to the band inversion mechanism. This nontrivial topology

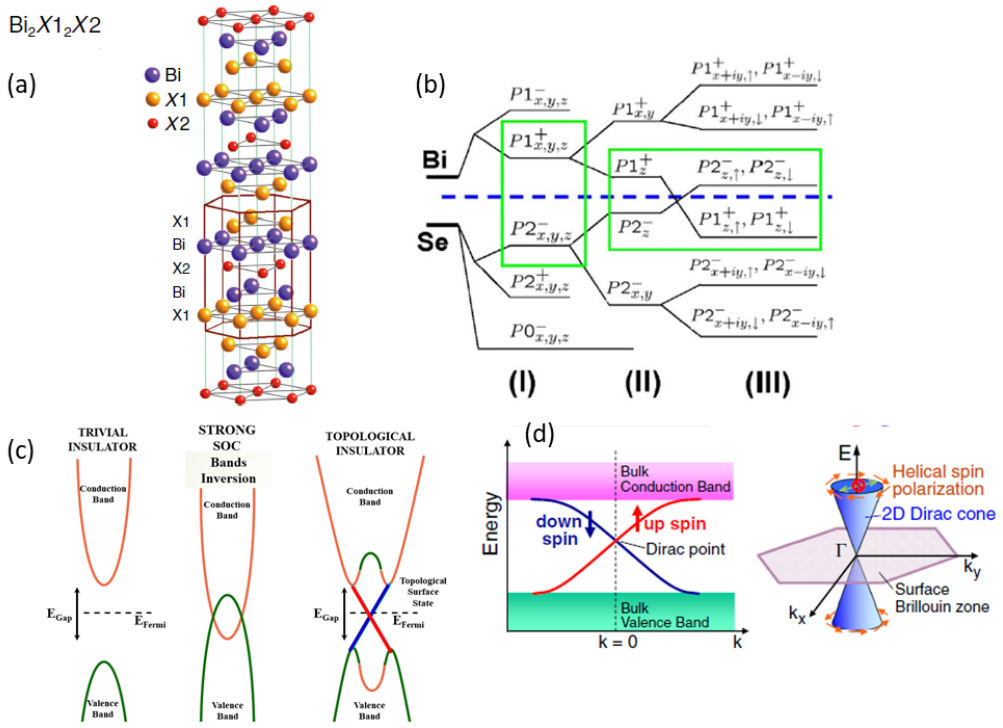

Fig. 1.1: (a) Crystal structure of topological insulator bismuth-chalcogenide family. The brown cage encloses the quintuple layer (QL). From [4]. (b) Schematic picture of the evolution of Bi and Se orbitals into valence and conduction bands of Bi_2Se_3 at the $\bar{\Gamma}$-point. (I), (II) and (III) stand for different stages in which chemical bonding, crystal field splitting and spin-orbit coupling, respectively are turned on. The blue dashed line represents the Fermi level. From [3]. (c) Cartoon of the band structure evolution from trivial to topological insulator trough band-inversion mechanism due to strong spin-orbit coupling (SOC). (d) Pictorial representantion of the band dispersion of the spin-polarized bidimensional Dirac cone within the bulk energy band gap. The helical spin texture is also reported. From [4] (c) (2013) The Physical Society of Japan.

is peculiar of the gapped energy states. This implies that topology cannot change while the bands energy gap is open. Therefore, at the interface the topology can turn to the trivial one of a common insulator only by closing the gap [4]. Topology shapes the rising of the gapless surface state. Surface state fundamental properties do not depend on the material parameters but only on the topology of the gapped bulk electronic states. In other words, smooth adiabatical changes in the physical parameters of the material do not

affect the fundamental properties unless the system passes through a quantum phase transition [5].
As previously described, it is the physics around the $\bar{\Gamma}$ point that determines the topological nature. It is possible to show that, starting from the p_z-states around the Fermi level (see Figure 1.1(b)), the effective Hamiltonian ruling the low energy properties of the system is close to the three-dimensional Dirac model except for the fact that the mass term is in this case **k**-dependent and proportional to the bulk energy gap. The Hamiltonian describing the topological surface state (TSS) is obtained taking the projection of the bulk Dirac-like one onto the surface. The surface Hamiltonian H_{surf} is [3]:

$$H_{surf}(k_x, k_y) = C + v\hbar(\sigma^x k_y - \sigma^y k_x), \tag{1.1}$$

where v is the group velocity of the surface state and σ^x, σ^y are the in-plane Pauli matrices. Equation 1.1 points out other novel properties of the TSS. Firstly, the gapless surface states within the bulk band energy gap have been found in a single massless Dirac fermion. For this reason, TSS forms the so-called Dirac cone. Then, the Pauli σ matrix represents the spin of the electrons [18]. Thus, according to eq. 1.1, the spin of the electron in the TSS is locked to be orthogonal to theo crystal momentum **k**, i.e. the surface Dirac fermion is helical. Looking from the surface normal, the upper (lower) part of the Dirac cone is characterized by a left-hand (right-hand) helicity (Fig. 1.1(d)). In other words, at a given energy, counter-propagating electrons have opposite spin. This implies that any charge current at the surface of TIs is also a spin-polarized current. In addition, the spin polarization of the TSS is extremely robust since the helicity of the TSS prevents the backscattering events. Electrons with opposite momentum should have opposite spin. Thus, an electron that is moving forward cannot be scattered in the opposite direction without a spin-flip event [4, 19]. The spin-polarization of the metallic surface state of TIs attracts the large interest of the materials science community. TIs are promising platform for the realization of room temperature operative spintronics devices.
It is well-known that symmetry plays a fundamental role in solid state physics defining the materials properties and TIs are no exception. Without any magnetic field, time reversal symmetry (TRS) is present. Then, Kramers' degeneracy occurs: electronic eigenstates at opposite momenta **k** and $-\mathbf{k}$ must have the same energy $E(\mathbf{k})$ [20]. At the time-reversal-invariant points of the Brillouin zone, such as $\bar{\Gamma}$ point, two surface states forming a Kramers' pair should cross each other. This degeneracy point is usually called Dirac point since it represents the point of contact between the conic structures of the TSS. The TSS cannot be gapped, i.e. Kramers' degeneracy cannot be removed, as long as TRS is present. This discloses the topological protection

of the gapless surface state by time-reversal symmetry. Three-dimensional TI cannot be adiabatically deformed into an ordinary insulator by nonmagnetic impurities or disorder, i.e. without breaking TRS [21]. We have described the

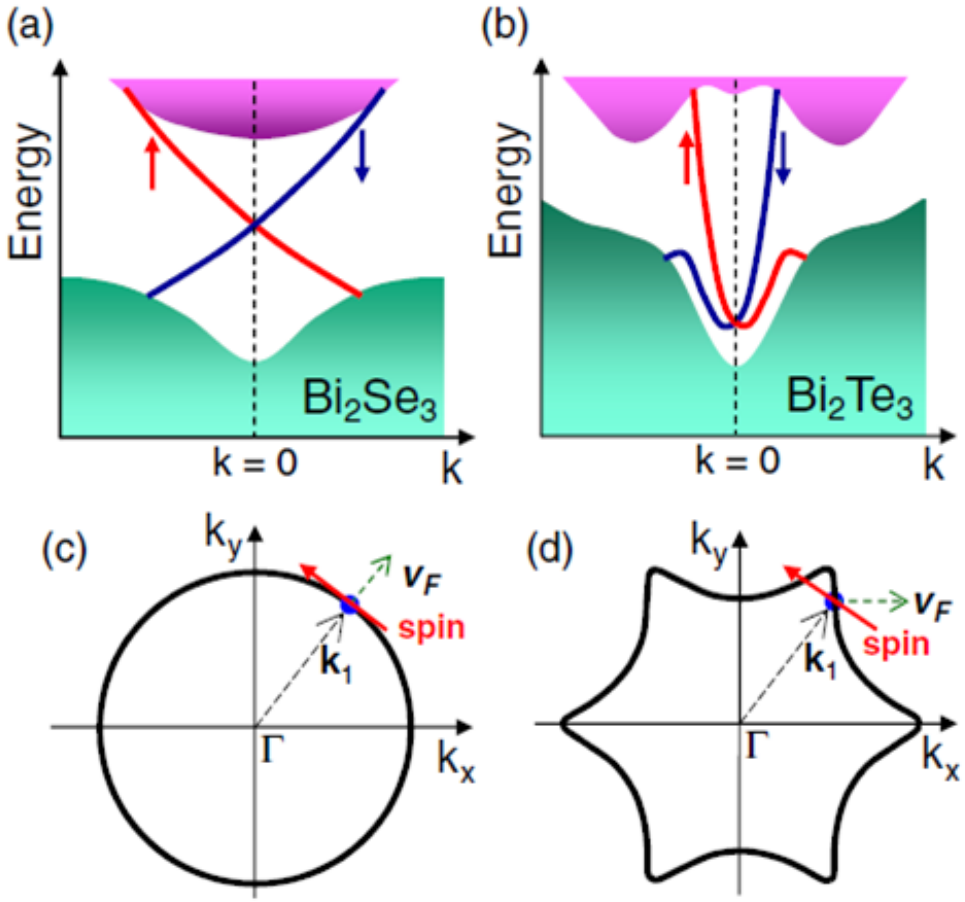

Fig. 1.2: Schematic band structure of (a) Bi_2Se_3 and (b) Bi_2Te_3. The spin polarization of the topological surface state within the bulk gap is reported. Costant energy cuts of the Dirac cone for (c) Bi_2Se_3 and (d) Bi_2Te_3. The strong reshaping due to the hexagonal warping in (d) is evident. Notice that the spin vector (red arrow) is always perprendicular to the momentum vector $\mathbf{k}_1$ while the Fermi velocity (green dashed arrow) can be non-orthogonal in presence of hexagonal warping. From [4] (c) (2013) The Physical Society of Japan.

existence of the TSS and its properties for Bi_2Se_3 but it is possible to extend them to all the parent compounds of the Bi_2Se_3 family, such as Bi_2Te_3 and

Sb_2Te_3. However, higher order in $\mathbf{k}$ corrections of the surface hamiltonian 1.1 should be taken into account [3]. To cubic order, continuous rotational symmetry around the z-axis is broken by additional terms due to Dresselhaus SOC Hamiltonian at the surface of rhombohedral structures [3, 4]. The resulting symmetry is a discrete three-fold rotation symmetry that resembles the crystal potential. According to the new symmetry, the Fermi surface loses its circular shape, as in the case of Bi_2Se_3, to become hexagonally warped (see Fig. 1.2) [22]. The hexagonal warping leads to peculiar physical properties. As shown in Fig. 1.2(d), the spin vector can now be non-orthogonal to the Fermi velocity $\mathbf{v_f}$ giving rise to strong quasi-particle interference [23, 24]. In addition, a finite out-of-plane component of the spin texture of the Dirac cone emerges [25].
All topological insulators properties previously deduced (such as the presence of a metallic linear dispersing surface state within the bulk energy band gap, its spin polarization and robustness, the effect of the hexagonal warping) have been experimentally verified by angle-resolved photoelectron spectroscopy measurements as shown in the next section.

1.2 Angle-resolved photoemission spectroscopy on topological insulators

Angle-resolved photoemission spectroscopy (ARPES) (for more details see Chapter 3) offers the unique capability to map the electronic band structure of solid crystals. For these reasons, ARPES has been the favorite tool to investigate the topological nature and the properties of three-dimensional TIs. In this section, we will provide a short review of the cornerstone ARPES experiments on TIs.

Figure 1.3(a) reports one of the first high-resolution ARPES maps of Bi_2Se_3 that evidences a remarkably simple TSS spectrum with a single Dirac cone located at the $\bar{\Gamma}$ point and a large bulk band gap, in agreement with theoretical predictions [27]. These measurements along $\overline{\Gamma M}$ and $\overline{\Gamma K}$, high symmetry directions of the surface projected Brillouin zone (marked in Fig. 1.3(b)), show how the bulk contributions change while the shape of the TSS remains the same hinting to a circular surface map proper of a cone (see onset of Fig. 1.3(c)). Figure 1.3(c) reports the in-plane component of the spin polarization along the $\overline{\Gamma M}$ direction measured by spin-resolved ARPES. For opposite $\mathbf{k}$, the spin polarization is opposite confirming the helical nature of

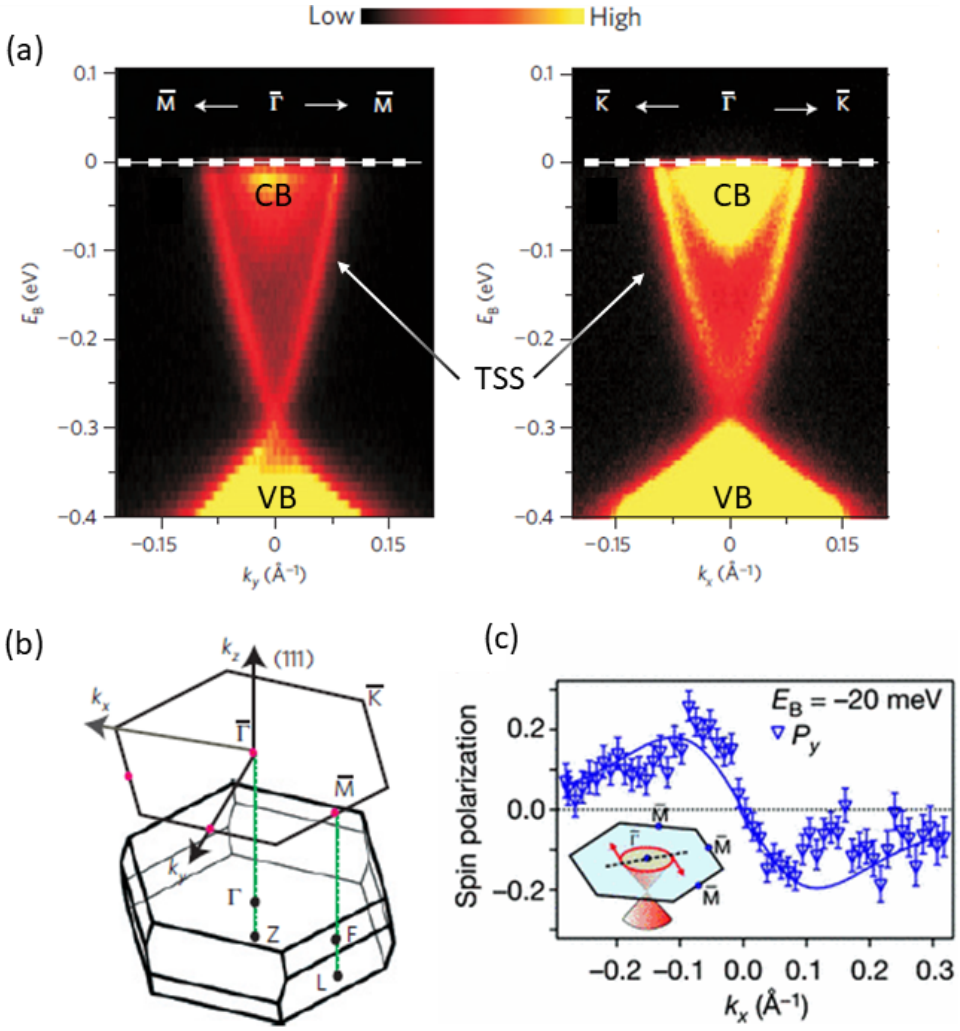

Fig. 1.3: ARPES data for the dispersion of the surface state of Bi_2Se_3 from [26] , along directions (a) $\overline{\Gamma M}$ and (b) $\overline{\Gamma K}$ of the (c) surface projected Brillouin zone [26]. The dashed white line refers to the Fermi level. VB: bulk valence band, CB: bulk conduction band and TSS: topological surface state. (d) Spin-resolved Arpes data along $\overline{\Gamma M}$ direction for a fixed energy. From [27].

the spin-polarized TSS. In addition, photon-energy dependent ARPES measurements (Fig. 1.4) show no dispersion associated with the TSS confirming the surface nature of this state [28].

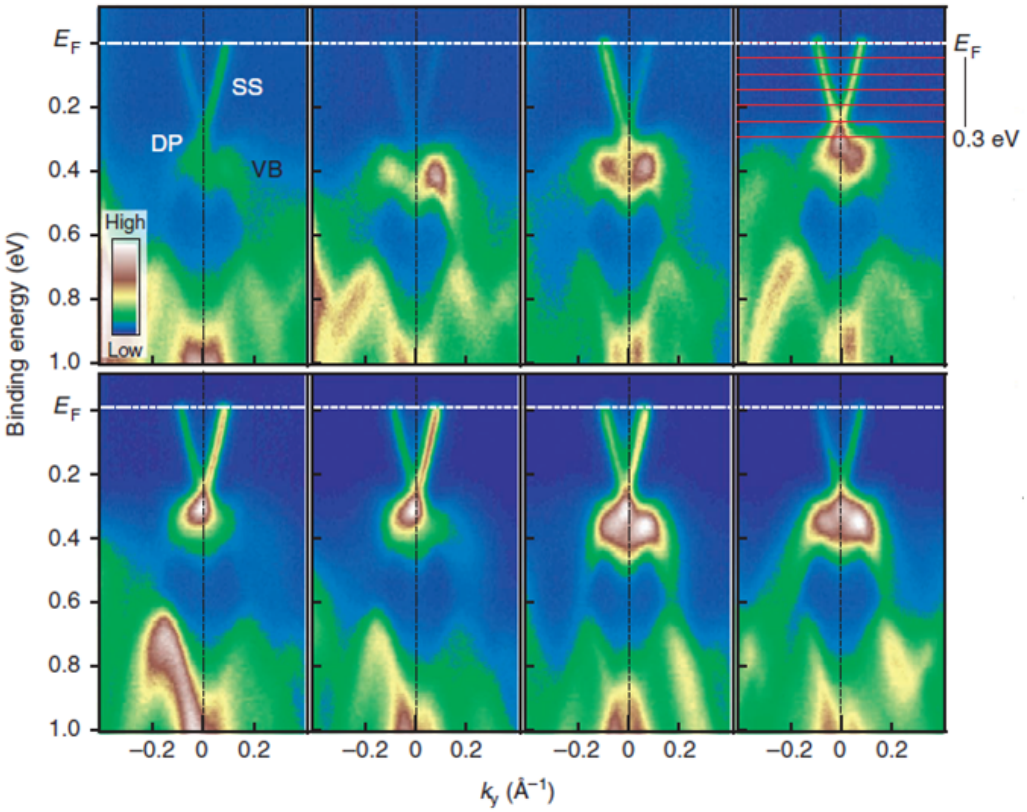

Fig. 1.4: Photon energy dependence of the ARPES intensity around the $\bar{\Gamma}$-point for Bi_2Te_2Se measured at $h\nu$=46, 50, 54 and 58 eV (top row) and 62, 66, 70 and 74 eV (bottom row) at T=30 K. White dashed lines stand for the Fermi level E_F. VB: bulk valence band, SS: topological surface state. DP: Dirac point. From [28]

As seen in the previous section, the circular costant energy cut of the Dirac cone could be distorted in an hexagonal shape. This effect, know as hexagonal warping, becomes relevant in the presence of a strong lattice potential and a small band gap such as in Bi_2Te_3 and Sb_2Te_3. Figure 1.5(c) reports ARPES measurements on Bi_2Te_3 confirming the distortion of the Fermi surface. In addition, spin-resolved ARPES data confirm the prediction that the helical spin-texture of the Dirac cone is modified in the presence of hexagonal warping. Figures 1.5(c) and 1.5(d) show the in-plane and the out-of-plane spin polarization along the $\overline{\Gamma K}$ direction for the TSS of $TlBiSe_2$, a non-warped TI (see Fig. 1.5(a)), and Bi_2Te_3, respectively. While the in-plane polarization is present in both compounds, a non-negligible out-of-plane component exists only in the hexagonally warped Bi_2Te_3 [22, 25]. Moreover, from point A to

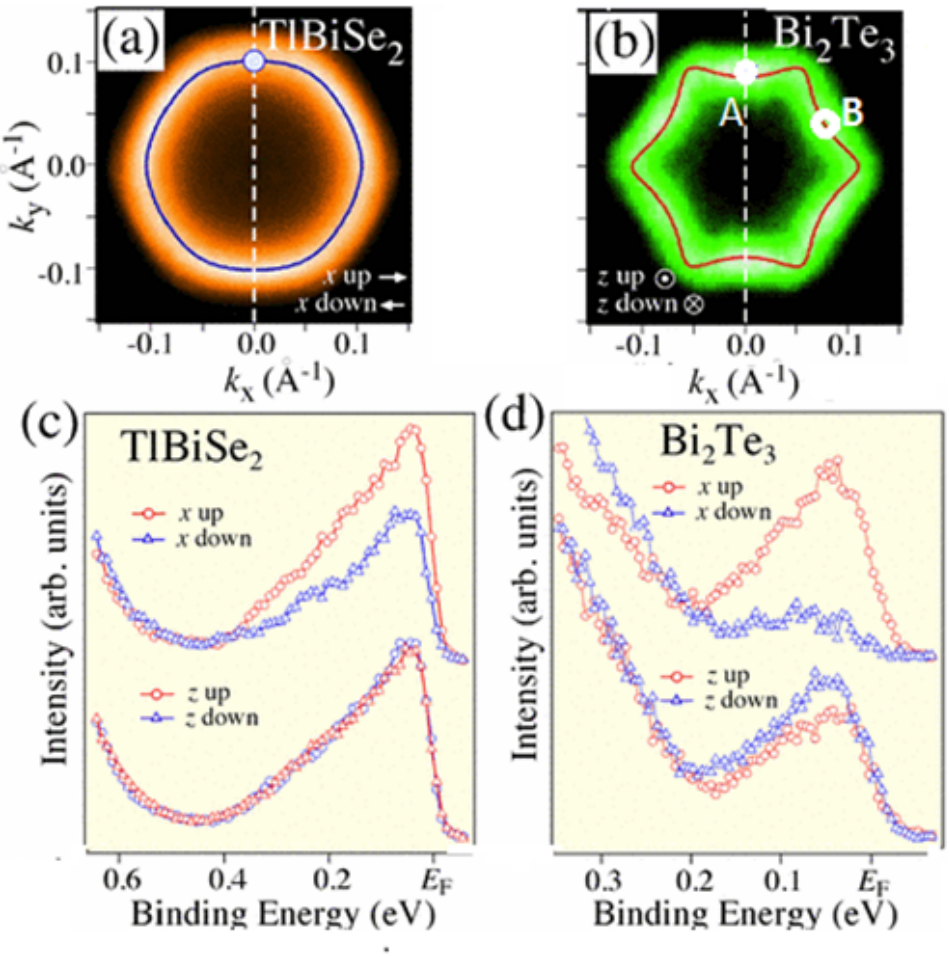

Fig. 1.5: Comparison between Fermi surface of (a) $TlBiSe_2$ and (b) Bi_2Te_3; the solid lines are the simulated Fermi surface using the theory in Ref. [22]. Spin-resolved EDCs measured along the $\overline{\Gamma K}$ direction for (c) $TlBiSe_2$ and (d) Bi_2Te_3; z marks the out-of-plane component. From [29].

point B in Fig. 1.5(b) the out-of-plane relative intensity of spin up and down reverses indicating that the overall spin texture is affected by the hexagonal symmetry.

ARPES measurements help characterize the fundamental role played by the quintuple layer (QL) structure. Linear polarization-dependent ARPES measurements suggest a complex orbital structure of the Dirac cone and a non-trivial interplay between the layers inside a QL in the interaction with the light [7, 30–32]. In the previous section we have shown that bulk and surface

states around the Fermi level have mainly a p-orbital character: being z the out-of-plane axis, the crystal field energetically separates the in-plane orbital component $p_{x,y}$ from the out-of-plane p_z. Then, SOC operates the parity band inversion leading to the formation of the TSS. In reality this picture is oversimplified. The TSS exhibits in fact a strong orbital-dependent spin texture characterized by a large p_z component but also by a non-negligible $p_{x,y}$ contribution. This has been demonstrated on Bi_2Se_3 observing the variation of the ARPES intensity upon changing the polarization of light. The ARPES intensity depends on matrix elements related to the polarization of the impinging photon (as described in Chapter 3). Intensity variations due to changes of the polarization of light reflect the symmetry properties of the system. Fig. 1.6(c) shows constant energy cuts of Bi_2Se_3 for different energies referred to the Dirac point (left to right). The bottom row shows data taken with p-polarization that mainly probes the p_z orbital states; the upper row shows data with s-polarization, mainly sensitive to in-plane components. The p-polarized light contours are almost uniform for all energy cuts. In contrast, with s-polarization we have drastic intensity variations around the constant energy maps. In particular, above the Dirac point a vanishing spectral weight *parallel* to the electric field is clearly evident, while a suppressed spectral weight *normal* to the electric field is shown in the data below the Dirac point. The sample crystalline axes is rotated while keeping all other experimental parameters identical to identify wether spectral weight variation depends on the specific crystalline orientation or on the photon field. Rotating the sample, the probed crystallographic direction changes while the polarized light in the plane of incidence (s-polarization) remains unchanged. In Fig. 1.6(a) the cuts at a fixed energy are shown as function of sample rotation angles (rows) and energy of the DP (columns). There is no dependence on the sixfold crystalline structure since the costant-energy cuts are the same for any rotated direction. Then, the observed ARPES intensity modulation is due to the light-interaction geometry and, as a consequence, to the symmetry of the in-plane orbitals. A different texture for the in-plane $p_{x,y}$-orbitals component above and below the Dirac point is observed. In particular, below the Dirac point the orbital texture is radial while above it is tangential as depicted in Fig. 1.6(b) [31].

There is the experimental evidence that the wave-function of TSS is not localized only at the surface but it has a deep extension into the bulk for several atomic layers (2 nm) without dispersion [32]. This extension, in concert with strong SOC, gives rise to a layer-dependent structure: the p_z orbitals at the surface give the same contribution for each layer while the $p_{x,y}$ gives a contribution that is strongly layer-dependent as shown in Fig. 1.6(d),(e)

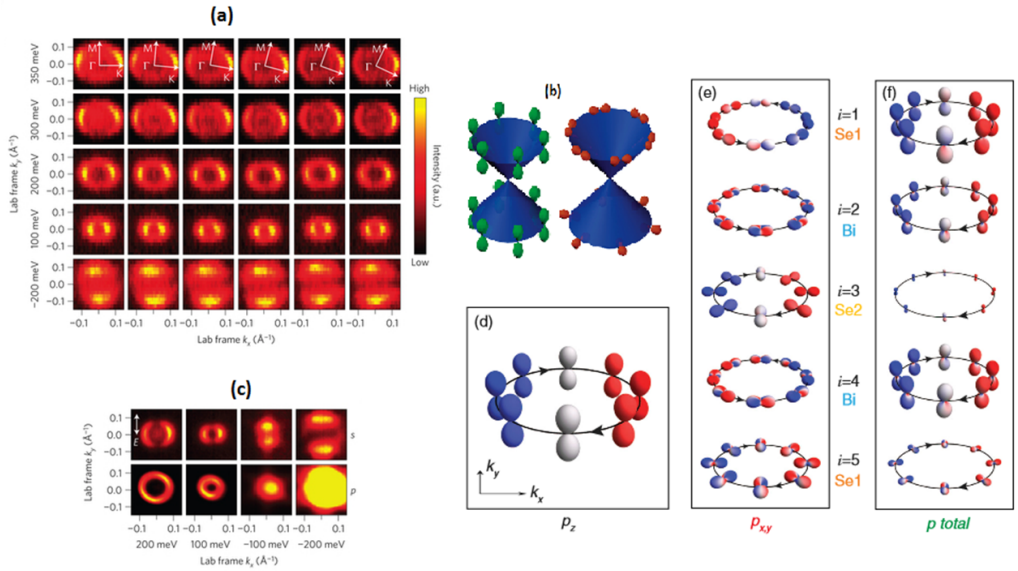

Fig. 1.6: (a) Bi_2Se_3 Dirac cone measured by s-polarized light. Costant energy surface are measured with polarized light in the plane of incidence; angle of incidence 7°. The sample is rotated by step of 5° showing that the detected pattern does not change. (b) Pictorial draw of the p-orbitals contribution to the Dirac cone deduced by ARPES spectra with different polarization(c). In (c) the upper row shows ARPES with s-light, more sensitive to in-plane components. The bottom row shows ARPES data from p-polarization, sensitive to out-of-plane component. In (d) the in-plane orbitals structure (red) changing from radial to tangential passing through the Dirac point while the out-of-plane component (green) stills invariated. From [31] (d)(f) Layer- and orbital-projected charge density. The total layer-resolved SS texture (f) is obtained by adding the out-of-plane (d) and the in plane (e) layer-depent contributs. From [32].

[32]. The final structure (f) has mainly out-of-plane character, with different magnitude of the orbitals layer by layer, and an in-plane radial configuration in the last layer of the QL. Due to this TSS layer-dependent spin-orbital entanglement, surface state electrons photoemitted from different layers interfere: this introduces a k_z dependence in the ARPES matrix element that changes the detected intensity for opposite $\mathbf{k}_{||}$. This effect explains the $\mathbf{k}_{||}$ asymmetry shown by ARPES maps of the TSS (see for example lower row of Fig. 1.4) apparently in violation of Kramers' degeneracy i.e. with a breaking of TRS. In addition, recent linear-dichroism ARPES experiments carried on the septuple layer $GeBi_2Te_4$ shows the inversion of the parity of bulk valence

and conduction bands confirming the theoretical prediction [33].
In the previous section we stated that TSS is protected by time-reversal symmetry i.e. alterations of the surface cannot lift the degeneracy at the $\bar{\Gamma}$ point and open a gap in the gapless TSS. The surface could be altered by exposition to air, with ionic sputtering or depositing alkali elements such as K, Ca, NO_2 [34–36]. ARPES experiments conducted in these conditions always showed the presence of TSS confirming the robustness of this state under non-magnetic perturbation. However, since the TSS is spin-polarized, it is extremely interesting to study the coupling with a ferromagnet in view of a possible spin-manipulation in a spintronic device. Iron adatoms deposition has been found to open a gap in the Dirac cone [37]. Other works [38, 39] did not attribute the opening of an energy gap in the topological surface state to magnetic impurities (Fig.(b)) suggesting that if the magnetization of Fe is within the surface plane, TRS is not broken. In this configuration the perturbation can only shift the Dirac point away from $\bar{\Gamma}$ and change the doping of the bulk. This robustness is the precondition for the effective spin manipulation in a spintronic device. However, the question about the robustness of TSS in presence of magnetic interactions is still unanswered and further investigation are needed to fully understand the effect of ferromagnetic materials at the topological insulator interface and then the capability to manipulate the spin in future applications.

We will focus now on the suitable characteristics required for operating application of TIs in devices. Elastic backscattering protection due to the helical texture of the TSS and its robustness under non-magnetic impurities ensures the required crucial spin coherence needed for application. However, at finite temperature electron-phonon interaction could largely increase the resistivity (as in metals). It is well know that phonons could also drive the system to novel symmetry-broken ground states such as superconductivity and charge-density-waves system (discussed in details in the next Chapter). Bi_2Se_3 and Bi_2Te_3 have been found to become superconductors under Cu-doping or pressure action due to the strong interaction of the TSS with bulk band phonons [40–42]. Then, the role of electron-phonon coupling in real operative devices is crucial. High-resolution ARPES measurements conducted as a function of temperature found an extremely weak broadening of the TSS and the absence of any anomaly in the band dispersion suggesting an extremely weak electron-phonon coupling [43]. These data ensure the capability to exploit TIs for room-temperature spintronics.
In order to exploit the spin-current due to the spin-polarization of the surface carriers in the Dirac cone, helical Dirac fermions should dominate the transport. Unfortunately, binary stoichiometric compounds such as Bi_2Se_3 and Bi_2Te_3 do not show the desired high insulating bulk due to defects nat-

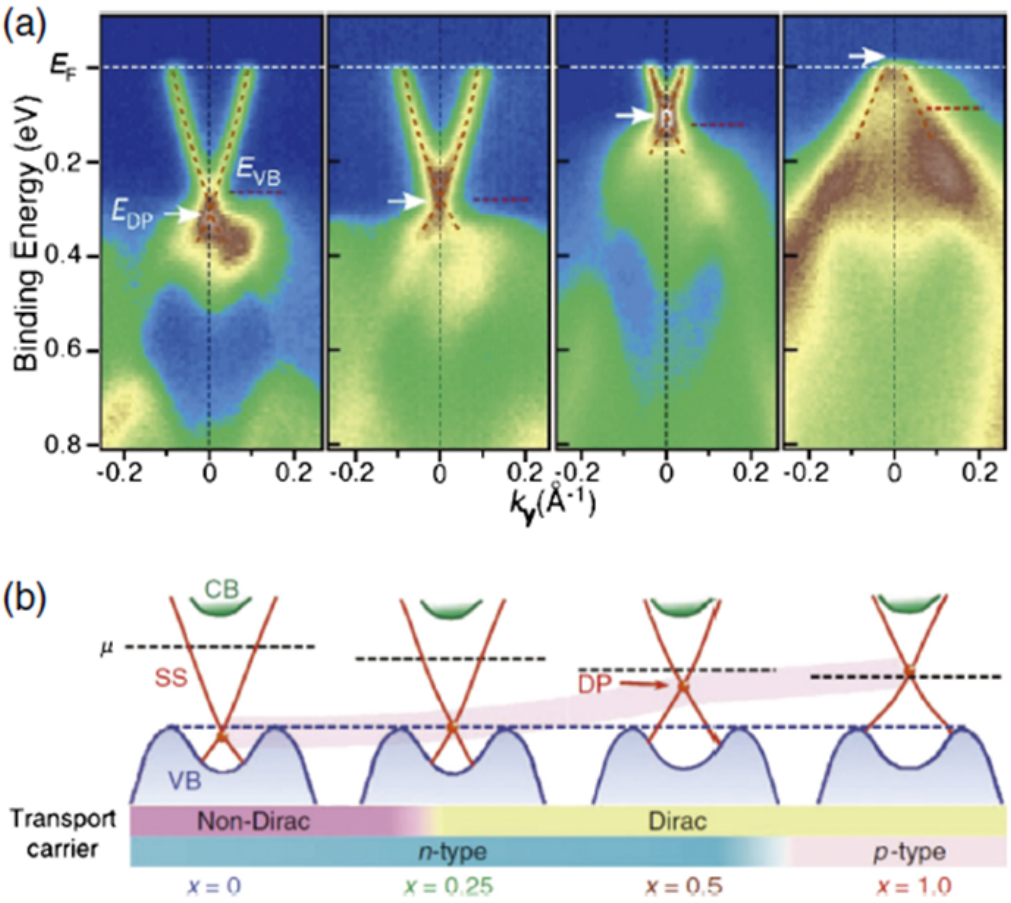

Fig. 1.7: (a) Comparison of band dispersions in $Bi_{2-x}Sb_xTe_ySe_{3-y}$ (BSTS) for four x values (x=0, 0.25, 0.5 and 1.0) where y=1, 1.15, 1.3 and 2, respectively. The ARPES data were measured with $h\nu$=58 eV at T=30 K. Brown dashed curves in (a) are guides to the eyes to trace the TSS. White arrows and red dashed lines indicate the energy positions of the Dirac point (E_{DP}) and the VB top (E_{VB}), respectively. (b) Schematic band diagram for changing x in BSTS derived from the (a). The top of the VB is aligned in this diagram for clarity. From [28].

urally occuring in the crystal growth that result in carrier doping. Then, bulk transport overhelms surface transport with the final loss of the spin-current. From this perspective, $Bi_{2-x}Sb_xTe_ySe_{3-y}$ (BSTS) has been found of great interest since particular x ad y combinations yield a large bulk resistivity suppressing bulk-transport [44]. Moreover, ARPES measurements on samples of different stochiometries (see Fig. 1.7) have shown the possibility

to tune the position of the Dirac point within the band gap maintening the large bulk resistivity [28]. This observation makes the BSTS family of fundamental importance for engineering of surface carriers properties (e.g. sign, density) without any requirement for tuning the bulk chemical potential, i.e. preserving the large insulating bulk nature.
We have shown how polarized-light interacts in a non-trivial way with the TSS, allowing to understand its complex orbital texture. In particular, photoemitted electrons along a QL could interfere, giving rise to anomalies in the ARPES signal. Spin-resolved ARPES measurements have shown the capability to flip the spin of the photoemitted Dirac fermions changing the polarization of the light [6]. Necleting the spin direction of the Dirac fermion inside the crystal, polarized-light allows us to obtain the chosen spin-signal. The interference between layers in a QL has been found at the origin of this astonishing effect [7, 32]. This experiment clearly demonstrates the strong coupling between polarized light and spin emitted from TSS opening the way to opto-spintronics devices.

1.3 Circular-dichroism in photoemission on topological insulators

In the previous section we have already shown how linear dichroism in ARPES measurements can provide unique information about the orbital character and parity of the TSS in topological insulators [31–33]. Similarly, circular dichroism (CD) in ARPES experiments grants the access to peculiar properties of Dirac fermion: in particular, CD allows to map indirectly the spin polarization of the bands structure. In the following we will give a detailed description of this technique, including its criticities. A short review of the previous works on TIs involving circular-dichroism will also be listed.

As seen for the linear dichroism in the previous section, CD-ARPES is a technique that consists in the comparison of the photoemission signal intensity using the two helicities of circularly-polarized light (circular right (R), circular left (L)). Through spin-orbit coupling different circular helicities of light selectively couple with spin. In this way, CD allows us to reveal the presence of an order involving spin of the spin-polarized band structure. In a nutshell, a fixed circular polarization of the light (eg. R) can interact only with a certain spin direction (eg. spin up). Then, in photoemission, we detect only photoelectrons with a fixed spin. If the energy bands are not spin-polarized, the occupation number of electrons with spin up and spin

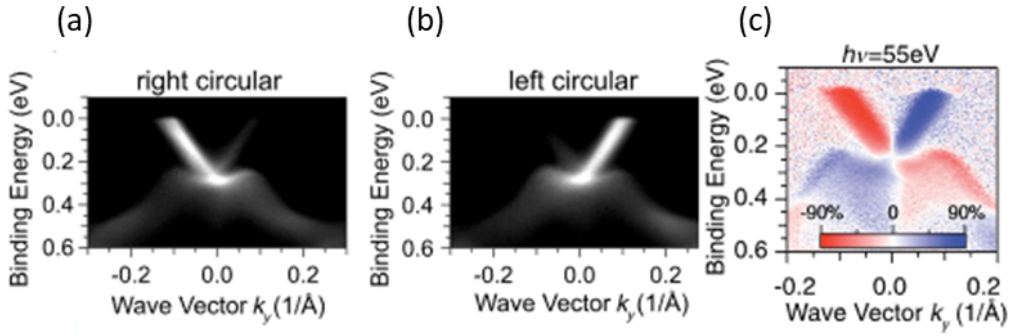

Fig. 1.8: Comparison between Bi_2Te_3 data along the $\overline{\Gamma K}$ direction photoemitted by (a) right- and (b) left-circularly polarized light of $h\nu$= 55 eV. (c) Dichroic asymmetry A between (a) and (b). From [45].

down is the same. Thus, the photocurrent emitted for R or L is identical. Instead, if some spin-order exists, the photoemission intensity obtained using a circular polarization of the light depends on the helicity given a non-zero spin-orbit coupling. Experimental evidence is shown in Fig.1.8(c),(d) compared to linearly polarized light ARPES (b). The spin-order is hidden in the unbalance between the photoemitted intensity with the two helicities of the light. The dichroic asymmetry (A), defined as

$$A = \frac{I_R - I_L}{I_R + I_L} \tag{1.2}$$

represents the weighted difference of the photoemission intensities with opposite light helicities. Then, computing A, as reported in Fig. 1.8(c), the order of spin in the sample is highlighted.
Recently, CD-ARPES has been exploited to investigate three-dimensional topological insulators [45–49] reporting an opposite value of the dichroic asymmetry for opposite crystal momenta in the TSS. This is consistent with the helical spin texture of the TSS already reported by spin-resolved ARPES. In particular, a CD-ARPES study with photon of 6.2 eV established a link between the dichroic signal and the spin and derived a vectorial mapping of the spin texture evidencing a small warping of the helical spin structure of the Dirac cone in Bi_2Se_3 [49]. According to this work, CD-ARPES can be used as a valuable alternative to spin-resolved ARPES. However, the interpretation of the CD signal in terms of spin-polarization is non-trivial and requires to pay attention. Angular momentum carried by circular light couples to the electronic spin through the SOC. As discussed in Section 1.1, SOC entangles spin and orbital momentum components. Then, the dichroic signal could

also be attributed to a local orbital-angular momentum [47].

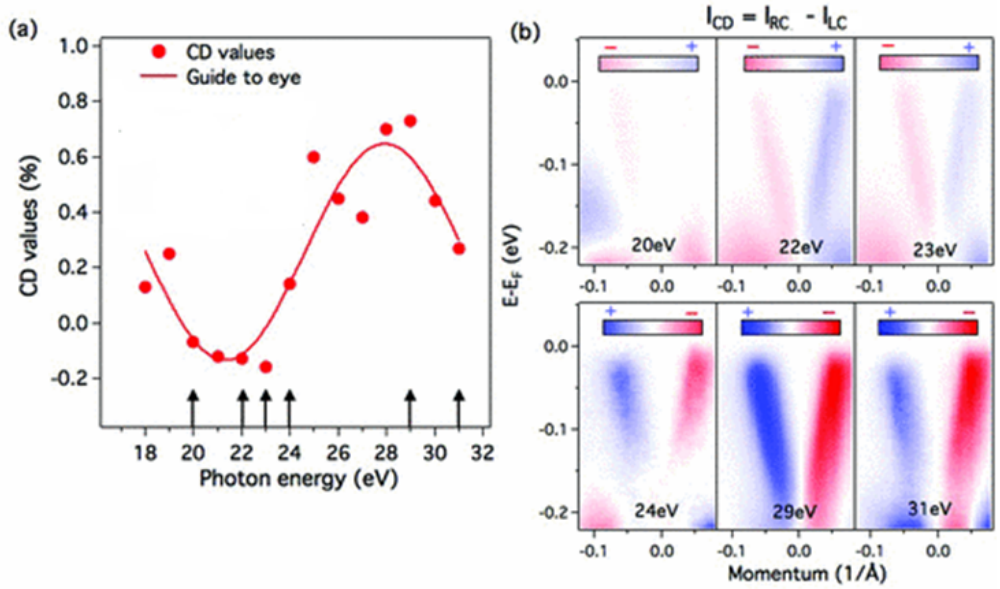

Fig. 1.9: (a) The measured dichroic asymmetry (CD values) is plotted as a function of photon energy. Arrows represent the photon energies of representative CD-ARPES spectra presented in (b). The corresponding photon energies are noted on the plots. From [50].

Another problem in the interpretation of CD-ARPES data arises if we look at the CD-ARPES measurements varying the photon energy. As shown in Fig. 1.9(a), the surface CD signal A exhibits an oscillating behavior as function of the photon energy [45, 46, 48, 50]. This particular dependence of the asymmetry as function of the photon energy is reported also for other materials indicating that it is a general characteristic of the CD-ARPES technique [51, 52]. This behavior could be ascribed to the so-called final state effect.The dichroic signal cannot be interpreted only in terms of initial-state. As decribed in Chapter 3, photoemission is a process that involves a transition between the initial electronically occupied state and the final, empty state. Thus, also final-states having a different orbital character or a spin-order could show a dichroic asymmetry. Then, final-state effects must be taken into account when we look at the CD-ARPES data. Depending on the photon energy, either a p-orbital, an s-orbital or a free-electron final state can be reached and this determines how much the dichroic pattern is affected [48]. In addition, final-state effects could give rise to anomalies in the detected CD signal but relativistic calculations have proven that also in this

non-ideal case the out-of-plane component of the spin could be derived by CD-ARPES measurements [53]. Moreover, relativistic one-step CD-ARPES calculations have shown that photons of energy h$\nu = 6$ eV allow to reach an *s*-type final state [48]. The spherical isotropic symmetry of the s final state cannot affect the initial-state spin-order. Then, we can confidently assume that low-photon energy CD-ARPES measurements could provide information about the spin-order in topological insulators.

1.4 Out-of-equilibrium dynamics in the unoccupied bands of topological insulators

At the end of Section 1.2 we have shown how topological insulators can provide a fllux of spin-polarized electrons by interaction with polarized light [6, 7]. This suggests the possibility of using topological insulators as base for future opto-spintronics devices. Moreover, the capability to optically trigger a surface spin-polarized current has been demonstrated [8], actualizing this future scenario. To better exploit the potentialities of this materials in opto-spintronics applications, an accurate characterization of their ultrafast response to optical perturbations is fundamental. Time-resolved and angle-resolved photoemission spectroscopy (TR-ARPES) is the best technique to achieve this characterization providing direct access to the out-of-equilibrium electronic dynamics in the band structure. A more detailed description of this technique, widely used in this thesis work, will be addressed in Chapter 3. In few words, contrary to traditional ARPES the sample is prepared in an excited state by an infrared-visible optical ultrashort pulse called *pump*. Then, like in ARPES, the electronic band structure is probed by a second delayed ultraviolet pulse, called *probe*. Changing the delay between the pump and the probe pulses is possible to map the evolution of the band structure in the time domain and then have acess to the electronic dynamics. To address the electronic transition driven by the light excitations a detailed knowledge of the unoccupied electronic states is required. This characterization can also be achieved exploiting out-of-equilibrium spectroscopies such as TR-ARPES or two-photon photoemission (2PPE). 2PPE slightly differs from TR-ARPES using two photons with energy $h\nu_{1,2}$ lower than the work-function Φ of the sample (tipically 4-5 eV) but satisfing the condiction $h\nu_1 + h\nu_2 > \Phi$. Single photon optically excites the system promoting electrons into unoccupied states. Consequently electrons are photoemitted from unocupied bands by two-photon processes overhelming the work function Φ. In this way, a snapshot of the empty band dispersion is provided. In the following, we will

report a short list of the pivotal studies on electronic dynamics in TIs in the perspective to better clarify our experimental results in Chapter 4.

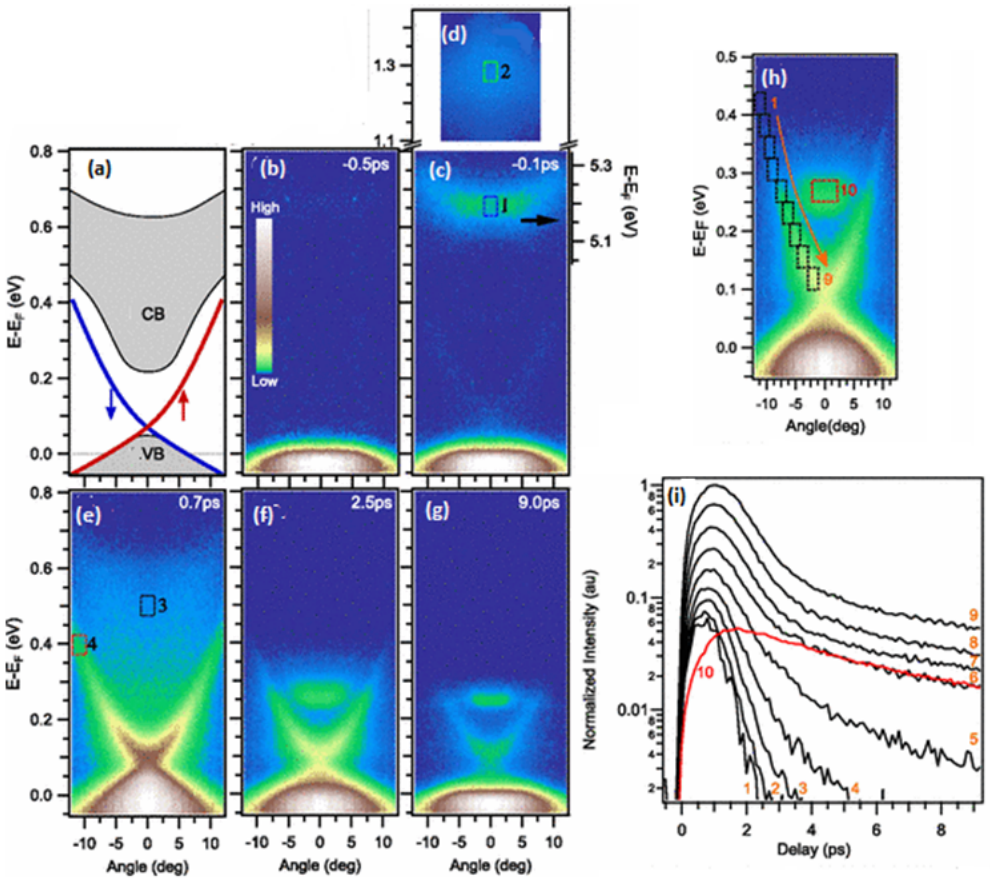

Fig. 1.10: (a) Schematic of the electronic band structure for Bi_2Se_3. Grey shaded regions represent the bulk valence (VB) and conduction (CB) bands. Lines represent the TSS with spin texture indicated. (b)(f) TR-ARPES spectra near the $\bar{\Gamma}$ point for various pump-probe delays. Note in the panel (c) the separate energy axis for the image potential state (IPS). (h) Transient photoemission intensities within the integration windows indicated in the TR-ARPES map at 2.5 ps (g). Red urve 10 corresponds to the integration window over the CB edge, and is normalized to match the intensity of the TSS intensities. From [54].

Figure 1.10 shows the first TR-ARPES measurements on the prototypical Bi_2Se_3 [54]. In order to follow the electronic dynamics of the Dirac cone,

TR-ARPES measurements have been performed on p-doped Bi_2Se_3 [54]. In this doping configuration, the Dirac cone is mostly unoccupied, allowing the study of Dirac fermion population dynamics after an optical excitation. In this experiment, the pump is the fondamental radiation of a Ti:sapphire laser (1.5 eV, 50 fs) and the occupied and unoccupied states are probed by UV laser pulse (6 eV, 160 fs). Figure 1.10(a) gives a sketch of the band structure of the system around the Fermi level E_F (0.0 in the figure) at the $\bar{\Gamma}$-point of the Brillouin zone. Figure 1.10(b) shows the unperturbed ARPES map: notice that only the top of the valence band is visible, as expected by the p-doped samples. The first features to be populated upon optical excitation are shown in Fig. 1.10(c). Curiously, the parabolic dispersing feature (labeled 1) appears to be populated before time zero. This feature is an image potential state (IPS) [55]. IPS is a bound electron state in front of the metallic surface of the sample pumped by the UV probe pulse and photoemitted by the infrared pump pulse. For this reason, it presents a reversed dynamics due to the exchanged roles of pump and probe. The feature labeled 2 results from a direct optical transition pumped from the edge of the bulk valence band (VB) to higher energy bulk bands. The bulk conduction band (CB) (labeled 3) and the TSS (labeled 4) have a negligible population around time zero and it takes 700 fs to reach maximum population (Fig. 1.10(d)). This indicates that the pump does not populate directly these bands. They are indirectly populated by the relaxation of higher-lying bulk bands electrons. After 2 ps (Fig. 1.10(e)) CB relax toward its bottom while TSS electrons accumultate around the Dirac point. The subsequent dynamics is slower and persists for more than 10 ps (Fig.(1.10(f)). The CB forms a metastable population due to the bulk energy gap that obstructs the decay channels. Surprisingly, also the TSS exhibits a persistent population. Photoconductivity of a metallic surface state is unexpected. The absence of a band gap means infact that no barriers to rapid recombination are present. This persistent TSS population is attributed to a continous filling from the metastable CB state that acts as a reservoir of electrons. This is evident when looking at Figs. 1.10(g),(h). Figure 1.10(h) shows the transient photoemission intensity obtained by integrating within the windows indicated in (g). Above the CB, the TSS decays with a single exponential. Below the CB a second slower component is observed, reflecting the presence of an additional channel. As seen in Section 1.2, the inelastic scattering between electrons and phonons has been found very weak indicating a non-efficient thermalization decay channel. This less-effective coupling has been confirmed also by several TR-ARPES experiments [56]. The reduced surface scattering contributes to the persistence of TSS population. In addition, at the Dirac point there is also a reduction of the density of states. This acts as bottleneck for the elec-

tronic recombination giving rise to the observed persistent population in the upper part of the Dirac cone.The same kind of investigation on several TIs reports similar results [57–62]. The TSS presents always a delayed response and a long life-time ranging from fews picoseconds to microseconds in bulk-insulating TIs. This properties are relevant for transport applications. For bulk crystals in equilibrium, current is typically dominated by non-polarized CB carriers. In this experiment, the transient populations are generated only in this near-surface region in which spin-polarized TSS contribution to transport is enhanced. In addition, bulk-insulating TIs have a large bulk resistivity and present an extremely long-lasting Dirac fermions population allowing to exploite the photon-driven transient spin currents without overwhelming contributions from the bulk.

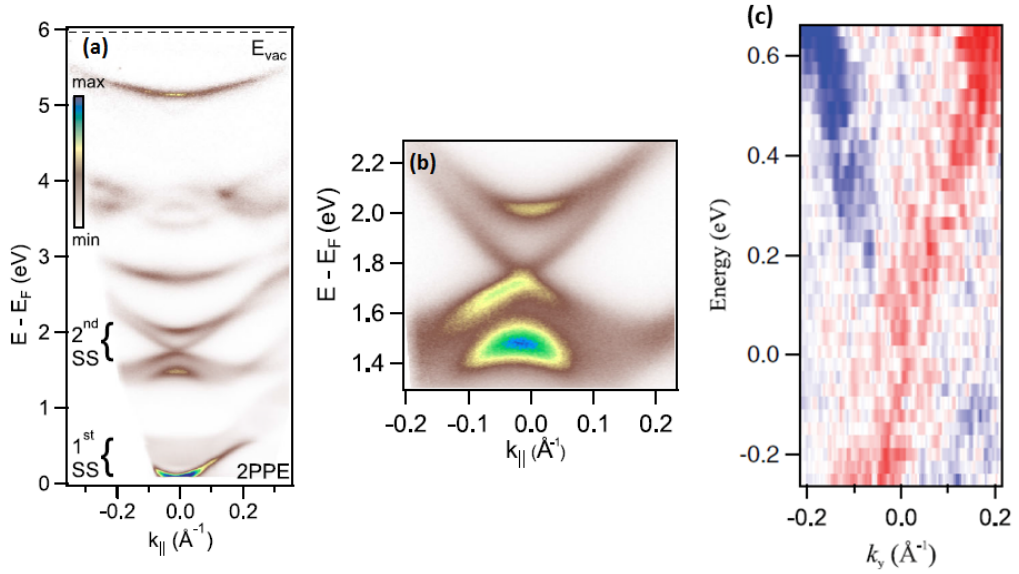

Fig. 1.11: (a) Two-photon photoemission (2PPE) (6 eV + 6 eV) on p-doped Bi_2Se_3. (b) A zoom around the empty Dirac cone. From [63]. Circular dichroism 2PPE data (4.65 eV + 6 eV) on the empty Dirac cone (ESS). The position of the Dirac point of the ESS is indicated by 0.0. From [64].

Two-photon photoemission (2PPE) measurements on Bi_2Se_3 have shown an extremely interesting and unexpected feature in the unoccupied states: a second Dirac cone located within an additional local bulk energy gap around 2 eV above the Fermi level. Figure 1.11(a) shows 2PPE results using 6-eV photons [63]. Other 2PPE experiments on bismuth chalcogenides are performed using third and fourth harmonic of the fondamental radiation of a

Ti:sapphire laser [64, 65]. All these techniques revealed a structure with a linear dispersion around the $\bar{\Gamma}$-point within a local bulk energy-gap in the unoccupied states (Fig. 1.11(b)). Theoretical investigations [64] have shown that the SOC is at the base of this structure, suggesting the shared nature with the TSS located at the Fermi level. Additional evidence of the topological character of this unoccupied surface state emerges from its spin texture derived from CD-2PPE measurements performed with a circularly polarized third harmonic (4.65 eV) [64]. As shown in Fig. 1.11(c), dichroic asymmetry clearly suggests a Dirac cone's spin-texture for this state confirming its topological nature. In Bi_2Se_3 the second Dirac point is found to be 1.8 eV above the first one suggesting a possible direct coupling of pump-photons with the second TSS. By the way, so far the dynamics of this state has not been addressed by any experiments. Our experimental results on the second Dirac cone in Bi_2Se_3 are presented in Chapter 4.

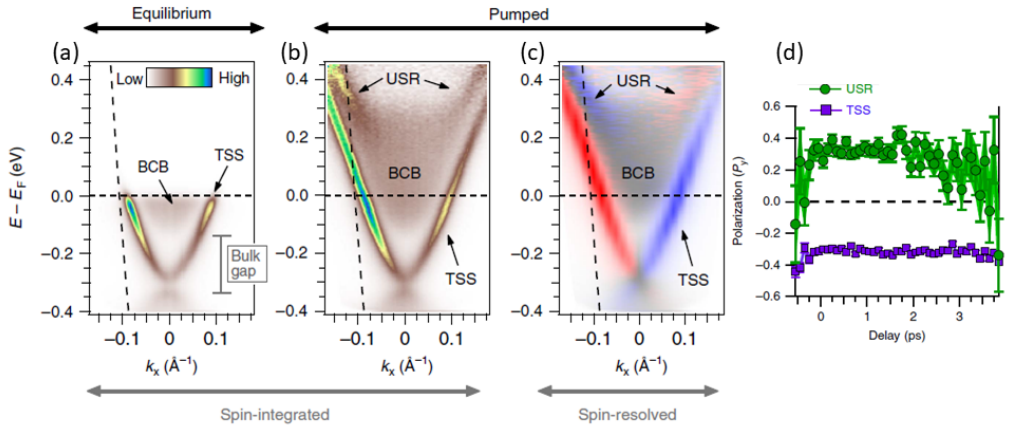

Fig. 1.12: (a) Equilibrium (no pump) spectrum taken along $\overline{\Gamma K}$ in spin-integrated mode. The colorscale represents photoemission intensity. (b) Same spectrum, but with pump, after 700 fs from the pump excitation. The continuation of the TSS above the bulk band gap is well resolved. An increase in spectral weight toward the top of the BCB coincides with the unoccupied surface resonance (USR). (c) Spin-resolved map of the pumped spectrum, showing that the USR is spin-polarized in a direction opposite to that of the TSS. (d) The delay-dependent spin polarization of the TSS and of the USR, constant within statistical error bars. From [66]

As discussed at the beginning of this Section, one of the most promising application of TIs is opto-spintronic devices. Several experiments have shown in fact that when a polarized light is shined on TIs surface, a net surface induced

photo-current appears[8, 67–72]. Since this current is related to the metallic surface state, it is spin-polarized. However, these optical experiments could access only averaged quantities in which the finite bulk response dominates making the TSS role hard to highlight. The origin of the photo-induced surface photo-curent is the photogavalnic effect, in which an out-of-equilibrium asymmetric population in **k**-space is originated by polarized-light [73, 74]. Recently, TR-ARPES measurements on Sb_2Te_3 TIs gave a direct microscopic view of the photogalvanic effect [75, 76]. Using mid-infrared pump pulses, electrons fron the lower part of the Dirac cone can be promoted into the upper part. They observed that for opposite polarizations of the pump pulses, an asymmetry in the out-of-equilibrium population appears at opposite momenta. In addition, momentum-scattering effects induced a flow along the Dirac cone indicating a current in **k**-space. However, the role of the spin in this mechanism is still undisclosed. We performed an analogous investigation inducing a population in the second TSS of Bi_2Se_3 using circularly-polarized pump pulses allowing us to highlight the role of the spin in the surface photocurrent. Our results are presented in Chapter 4.
As seen in Sec. 1.1, the TSS originates from an energetical band inversion driven by the strong spin-orbit coupling (SOC). Moreover, SOC is at the base of the complex layers spin and orbital texture. The presence of a second Dirac cone in the unoccupied states is another consequence of the SOC. In the following we will discuss recent TR-ARPES experiments that highlighted additional consequences of the band inversion and the SOC on the band structure of TIs. In particular, they disclosed the existence of spin-polarized surface-resonance state (SRS) within the bulk conduction bands [66, 77, 78]. Fig. 1.12(c) shows the first direct full momentum spin-polarization map of the SRS. Notice the presence of a net spin-polarization in the region occupied by the CB, that does not exhibit any polarization as expected. Moreover, the polarization of the SRS is always opposite to the one of the TSS for all momenta, suggesting an analogous spin-texture with opposite orientation. As already reported for the TSS (see Sec. 1.2) [6, 7], the spin of the electrons photoemitted from the SRS depends on the polarization of the probe. This suggests that the SRS shares with the TSS not only the spin-texture but also the non-trivial orbital texture and the extension among the QL. In addition, as shown in Fig. 1.12(d), the TSS and the SRS exhibit a spin-polarization constant in time within their temporal resolution. Similar temporal behaviour is proper of truly spin-polarized bands indicating no effects related to the pump pulse. Tight-binding calculations suggest that both the TSS and the SRS originate from pristine Rashba states modified by the non-trivial topology highlighting again the fundamental effect of the SOC on the band structure of TIs.

Chapter 2

Charge density waves in layered materials

Every breaking wave on the shore
Tells the next one there'll be one more
And every gambler knows that to lose
Is what you're really there for

Every breaking wave on the shore
from Songs of Innocence (2015), U2

Layered materials, i.e. presenting a high anisotropy in the crystal and also in the electronic structure, are nowadays a reality attracting attention for their peculiar properties such as non-conventional superconductivity and metal-to-insulator instability. In particular, the latter one can occur as consequence of a Charge Density Waves (CDWs) phase transition. The transition-metal dichalcogenide 1T-$TiSe_2$ is a layered bi-dimensional (2D) system in which a CDW phase occurs below the critical temperature T_{CDW}= 202 K. The CDW ground state is accompanied by a 2x2x2 lattice reconstruction in real space [14]. Although this phase transition is well known since the '70s, its driving mechanism is still an open-question and is largely debated in the scientific community.
In the following chapter we will provide a detailed introduction to CDWs phase transition. Starting from the simplest case of a metallic 1D atomic chain in a weak electron-lattice coupling regime, we will highlight some important aspects of the physics of the CDWs. Then the effect of instability and higher dimensionality will be taken into account. In conclusion, we will give an introduction to the physics of 1T-$TiSe_2$ investigated in this work, with particular attention to previous ARPES and TR-ARPES measurements.

2.1 Charge-density waves: an introduction

Due to their reduced phase-space, low dimensional systems exhibit a rich variety of phenomena [1]. In particular, one of the most peculiar is the instability of the metallic phase that leads to a translation-symmetry broken ground state called charge density waves (CDWs) phase [79–82]. To better understand what a CDW is, we consider the simplest case of a one-dimensional (1D) metal made of a monoatomic linear chain with spacing a. Now imagine to modulate the electronic density with the cosinusoidal function:

$$\rho(\mathbf{r}) = \rho_0(\mathbf{r})[1 + \rho_1 cos(\mathbf{q_0}\mathbf{r} + \phi)], \tag{2.1}$$

with $\rho_0(\mathbf{r})$ describing the pristine electronic density, ρ_1 , $\mathbf{q}_0$ and ϕ are the amplitude, the wavevector and the phase of the electronic density modulation, respectively. We call charge-density wave the last term in the bracket of equation 2.1. The last term in eq. 2.1 represents a standing wave with wavelength $\lambda_0 = \frac{2\pi}{|\mathbf{q}_0|}$ [14, 79]. The new modulated electronic density leads to a novel modulated Coulomb potential. As a consequence, ions in the chain move to different equilibrium positions resembling the relative maxima of the modulated potential. This leads to a Periodic Lattice Distortion (PLD) with the form:

$$u_n = u_0 sin(n|\mathbf{q}_0|a + \phi)], \tag{2.2}$$

with n being position-index of the ions in the chain. In eq. 2.2 the amplitude u_0 is generally smaller than the lattice constant a describing a small perturbation of the lattice. The same results is obtained reversing the previous scenario. If we now consider first a lattice distortion as described by eq. 2.2, the conduction electrons will move in order to screen the new ionic potential. This leads to an electronic density modulated according to eq. 2.1. Thus, a PLD leads to the formation of CDWs and *viceversa*. A CDW always occurs togetehr with a PLD and we can use both terms to refer to this phase of matter [83, 84].

The simple model that we have here presented leads to some questions: is the PLD the driving force of the transition or is the CDW/PLD phase primarily an instability of the charge systems? Modifying the lattice and the electronic density implies a cost in terms of elastic and Coulomb energy: what is the microscopic mechanism that stabilizes this phase? Although CDWs in low-dimensional materials is a well-known and widely investigated topic, we are far from a complete and realistic microscopic coherent theory describing it. However, several qualitative models have been proposed giving the description of important aspects of the CDW phase. In particular, a mean-field theory for weakly-coupled (i.e. $u_0 \ll a$) one-dimensional systems is able to

provide a good explanation for the occurence of a CDWs phase in 1D- and also in some 2D-materials [79, 85, 86]. In the following, we will introduce this ideal simple model to present the physics underlying the CDWs/PLD phase-transition. Then, the effect of fluctuations, dimensionality and strong coupling will be taken into account. In conclusion, different proposed proposed at the origin of CDWs/PLD in 2D transition-metal dichalcogenide family will be introduced.

2.1.1 Peierls instability

The CDW/PLD defined by eq. 2.1 and eq. 2.2 in the previous section is well described by a Peierls mode [79–81]. Peierls instability essentially represents a structural phase transition of the coupled electron-lattice system from a metallic to an insulating ground state driven by strong electron-phonon coupling. In the Peierls model, the strong electron-phonon coupling leads the 1D-system to be unstable towards the formation of a CDWs/PLD. This model also addresses the question about the energetic stabilization of the new ground-state. As seen, the formation of an electronic modulation and lattice distortion implies a cost to pay in terms of Coulomb and elastic energy. In the Peierls model, CDW and PLD lead to the opening of a band energy gap at the Fermi level. Then, the energy of occupied electronic states decreases while the unoccupied bands are pushed up in energy. The resulting energy gain of the electron system counteracts the cost of the CDW/PLD occurency in a self-sustaining mechanism. Thus, due to the opening of an energy gap, a quasi 1D- metal undergoes a transition to an insulating phase.
We can describe quantitatively Peierls instability in the framework of a mean-field theory for a 1D electron-lattice system in the limit of weak coupling using independent electron, harmonic and adiabatic approximations [14, 79, 80]. The system is then described by Fröhlich Hamiltonian [81]:

$$H = \sum_{\mathbf{k}} \epsilon_{\mathbf{k}} a^{\dagger}_{\mathbf{k}} a_{\mathbf{k}} + \sum_{\mathbf{q}} \hbar\omega_{\mathbf{q}} b^{\dagger}_{\mathbf{q}} b_{\mathbf{q}} + \frac{1}{\sqrt{N}} \sum_{\mathbf{k},\mathbf{q}} g_{\mathbf{q}} a^{\dagger}_{\mathbf{k}+\mathbf{q}} a_{\mathbf{k}} (b^{\dagger}_{-\mathbf{q}} + b_{\mathbf{q}}), \tag{2.3}$$

with $\epsilon_{\mathbf{k}}$ being the energy of the electron state $\mathbf{k}$, $a^{\dagger}_{\mathbf{k}}$ and $a_{\mathbf{k}}$ creation and annihilation operators for state $\mathbf{k}$, $\omega_{\mathbf{q}}$ is the frequency of the phonon $\mathbf{q}$, $b^{\dagger}_{\mathbf{q}}$ and $b_{\mathbf{q}}$ creation and annihilation operators for phonon normal mode $\mathbf{q}$, $g_{\mathbf{q}}$ is the electron-phonon coupling constant and N is the number of lattice sites per unit length. Thus, in Fröhlich Hamiltonian, the first term represents the electron gas energy, the second is the lattice energy in the harmonic approximation. The last term describes the electron-phonon interaction, i.e.

the transfer of one electron from a state $\mathbf{k}$ to a state $\mathbf{k}+\mathbf{q}$ mediated by the phonon mode $\mathbf{q}$.
In terms of this Hamiltonian, the displacement $u_{\mathbf{q}}$ of phonon mode $\mathbf{q}$ creates the potential

$$v_{\mathbf{q}} = g_{\mathbf{q}} u_{\mathbf{q}} \sqrt{\frac{2M\omega_{\mathbf{q}}}{\hbar}}, \tag{2.4}$$

where M indicates the ionic mass. The cost in terms of elastic energy associated to the displacement $u_{\mathbf{q}}$ is then

$$\delta E_{lattice} = \frac{1}{2} M \omega_{\mathbf{q}}^2 u_{\mathbf{q}}^2. \tag{2.5}$$

In an electron gas, an external time indipendent perturbation as $v_{\mathbf{q}}$ in eq.2.4 induces a rearrangement of the charge density. The total induced energy change is described within the linear potential theory as

$$\delta E_{band} = -|v_{\mathbf{q}}|^2 \chi(\mathbf{q}), \tag{2.6}$$

where $\chi(\mathbf{q})$ is the so-called Lindhard response function for a non-interacting electron system and it is defined, for d dimension, as

$$\chi(\mathbf{q}) = \int \frac{d\mathbf{k}}{(2\pi)^d} \frac{f_{\mathbf{k}+\mathbf{q}} - f_{\mathbf{k}}}{\epsilon_{\mathbf{k}} - \epsilon_{\mathbf{k}+\mathbf{q}}}. \tag{2.7}$$

Here $f_{\mathbf{k}}$ is the Fermi-Dirac electronic distribution $f(\epsilon_{\mathbf{k}})$. As shown in eq. 2.6, Lindhart function is directly related to the distortion-induced energy gain [79]. In the following Section, we will evaluate Lindhart function for an electronic gas showing how, in low-dimensional systems, this leads to an instability towards the formation of a CDW.

2.1.2 Fermi surface nesting

To evaluate Lindhard integral, we consider the case of a one-dimensional free electron gas. The electron energy is purely kinetic and in $\mathbf{k}$-space has the form $\epsilon(k) = \frac{\hbar^2 k^2}{2m}$, where m is the electron mass. The Fermi energy is then given by $\epsilon_F(k) = \frac{\hbar^2 k_F^2}{2m}$ where the Fermi wavevector is proportional to the length L of the 1D-chain by the relation $k_F = \frac{N_0 \pi}{2L}$, with N_0 being the total number of electrons.

Regarding eq. 2.7, a large linear response is obtained in the case of a large numerator $f_{\mathbf{k}+\mathbf{q}} - f_{\mathbf{k}}$ and a small denominator $\epsilon_{\mathbf{k}} - \epsilon_{\mathbf{k}+\mathbf{q}}$ over a high number

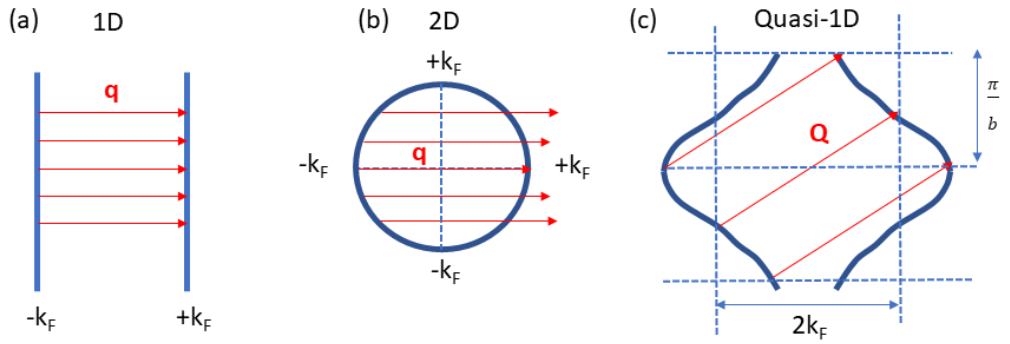

Fig. 2.1: Fermi surface nesting condition in (a) 1D, (b) 2D and (c) quasi-1D systems.

of **q**-coupled states. Thus, the most significant contributions to the integral in eq. 2.7 arise around the Fermi surface, i.e. the dispersion of the band structure over the **k**-space at the Fermi energy. Only around the Fermi surface an electron could be scattered from an occupied state to an unoccupied one by a low-energy excitation giving rise to the largest contribution in the evaluation of the Lindhart function (eq. 2.7) [79]. This condition is satisfied by 1D-dimensional systems because of the particular topology of the Fermi surface. As shown in Fig. 2.1(a), the Fermi surface of a one-dimensional metal consists of two points in the 1D reciprocal space sheets at $\pm k_f$. In this case, a low-energy excitation coupling electrons and holes has possible transitions only for $\mathbf{q} = 2\mathbf{k}_F$. The possibility to superimpose exactly one portion of the Fermi surface onto another section by a single wavevector **q** is the concept of Fermi surface nesting, that plays, as seen, an important role to evaluate the electronic response of the system.
For a one-dimensional electron gas, it is possible, for $\mathbf{q} = 2\mathbf{k}_F$ [79], to approximate linearly the dispersion around the Fermi energy as $\epsilon_k - \epsilon_F = \hbar v_F(k - k_F)$ where $v_F = \frac{\hbar k_F}{m}$ is the Fermi velocity. With this approximation we obtain

$$\chi(q) = -e^2 n(\epsilon_F) ln \mid \frac{q + 2k_F}{q - 2k_F} \mid, \tag{2.8}$$

where $n(\epsilon_F)$ represents the density of states for one spin component at the Fermi level.

Figure 2.2 shows the Lindhart function evaluated over all q-values. For completeness, the behavior for higher dimensions is also reported. The condition for Fermi surface nesting in 1D-systems leads to a divergence of eq. 2.8 for $\mathbf{q} = 2k_F$. This implie that an external perturbation, as seen in eq. 2.6, leads

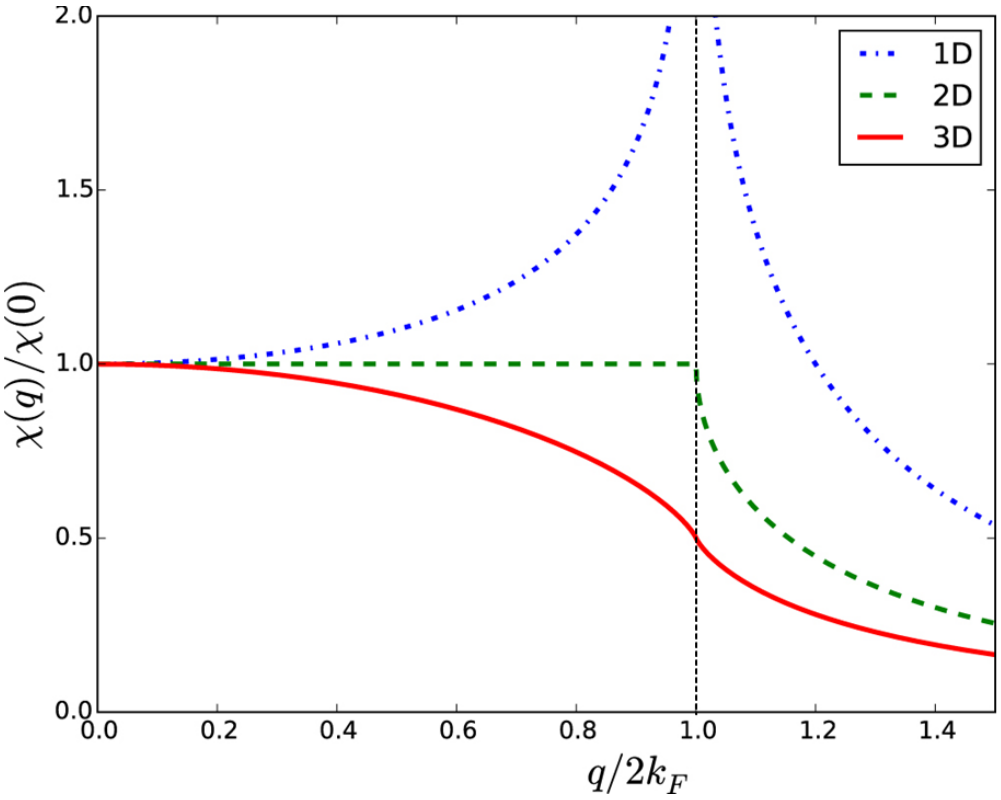

Fig. 2.2: Wavevector **q**-dependent Lindhart function for 1D, 2D and 3D systems. From [87].

to a divergent energy change. The electron gas is indeed unstable towards a periodically modulated charge distribution with a period related to k_F:

$$\lambda = \frac{2\pi}{\mathbf{q}} = \frac{\pi}{|\mathbf{k}_f|}. \tag{2.9}$$

Where the number of electrons per site is not a simple fractional number, the periodic CDW/PLD superstructure in general has a period λ_0 incommensurate with respect to the underlying lattice parameter [14].
As shown in Fig. 2.1(b), for higher dimensions the degeneracy at $2k_F$ is removed. This is due to less efficient Fermi nesting condition due to the different topology (see Fig. 2.1(b)). The role of the electronic linear response and of the Fermi surface in the formation of CDW/PLD phase in 2D-materials is largely diminished [14, 79] leading to the open question about the origin of this phase transition in these materials.
The 1D Fermi surface represented in Fig. 2.1(a) is an ideal case. A more realistic case should take in consideration also the Coulomb interactions between

adjacent chains [88–90]. This leads, for materials with a large anisotropy along the chains direction, to the quasi 1D-Fermi surface in Fig. 2.1(c). In this case, as for the 1D-ideal one, we find a topology with a large possible Fermi nesting. The wavevector of the nesting is now $\mathbf{Q} = (2k_F, \frac{\pi}{b})$ where b is the lattice constant in the direction orthogonal to the chains. Lindhart function presents now a singularity for $\mathbf{q} = \mathbf{Q}$. The CDW/PLD modulation along the chain has wavevector $q_{||} = 2k_F$ as in the ideal case. In the orthogonal direction we have an out-of-phase periodic modulation between first neighbour chains with wavevector $q_\perp = \frac{\pi}{b}$.

2.1.3 Kohn anomaly

As seen so far, the coupled electron-phonon system is unstable towards the formation of CDW/PLD. Thus, we expected that this instability has fundamental consequences on both the electron and phonon spectrum [83]. To clarify how the electronic band structure and phonon dispersion is modified, we consider the archetypal half-filled single band 1D-metal. The band dispersion, according to a tigh-binding modelization, is $\epsilon_k = -E_F cos(ka)$ with E_F Fermi energy [91, 92]. The Fermi vector is $|\mathbf{k}_F| = \frac{\pi}{2a}$. For this band it is possible to derive the temperature-dependent Lindhard linear response function in the limit $\frac{E_F}{k_B T} \gg 1$, with k_B Boltzmann's constant. In this limit, eq. 2.7 becomes

$$\chi(2\mathbf{k}_F, T) = \frac{1}{2} N(E_F) ln(\frac{2.28 E_F}{K_B T}), \tag{2.10}$$

where $N(E_F)$ is the electron density for both spin directions at the Fermi level in the normal phase [79]. Considering the equation of motion for small amplitude displacements in a system described by Fröhlich Hamiltonian (eq. 2.3),in the mean-field approximation it is possible to derive an expression for the renormalized phonon frequency due to the CDW periodic modulation:

$$\tilde{\omega}_q^2 = \omega_q^2 + \frac{2g^2\omega_q}{\hbar} \chi(q, T). \tag{2.11}$$

Here, we indicate as $\tilde{\omega}_q$ and as ω_q the renormalized and normal-phase phonon frequency, respectively [83].
As seen in the previous section, the divergence of the Lindhard function occurs at $q = 2k_F$. Then, the maximum reduction, or softening, of the renormalized phonon spectrum will occur at this wavevector. Combing eq. 2.11 with the temperature-dependent eq. 2.10 for wavevector $q = 2k_F$ we

obtain

$$\tilde{\omega}^2_{2k_F} = \omega^2_{2k_F}\left(1 - \frac{4g^2N(E_F)}{\hbar\omega_{2k_F}} ln(\frac{2.28E_F}{K_BT})\right). \tag{2.12}$$

Expanding eq. 2.12 around the transition temperature, we can easily obtain [79]

$$\tilde{\omega}_{2k_F} = \omega_{2k_F}\sqrt{\left(\frac{T - T^{MF}_{CDW}}{T^{MF}_{CDW}}\right)}. \tag{2.13}$$

Decreasing the temperature, the Lindhard function peaks more and more around $q = 2k_F$ as described by eq. 2.10. This drives the renormalized phonon frequency to zero $\tilde{\omega}^2_{2k_F} = 0$. This complete softening of the phonon mode is usually called Kohn anomaly. It represents a state with a frozen-in distortion with periodicity given by eq. 2.9 [14, 79]. Combining eq. 2.12 with Kohn anomaly condition, we obtained an instability criterion for the CDW/PLD formation:

$$\frac{4g^2_q}{\hbar\omega_q} > \frac{1}{\chi(q)}. \tag{2.14}$$

For the occurrency of the CDW/PLD phase, a strong electron-phonon coupling is required together with a large electronic linear response at the wavevector q.
Kohn anomaly defines the transition temperature T^{MF}_{CDW}. From eq. 2.12,

$$k_BT^{MF}_{CDW} = 2.28E_F exp(-\frac{1}{\zeta}), \tag{2.15}$$

with $\zeta = \frac{2g^2N(E_F)}{\hbar\omega_q}$ being the dimensionless electron-phonon coupling [79].

2.1.4 Energy band gap

The formation of the CDW/PLD phase leads the phonon spectrum to a strong renormalization and in particular, as seen, Kohn anomaly occurs. This, together with the lattice displacement, strongly affects also the electronic band structure. In the framework of the tight-binding model for half-filled 1D-metal developed in the previous section, the CDW is perfectly commensurate with $\lambda = 2a$. The ions move in real space doubling the chain-spacing, as shown in Fig. 2.3(a). This implies that, in the reciprocal space, vectors $k = \pm\frac{\pi}{2a}$ are in the new ground-state novel Brillouin zone edges, i.e. Bragg planes [14, 79, 93]. This implies the opening of a band gap as shown in Fig. 2.3(b). The normal state band ϵ_k (dashed black parabolic line) splits in a totally occupied branch and in an upper branch completely empty (red

lines band structure). A uniform and complete energy band gap 2Δ opens at $\frac{q}{2} = k_F$, i.e. at E_F. The total density of states N(E) is zero between the gap and diverges for energies $E = \pm\Delta$ (see Figure 2.3(c)). This implies a metal-to-insulator transition occuring together with the CDW/PLD phase transition.

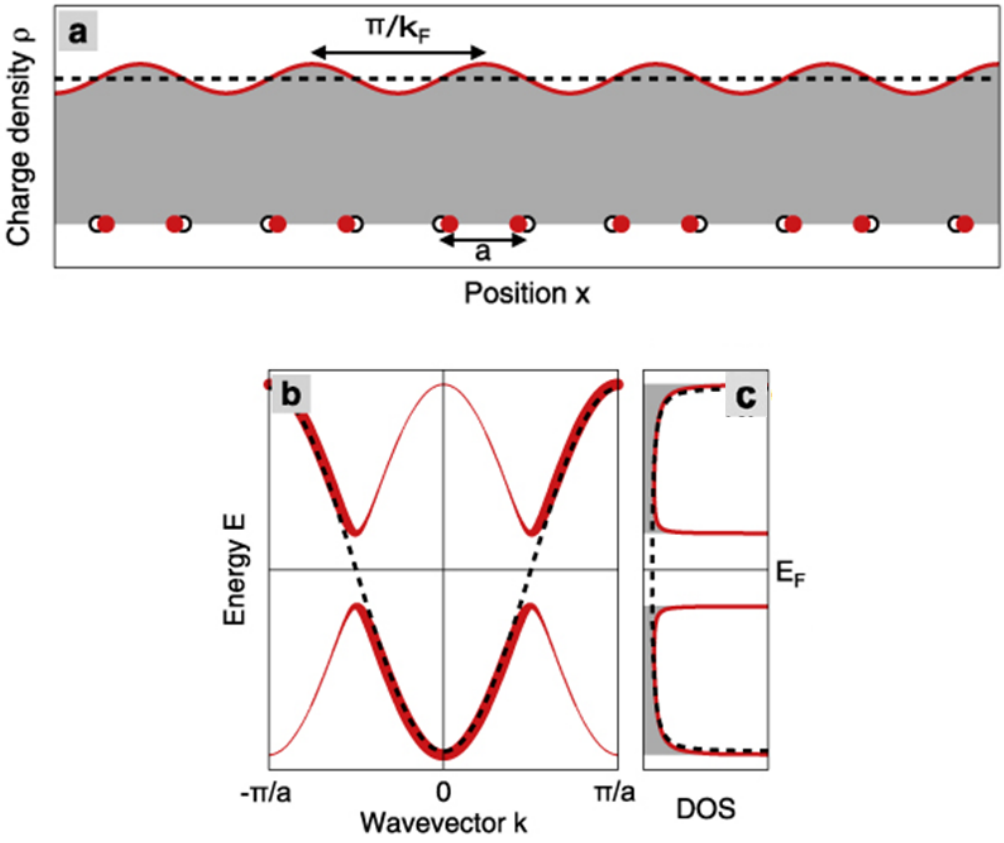

Fig. 2.3: Pictorial representation of Peierls instability of a half-filled band 1D metal. (a) Schematic view of a CDW/PLD showing the modulations of the electron density (solid red line) and ion positions (filled red circles). The normal state is characterized by a constant charge-density (dashed black line) and an undistorted chain (open black circles). (b) Electronic band dispersion and (c) density of states above (dashed black lines) and below (solid red lines) the transition temperature T_{CDW}. The thickness of the red lines in the band structure plot is proportional to the spectral weight carried by reconstructed bands in the CDW phase. From [14].

In the model here developed, the energy gap is given by [79]

$$\Delta = u_q g_q \sqrt{\frac{2M\omega_q}{\hbar}}. \tag{2.16}$$

In particular, the difference in energy between the two phases is

$$\Delta E = E_{normal} - E_{CDW} = \frac{n(E_F)}{2}\Delta^2, \tag{2.17}$$

and the positive sign implies that the energy of the CDW/PLD ground state in 1D is lower than the normal state [79]. It is possible to show that, for zero-temperature and in the tight-binding model, using eq. 2.15, the zero-temperature energy band gap could be written as

$$2\Delta(T=0) = 3.52 k_B T_{CDW}^{MF}, \tag{2.18}$$

that is the same equation that describe the superconducting band gap in the Bardeen-Cooper-Schrieffer (BCS) theory [94]. This implies that formulas derived in the BCS theory could be applied in the CDWs mean-field theory to evaluate the temperature-dependency of several quantities in the CDWs ground-state. In particular, it is possible to write the evolution of the band gap with the temperature as

$$\frac{|\Delta(T)|}{|\Delta(T=0)|} = 1.71\sqrt{\left(1 - \frac{T}{T_{CDW}^{MF}}\right)}. \tag{2.19}$$

Equation 2.19 is a redefinition of eq. 2.15; the T_{CDW}^{MF} is now defined as the temperature in which the energy gap closes, i.e. $|\Delta(T = T_{CDW}^{MF})|$ goes to zero.

The most direct experimental technique to measure the reconstructed band structure is angle-resolved photoemission spectroscopy (ARPES), discussed in details in Chapter 3. However, if we want to measure the modified band dispersion in a CDW ground-state, a difficulty arises since ARPES measured intensity is proportional to the electronic **k**-dependent spectral weight [14]. This spectral weight distribution is given by the one-electron spectral function $A(\mathbf{k}, E)$ that can be calculated in Green's function formalism for many-body systems. For the CDW ground state described so far, the spectral function is [14]

$$A(\mathbf{k}, E) = \frac{\delta(E - E_1(\mathbf{k})}{1 + \frac{\Delta^2}{E_1(\mathbf{k} - \epsilon_{\mathbf{k}+\mathbf{q}_0})^2}} + \frac{\delta(E - E_2(\mathbf{k})}{1 + \frac{\Delta^2}{E_2(\mathbf{k} - \epsilon_{\mathbf{k}+\mathbf{q}_0})^2}}, \tag{2.20}$$

where $\delta(E)$ is Dirac delta distribution and E_1, E_2 are the two branches separated by the open gap 2Δ. The spectral weight of the reconstructed bands is reported in Fig. 2.3(b). The thicker is the line, the larger is the spectral weight carried by the band. The spectral weight results mostly in the pristine bands and only around $\mathbf{k}_F$, where the band gap is open, a small weight is seen. Thus, the spectral weight conserves almost the undistorted periodicity, in contrast to the one of the novel CDW/PLD phase.

2.1.5 Effect of fluctuations

In the model we have introduce so far, we have completely neglected any effects of the fluctuations assuming, in the mean-field approach, the lattice as a rigid frame. In reality, the lattice is randomly in motion by thermal and quantum (i.e. zero-point) agitation. It is known that these fluctuations strongly affect low dimensional systems due to the reduced phase-space [79, 88–90]. The states around the Fermi level are particularly affected by these lattice motions leading to a smaller value of the energy band gap. The order parameter, i.e. the gap, can take any value between 0 and Δ reducing actually the electronic gain in the CDW phase [14, 79, 90]. Thus, the transition temperature is smaller than T_{CDW}^{MF}; in particular, for 1D and 2D systems a transition cannot occur anymore at non-zero temperature [95]. This implies also that a long-range order is forbidden for non-zero temperature, apparently in contrast with the occurence of CDWs.
While the CDWs phase is strongly suppressed by fluctuactions in an ideal 1D-materials, the Coulomb inter-chains interaction of quasi 1D-systems leads to the occurence of a non-zero temperature of the CDW/PLD with almost the same properties described in the previous sections [79]. A CDW/PLD is formed in any chain. In an ideal 1D-system, in each adjacent chain the CDW fluctuates randomly and indipendently from each other. By contrast, in a quasi 1D-material, the Coulomb interaction tends to align the CDWs of two neighbouring chains suppressing the fluctuation effects. To minimize the interaction energy, the two CDWs align each other with a π-phase difference forming a bidimensional superstructure as seen in Sec. 2.1.2 [79]. The transition temperature T_{CDW} in this situation is finite but smaller than T_{CDW}^{MF}. In particular, due to fluctuations there is not abrubt metal-to-insulator transition, i.e. opening of a gap. Below T_{CDW} a total band-gap is still opened, but, in the region of temperature between T_{CDW} and T_{CDW}^{MF} we observe a pseudogap with a slow decrease of the density of states around the chemical potential [90]. This is due to the remaining of short-range order distortions that smear the energy gap.

2.1.6 Pseudo Jahn-Teller mechanism

In 2D-systems the role of the Fermi surface and of the Lindhard response function is largely diminished with respect to the one-dimensional model described in the previous sections. As seen in Sec. 2.1.2, the favorable portion for Fermi surface nesting in 2D-materials is extremely small. This leads to a smooth Lindhard function; $\chi(\mathbf{q})$ does not present anymore a divergence at any particolar $\mathbf{q}$-vector [96, 97]. Applying the simple criterion for the formation of CDW/PLD phase expressed by eq. 2.14, we can see that the occurence of CDWs modulation in 2D-layered materials, as for example 1T-$TiSe_2$ studied in this thesis, requires an increased strength of the electron-phonon coupling [14]. The stronger electron-phonon coupling CDWs are characterized by a greater lattice distortion, a larger energy band gap and a shorter-order range [14].
As seen, Peierls instability can well describe only systems with a long-coherence length. In the short-range order scenario, a model involving local-chemical bonding is more accurate [98–100]. Atoms are now more propense to form clusters or pairs with short ligand-bond. This is due to the anarmonicity terms in electron-phonon coupling that cannot be neglected due to the greater atomic displacement. The total energy gain is due to the Jahn-Teller effect in molecules. The CDW/PLD then tend to freez the underlying crystal structure [96, 101, 102].
A mechanism analogous to molecular Jahn-Teller effect has been proposed as the driving mechanism of the CDW formation in 2D-materials and in particular in layered transition-metal dichalcogenides (e.g. 1T-$TiSe_2$) [96, 101, 102]. At the base of this mechanism there are simple energetic considerations between electrons and lattice energy that drives all crystal distortions. In particular, the energy gain has been noticed depend only on crystal structure considerations. The geometry of the crystal structure strongly affects the ligand-configuration of d-band in transion-metals. The lattice distortions lift away the degeneracy of the conduction d-bands lowering the energy of the d_{z^2}-bands. If this bands are partially occupied, the PLD leads to an energetic gain and the CDWs ground state occurs. Since this mechanism resembles the molecular Jahn-Teller effect but for unoccupied, or partially occupied, states, we refer to it as pseudo band Jahn-Teller effect. In the framework of this mechanism, a microscopic theory taking into account the effects of Fermi nesting and mode-dependent electron phonon coupling has been developed [96, 103]. In this theory, the softening of the frozen-in CDW mode originates from the temperature-dependent effective ion-ion interaction, remarking the driving role of the strong electron-lattice interaction.
Unfortunately, this mechanism that naturally originates from the strong

electron-lattice interaction fails to predict important quantities of the CDW ground-states like the order-parameter, i.e. the energy band gap [14]. For this reasons, a different model (purely electronic) for the description of CDW phase in 1T-$TiSe_2$ has been developed: the excitonic insulator instability model.

2.1.7 Excitonic insulator instability

In this section we present an antagonist CDW/PLD model. While in Peierls instability the formation of CDW/PLD is due to the strong electron-lattice interaction, here the instability is first driven by electron-hole Coulomb attraction, i.e. the formation of excitonic quasi-particle [104, 105]. The role of the lattice as driving force is negligible; the PLD occurs just as secondary accidental consequence due to a finite electron-phonon coupling. In any case, we want to point out that despite the different driving mechanism, the two models describe the same physics: a translational-broken symmetry ground-state, with charge and lattice modulations and the opening of an energy gap [106].

We consider a valence band with maximum at $\mathbf{k} = 0$ and a conduction band with energy-minimum at $\mathbf{k} = \mathbf{q}_0$ as shown by dashed black lines in Fig. 2.4. These two-bands are separated by a small energy gap Δ and their energy could be written as

$$\epsilon_k^{VB} = -\frac{1}{2}\Delta - \frac{\hbar^2}{2m_{VB}}\mathbf{k}^2, \qquad \epsilon_k^{CB} = \frac{1}{2}\Delta + \frac{\hbar^2}{2m_{CB}}(\mathbf{k} - \mathbf{q}_0)^2, \tag{2.21}$$

where m_{VB} and m_{CB} are the effective masses of the valence and conduction band, respectively. In this insulating phase the energy band gap is larger than the lowest-lying excitons binding energy E_B, i.e. $\Delta > E_B > 0$. Suppose now that the energy gap Δ reduces under the variation of some external parameter (e.g. the temperature). Since E_B stays finite, at some point we reach a situation in which $\Delta - E_B$ goes to zero. At this point, excitons can form a zero-cost. The spontaneous occurency of bounded excitons then leads to an electronic instability. The system undergoes an insulator-to-(semi)metal transition. We consider now the other direction of this transition. We have a semimetal with a finite small but negative Δ. In this configuration, under the variation of an external parameter (e.g. the temperature), the Δ becomes smaller and smaller leading to an instability of the electronic system. We can understand this transition in terms of Coulomb screening. In the semimetallic phase, the number of electrons and holes is enough to screen the Coulomb

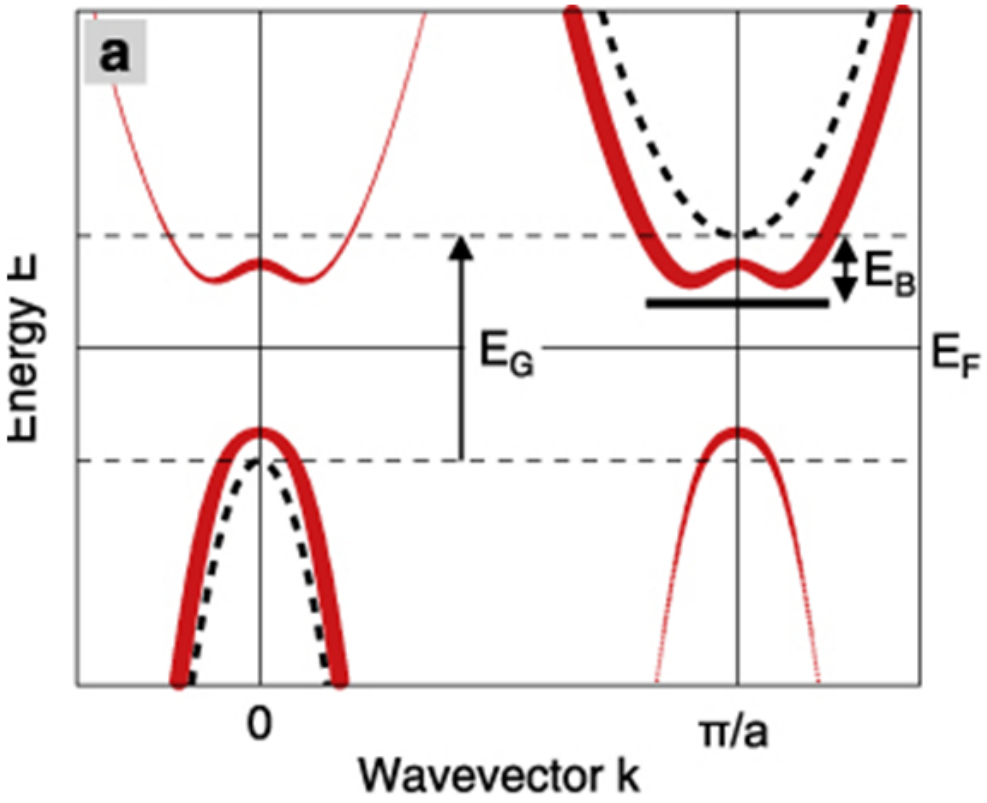

Fig. 2.4: Electronic band dispersion above (dashed black lines) the critical temperature and in the excitonic insulator phase (solid red lines). The thickness of the red lines is proportional to the spectral weight carried by the electron states in the excitonic insulator phase. From [14].

interaction between them. If the partial band overlap reduces, the number of electrons and holes decreases. At some critical point, their number is not anymore sufficient to screen the Coulomb attraction and bound states arise. This implies the opening of a gap driving the semimetal to an insulating phase. In the excitonic insulator phase, as shown by solid red lines in Fig. 2.4, the conduction band is deformed in the so-called *mexican hat* shape. The re-shaping of the electronic band structure can be modeled by the following effective hamiltonian:

$$H_{Exc.Ins.} = \sum_{\mathbf{k}} \epsilon_{\mathbf{k}}^{VB} a_{\mathbf{k}}^{\dagger} a_{\mathbf{k}} + \sum_{\mathbf{k}} \epsilon_{\mathbf{k}}^{CB} b_{\mathbf{k}}^{\dagger} b_{\mathbf{k}} + \sum_{\mathbf{k}} \Delta_{\mathbf{k}} (b_{\mathbf{k}}^{\dagger} a_{\mathbf{k}} + a_{\mathbf{k}}^{\dagger} b_{\mathbf{q}_0}). \tag{2.22}$$

The last term connects valence and conduction bands separated by a wavevector $\mathbf{q}_0$. We can adapt eq. 2.20 to the modified band-structure described by

eq. 2.22 to evaluate the **k**-dependent ARPES spectral weight for the excitonic insulator. The result is reported in Fig. 2.4. The spectral weight is represented by the thickness of the line drawing the bands. We have a folding of the valence and conduction bands in the reciprocal **k**-points with a small transfer of spectral weight from the original to the reconstructed bands. The repulsion between the band edges leads to the mexican hat shape.

If in the Peierls model the softening of the phonon corresponding to the CDW frozen-in modulation signals the novel ground-state, here the bosonic modes that feel that soften are the excitons and the plasmons. Besides this softening, a CDW/PLD occurs with a wavelength given by $\lambda = \frac{2\pi}{|\mathbf{q}_0|}$ (identical to eq. 2.9). The finite electron-phonon coupling mixes the softened electronic modes (with total spin $S = 0$) with some phonon modes ($S = 0$). Then, a PLD accidentally occurs with the same periodicity. This is the greatest difference with respect to Peierls mechanism. Here the CDW is purely due to the electron-electron interaction, i.e. the electron-hole attraction, and the lattice has only an accidental role. In the Peierls model, as seen, both systems are strictly entangled in the occurence of the new ground-state.

2.2 Charge-density waves in 1T-$TiSe_2$

Due to the layering, they can be described as bi-dimensional (2D) in terms of their electronic properties. Very often in this class of materials the ground state is characterized by the formation of a CDW and a PLD.

Into this family of materials, 1T-$TiSe_2$ is largerly interesting, being the only compound with a group IV B transition metal showing a CDW instability and the associated structural deformation below a critical temperature $T_{CDW} = 202K$ [108]. In addition, recent observation of superconductivity occuring in Cu-intercalated [109] or under-pressure [110] 1T-$TiSe_2$ offers a way to investigate the interplay between these two strongly-competing phases of matter [111]. Despite the wide theoretical and experimental investigation in the past decades, the driving force at the base of the CDW instability in 1T-$TiSe_2$ is still controversial. Several mechanisms have been proposed, from the 1970's pseudo Jahn-teller scenario (see sec. 2.1.6) to the excitonic condensate and a Jahn-Teller - excitonic hybrid model.

Figure 2.5(a) shows the real-space crystal structure of 1T-$TiSe_2$ above the critical temperature. According to the 1T structure, the transition-metal

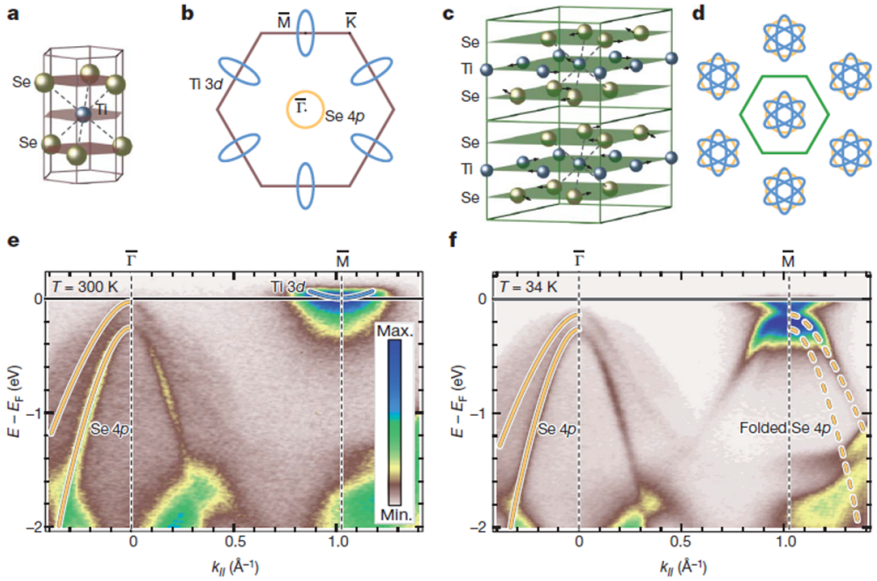

Fig. 2.5: (a) Real space unit cell of the undistorted structure above the critical temperature. (b) First surface projected Brillouin zone in the undistorted phase above the critical temperature. Blue ellipses and yellow circles represent the Fermi surface topology of Ti 3d and Se 4p bands, respectively. (c) Real space unit cell for the CDW/PLD phase. Samll black arrows show the PLD. (d) Surface projected Brillouin zone in the CDW phase. The folding os Ti 3d and Se 4p bands is reported. ARPES maps of 1T-$TiSe_2$ (e) above and (f) below the critical temperature. From [107].

atom is octahedrally coordinated with chalcogen atoms. At 202K, the system undergoes a phase transition to a commensurate 2x2x2 CDW/PLD structure, represented in Fig. 2.5(c): the atomic displacements pattern of the transition is shown by small arrows. Atoms displace in order to reach a 2H, trigonal prismatic, structure. The atomic displacement is about 0.085 $\mathring{A}$ for Ti atoms and it is about 0.028 $\mathring{A}$ for Se [14]. A three-dimesional CDW with wavevector $\mathbf{q} = (\frac{1}{2}, \frac{1}{2}, \frac{1}{2})$ is associated with to the PLD described before. This strongly affects the electronic band structure of the system. Focusing only into the k_x, k_y-plane, the CDW wavevector connects the center of the surface-projected hexagonal Brillouin zone (see Fig. 2.5(b)) $\bar{\Gamma}$ with the high-symmetry point $\bar{M}$. Below the critical temperature, the Brillouin zone halves in all directions due to the 2x2x2 transformation real-space. Thus, the pristine $\bar{M}$-point corresponds to a novel $\bar{\Gamma}$-point in the CDW ground-state as shown in Fig. 2.5(d). This implies that the bands at the $\bar{\Gamma}$-point and $\bar{M}$-point fold onto each-other. Figure 2.5(b) shows the Fermi surface

topology for the undistorted 1T-structure. Around the $\bar{\Gamma}$ point, hole-pockets originating from Se 4p valence bands are observable while at the $\bar{M}$-points there are electron-pockets due to Ti 3d conduction bands states. As shown in Fig. 2.5(d), in the CDW phase, the Ti 3d-electron pockets appears around the center of the Brillouin zone $\bar{\Gamma}$ while Se 4p states fold onto the pristine $\bar{M}$-point, i.e. the $\bar{\Gamma}$ point of the secondaries CDW Brillouin zones.

As seen so far, a strongly modification of the electronic band structure characterizes the CDW phase transition. For this reason, ARPES is a powerful technique to characterize this fingerprint and identify the interaction underlying the phase-transition. An example of ARPES spectra above and below the critical temperature is reported in Fig. 2.5(e) and (f). Above the critical temperature (Fig. 2.5(e)), 1T-$TiSe_2$ is a semimetal characterized by a two-splitted Se 4p valence band at the $\bar{\Gamma}$ point and a Ti 3d conduction band at the $\bar{M}$-point. The top of the Valence Band (VB) crosses the Fermi level with anegative energy gap of ≈ -20 meV. Other ARPES measurements report an indirect semiconductor character with a bandgap about 150 meV [108, 112–115]. This difference arises from defects and doping effects. Below the critical temperature all ARPES measurements on 1T-$TiSe_2$ have reported some common features shown as example in Fig. 2.5(f), fingerprints of the CDW/PLD phase:

i) a very intense folded valence band is observed at the $\bar{M}$-point;

ii) the maximum of the valence band and the minimum of the conduction band shift to lower binding energy leading to a total energy gain of about 80 meV;

iii) a flattening of the top of the valence band and of the bottom of the conduction bands. In particular, the conduction band minimum is no more at the $\bar{M}$-point.

While the non-metallic character and the large anisotropy of electron and holes pockets at the Fermi surface (see Fig. 2.5(b)) allow to rule out the role of Fermi surface nesting [108], unfortunately these observed fingerprints do not lead to an unambigous identification of the mechanism underlying the CDW/PLD formation. The lowering of valence and conduction bands is in agreement with a modified Jahn-Teller scenario. The atomic displacements reported in Fig. 2.5(c) represent a shortening of the local Ti-Se bonding length and a modification of the local crystal field around the Ti atoms. These lead to a lowering of the average energy of conduction and valence bands close to the Fermi surface through a distortion-enhanced partial charge transfer between neighbouring 3d ad 4p orbitals [108, 113, 116].

Since this scenario naturally comes out from the PLD, it cannot explain the large spectral weight carried by the folded bands in the CDW ground state [14, 112, 116–118]. In addition, tight binding calculations have shown that a lattice displacement twice as big as the experimental one is required to explain the observed opening of the band gap [14] (see Fig. 2.6(c) and (d)). Thus, the Jahn-Teller based scenario actually requires a sort of enhancement of the electron-phonon coupling during the transition to justify the experimental value of the energy band gap opened by the CDW formation.

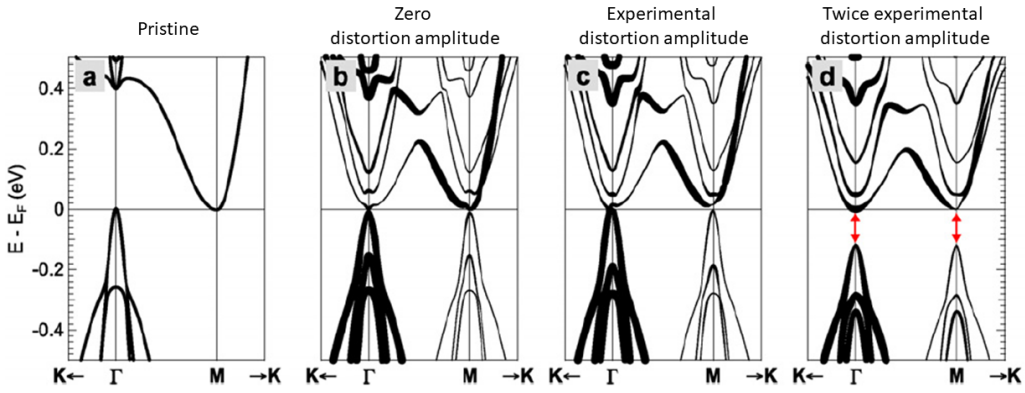

Fig. 2.6: Tight-binding band structure of 1T-$TiSe_2$ for (a) unreconstructed and reconstructed (b) with zero distortion amplitude, (c) experimentally reported distortion amplitude, (d) twice the experimental distrortion amplitude. Thickness of the lines is proportional to the spectral weight carried by the bands. Red arrows mark the opening of a band gap. From [14].

However, electron-phonon interactions mechanism transfer only a small amount of spectral weight in the folded band [14, 112, 116, 117]. As seen for the simple 1D-case in sec. 3.1.7, the large redistribution of spectral weight in the folded bands is characteristic of the excitonic insulator scenario. A comparison between the spectral function calculated for the excitonic insulators model in 1T-$TiSe_2$ and ARPES measurements is reported in Figure 2.7. Figures 2.7(a) and (b) are ARPES spectra at $\bar{\Gamma}$ (left panel) and $\bar{M}$-point (right panel) above and below the critical temperature, respectively. These should be compared with Figure 2.7(c) and (d) reporting the calculated spectral weight in the assumption of an excitonic insulator scenario. Clearly, a good agreement between theoretical predictions and experimental data can be observed.
However, is not clear how electron-hole interaction alone could lead to a perfectly commensurate PLD [116]. All the observed features are explained by

a modified Jahn-Teller - electron-hole interaction hybrid model [119].
The recent observation above the critical temperature of a diffuse residue of CDW- folded valence band at the M-point leads to the formulation of a different mechanism [120]: the excitonic condensate. The residual spectral weight represents the presence of incoherent excitonic pairs that condensate at the critical temperature in a coherent Bose-Einstein condensate ground state. This drives, as in BCS for Cooper pairs condensation, the opening of a band gap. However, as in the case of the excitonic insulator, even this scenario is not able to explain the perfect commensurate CDW/PLD since there is no lattice coupling in the model [116]. The same high-temperature features have been explained in terms of the hybrid model considering the presence of excitons above the critical temperature [116]. The absence of an electron-hole nesting vector does not allow the formation of CDW even if excitons are present. Only when the renormalization of the elctron-phonon coupling due to the excitons becomes strong enough, i.e. at the critical temperature, the transition occurs and the CDW is naturally commensurate to the lattice.

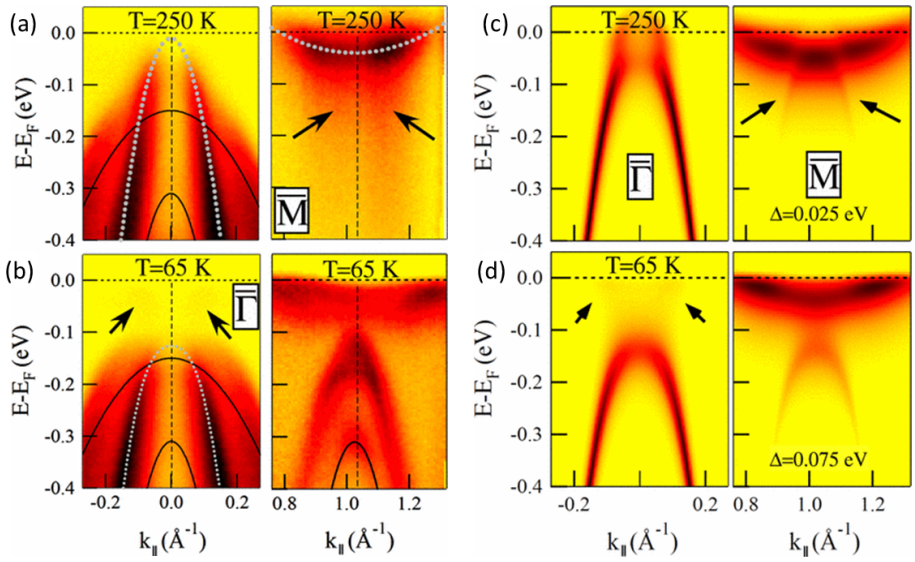

Fig. 2.7: ARPES maps at the $\bar{\Gamma}$-point (left panel) and at the $\bar{M}$-point (right panel) (a) above and (b) below the critical temperature to be compared with the theoretical spectral function in an excitonic scenario (c) above and (d) below the critical temperature. From [112].

Recently, scanning-tunnel microscopy measurements have reported for the first time a short range coherence of the CDW domains suggesting a strong-coupling regime (see section 2.1.6) and then a local bonding scenario that naturally leads to a pseudo Jahn-Teller description [121]. The excitons are an accidental consequence of the more favorable direct coupling in the distorted band structure and excitons-phonon coupling could reinforrce the CDW. In contrast, very recent measurements conducted with a novel technique (momentum-resolved electron-energy-loss spectrscopy (M-EELS)) claimed the first observation of the excitonic condensation in 1T-$TiSe_2$ [13].
Due to the large number of possible explainations all consistent with subsets of the extensive experimental and theoretical results, a general consense about the driving force of CDW phase transition in 1T-$TiSe_2$ does not exist.

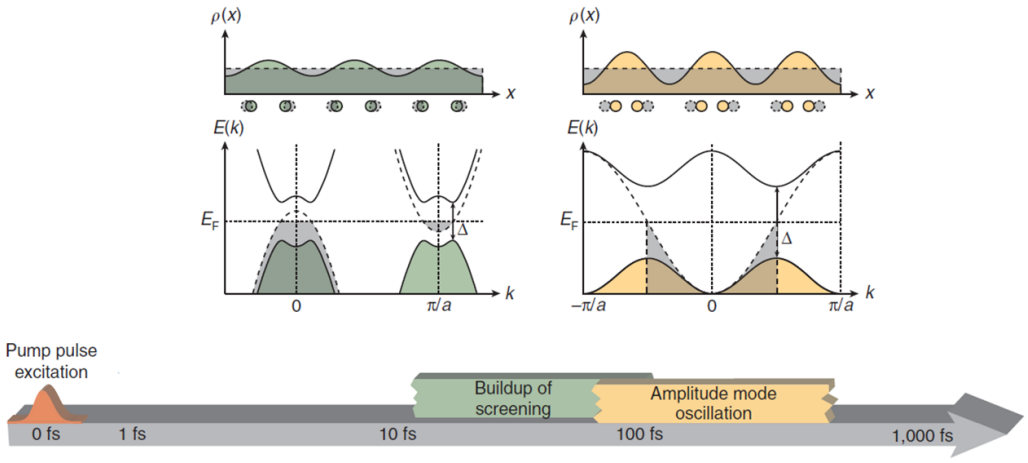

Fig. 2.8: (a) excitonic insulator and (b) Peierls insulator scenarios. The insulating phase is marked by solid curves and coloured shading while the metallic phase is indicated by dashed curves and grey shading. (c) Characteristic time-scale of the main driving mechanism of the scenarios (a) and (b) upon pump excitation. From [122].

The ambiguity about the dominant interaction in the CDW transition of 1T-$TiSe_2$ is due to the fact that, in real complex materials, electron-electron and electron-phonon interactions are simultaneously strong [122]. Then, the classification in terms of dominant Peierls mechanism or excitons role is not straightforward. In addition, we want to point out that the most prominent feature of the CDW ground state, i.e. the resulting insulating gap in the electronic spectrum appears the same in steady-state spectroscopies for both mechanisms discussed above [106, 122]. While these two interac-

tions, electron-electron and electron-phonon scattering, may be degenerate in energy and then hard to resolve in time-integrated spectroscopies, they are extremely different in the time-domain as depicted in Figure 2.8 [122–124]. Purely electronic interactions like electronic screening at the base of the excitonic insulator mechanism occur in fact on a typical timescale of tens of femtosecond. In contrast, interactions between electronic population and lattice require a longer time (hundreds of femtoseconds) because of the larger mass of the ions. Following this observation, out-of-equilibrium spectroscopies are fundamental tools to disentangle the mechanisms dominating quantum matter. Thus, metal-to-insulator transitions can be more reliably classified according to the gap melting characteristic time.

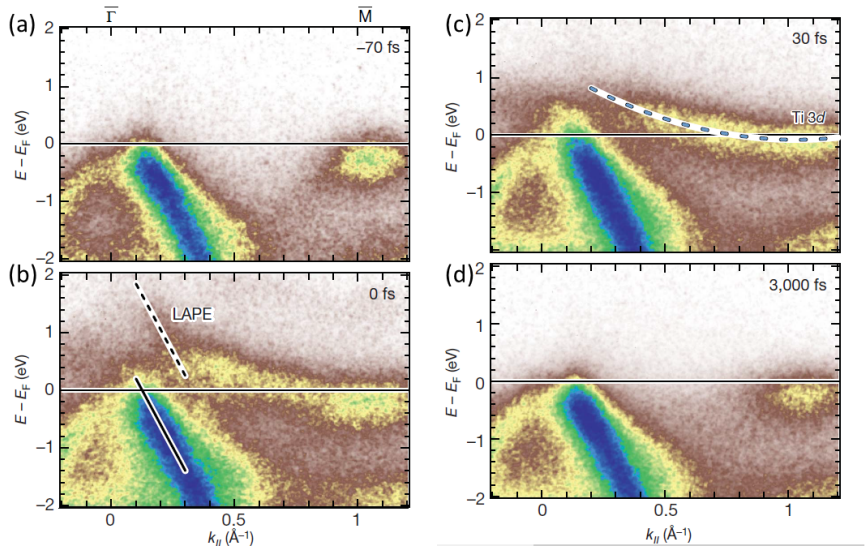

Fig. 2.9: TR-ARPES maps at different pump-probe delays: (a) before the pump arrival, (b) time-zero, (c) 30 fs after the photoexcitation and (d) at 3 picoseconds. From [107].

Figure 2.9(a) shows ARPES map of 1T-$TiSe_2$ along the $\overline{\Gamma M}$ direction using sub 10-fs extreme ultraviolet pulses (XUV) ($h\nu = 43$eV) at T=125K, i.e. in the CDW phase, from [107]. Despite the poor energy resolution due to the intrinsic broadening associated with ultrashort femtosecond pulses, the hole-like parabolic VB at the $\bar{\Gamma}$-point is clearly visible. In addition, signature of the folded VB at the $\bar{M}$-point is retrieved. Exploiting an intense ultrashort infrared laser pulse ($h\nu = 1.57$eV and 32 fs-pulse width, optical fluence about 5 $\frac{mJ}{cm^2}$), the system is brought out-of-equilibrium. The increment of the effec-

tive electronic temperature due to the pump excitation drives the transition to the metallic phase allowing to investigate the underlying mechanism in the time domain. However, XUV-based time-resolved ARPES experiments focused on the dynamics of the folded bands at the $\bar{M}$-point rather then of the closing of the insulating gap upon optical excitation [107, 122]. Figures 2.9(b,c) show the disappering of the folded VB at the M-point within 30 fs after the pump optical excitation. Moreover, the pristine electron-like parabolic conduction band at the $\bar{M}$-point appers together with the disappearing of the folded VB. These experimental observations hint for the loss of the long-range charge order on the tens of femtoseconds time-scale suggesting an electronic screening-dominated mechanism, i.e. the excitonic insulator scenario [107, 122]. In addition, the ultrafast spectral response of 1T-$TiSe_2$ has been found different with respect to the paradigmatic Peierls insulators transition metal dicalchogenides enforcing the conclusion of the excitonic-dominated scenario [122]. We point out that a partial recovery of the folded VB at the $\bar{M}$-point occurs on the several picoseconds time scale (see Fig. 2.9(d)) suggesting a fundamental role of lattice in the thermalization process of the electronic subsystems [107]. Recently, out-of-equilibrium optical spectroscopy measurements have been able to disentangle the excitonic and PLD response [125]. They demonstrate that even when the excitonic order of the CDW phase is completely quenched by the optical excitation, the lattice distortion is still present in a coherently excited state. This observation suggests that excitons alone are not the only character driving the metal-to-insulator transition in 1T-$TiSe_2$. Also the lattice plays a fundamental role. Moreover, recent time-resolved ARPES measurements with near- and midinfrared photon pump excitations [126] have pointed out a greater and more fundamental role of the electron-phonon interaction in the CDW phase transition of the 1T-$TiSe_2$ re-opening the question about the nature of the CDW ground state in this peculiar transition metal dicacholgenide.
Our time-resolved ARPES measurements focus for the first time on the temporal evolution of the CDW order parameter, i.e the insulating gap, and suggest a complex interplay between excitonic population and lattice [15]. These results are shown in Chapter 5 of the present thesis.

Chapter 3

Time-resolved and Angle-resolved photoemission spectroscopy (TR-ARPES)

Tomorrow is gaining speed on you
It's all you want to do
You, you know where to run
You run electron blue

Electron Blue
from Around the Sun (2004), R.E.M.

In this Chapter, after an introduction about steady-state ARPES, we will provide a description of out-of-equilibrium spectroscopies. In conclusion, details about TR-ARPES, the most exploited technique in this thesis, will be addressed.
Angle-resolved photoemission spectroscopy (ARPES) provides a unique insight allowing a direct access to the band structure and many-body interactions of solids. Steady-state ARPES developed in the past decades to high resolution both in energy and momentum. However, ARPES probes only occupied states.
The fast development in these years of mode-locked ultrashort pulsed lasers leads nowadays to a wide class of out-of-equilibrium spectroscopies allowingto study the temporal evolution of the excitations. Since the proper timescale for many-body correlations differs over a two-orders of magnitude (typically 10-1000 fs), these techniques provide a terrific way to directly disentangle several interactions. In this context, time-resolved ARPES (TR-ARPES) occupies a special role allowing to track electronic and many-body excitations

dynamics directly in their quantum state space, i.e. the electronic band structure.

3.1 Photoemission spectroscopy in a nutshell

Angle-resolved photoemission spectroscopy (ARPES) is a technique based on the Hertz-Einstein photoelectric effect [127]. A photon with energy larger than the work function of a solid Φ (tipically $4 - 5$ eV) impinges on a material. Then, electrons come out from the surface of the material carrying information about their quantum state inside the solid. At variance with other spectroscopies, ARPES provides the unique capability to directly access the quantum band structure of the materials, fundamental for a deep understanding of materials properties such as superconductivity, magnetism and exotic phase-transitions.

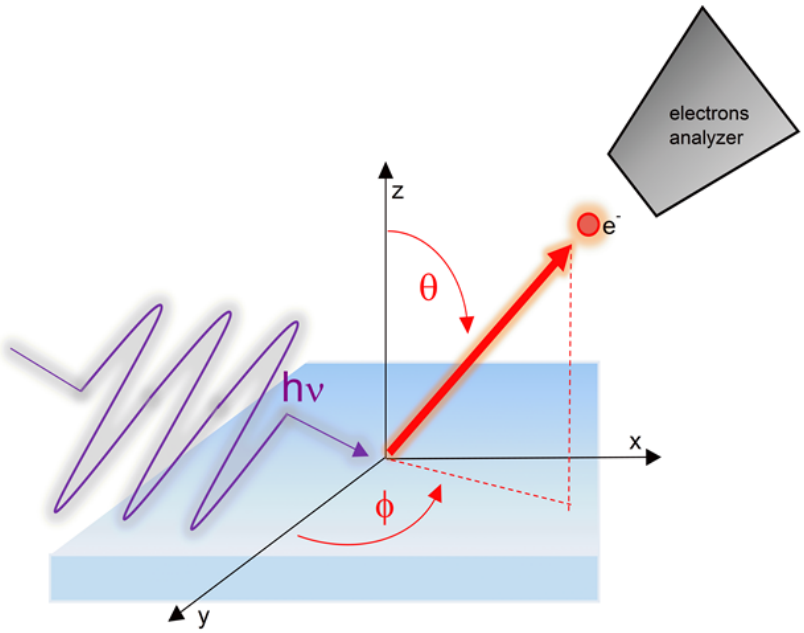

Fig. 3.1: Scheme of an ARPES experiment, photons with energy $h\nu$ photoemit electrons detected by an electron analyzer under an angle of emission θ.

The general geometry of an ARPES experiment is sketched in Fig. 3.1: a monochromatic photon beam of energy $h\nu$ (with $h\nu > \Phi$) provided by a gas-discharge lamp, synchrotron beamline or laser source hits a properly aligned single crystal. This promotes an electron above the vacuum level E_{Vacuum}. Thus, the electron is photo-emitted with a certain kinetic energy E_{kin} and a direction defined by angles θ and ϕ. For the study of condensed matter the goal is to relate measured quantities (energy and angles) to binding energy and crystal momentum of electrons propagating in the solid, i.e. the band dispersion $E(\mathbf{k})$ [128].
By energy conservation law we can easily relate the kinetic energy and the binding energy:

$$E_B = h\nu - E_{kin} - \Phi, \tag{3.1}$$

where $E_B = 0$ corresponds to E_{Fermi}, i.e. the energy above which all states, at $T = 0K$, are empty. Then, from the spectrum of detected photoelectrons it is possible to obtain the band energy of the solid as shown in Fig. 3.2(a).

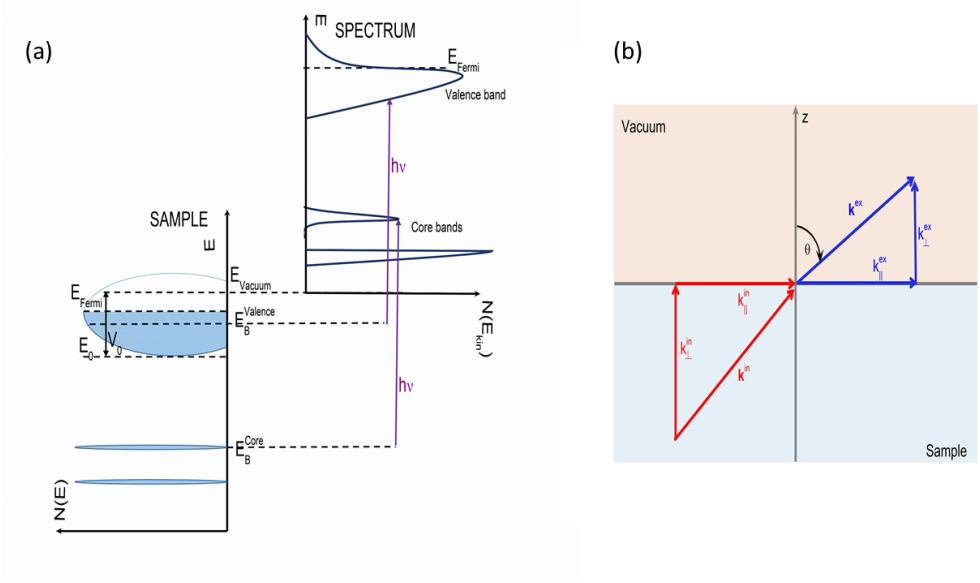

Fig. 3.2: (a) Relation between energy levels of the sample and the spectrum of detected photoelectrons. (b) Conservation of the parallel component of the momentum upon transmission through the surface between sample and vacuum.

Accessing the momentum is a bit trickier. We have in fact to consider that the presence of the vacuum-solid interface causes an abrupt change in the crystal potential in the normal direction z. The momentum-component along this

direction, $k_\perp$, is then a not-good quantum number and it is not conserved through the surface. Fortunaly, even if the surface breaks the traslational symmetry, the parallel component, $\mathbf{k}_{||}$, of momentum is conserved. By geometrical considerations (see Fig. 3.2(b)) we have

$$\mathbf{k}_{||}^{\mathbf{in}} = \mathbf{k}_{||}^{\mathbf{ex}} = \sqrt{\frac{2mE_{kin}}{\hbar^2}} \sin\theta, \tag{3.2}$$

valid for any given angle ϕ. Conducting measurements as function of both geometrical angles allows to determine the two in-plane component k_x, k_y. The ARPES intensity distribution in the (k_x, k_y) plane at costant energy represents a cut of the band structure in the surface-projected Brillouin zone. At the Fermi level, we have the Fermi surface whose topology is responsible for the main macroscopic properties of the crystal such as metallicity, magnetism and charge-order.

Relation 3.2 is strictly valid in the approximation that the momentum associated to the photon is negligible and then only vertical optical-transitions, i.e. satisfating the relation $\mathbf{k}_{initial} = \mathbf{k}_{final} + \mathbf{G}$ where $\mathbf{G}$ is the reciprocal lattice vector, are triggered by the photon. This is in general a good approximation for photons having energy less than 100 eV. This assumption implicitly imposes a condition also on $k_\perp$. The knowledge of $k_\perp$ is fundamental for mapping completely the three-dimensional band but it is undetermined in ARPES. The assumption of a negligible momentum carried by a photon imposes that initial and final states in the photoemission process are linked by vertical transition.Thus, an *a priori* knowledge of the final state dispersion is required to access $k_\perp$. Unfortunately, the final state is in general unkown [128]. However there is a generally accepted approximation to $k_\perp$. The effect of the surface is approximated with a step potential of value V_0 that is the so-called "inner potential", i.e. the energy of the bottom of the valence band with respect to the vacuum level (see Fig. 3.2(a)); if we assume that the final state is a free-electron's plane wave like, we can obtain $k_\perp = \frac{1}{\hbar}\sqrt{2mE_{kin}\cos^2\theta + V_0}$. V_0 can be found observing the periodicity of the dispersion $E(k_\perp)$; in an experimental way this is possible by scanning photoelectrons emitted only in normal direction as function of the radiation's energy (eg. using synchrotron light) [129].

For some systems, the lack of information about $k_\perp$ is not so relevant: this is the case of low-dimensional systems in which the electronic structure is strongly anisotropic and withouth dispersion in the direction normal to the surface (eg. 2D superconducting cuprates, 2D layered transition metal dichalcogenides and 1D linear atomic chains materials). We highlight that also the surface states, like Shockley's state in metal or the spin-polarized surface state characteristic of the topological insulators (see Chapter 1), are

completely described by their $\mathbf{k}_{||}$ dispersion. ARPES on these materials allows us to study their properties directly in the 2D reciprocal space, i.e. the quantum space of the electronic states.

3.1.1 One-step model

Many-body effects are due to the interactions among electrons or with other excitations inside the crystal, and are responsible for many interesting phenomena like, for example, superconductivity, magnetism, charge-density waves. They are very rich of physical interest but a many-body problem is generally very hard to calculate and to understand completely. ARPES spectra contain information about these interactions. If the system is largely anisotropic and it is possible to neglect the dispersion in $k_\perp$, the imaginary part of the self-energy, the complex function describing all deviations from the non-interacting ideal systems, is accessible looking at the linewidth of the peaks in ARPES [129]. For a three-dimensional system it is not so simple and a complete theoretical description should be considered. ARPES signal is related to the many-body interactions in solids through the one-particle removal spectral function $A_{\mathbf{k}}(E_B)$. In this section, we will introduce basically the theory of many-body interactions in ARPES.
The most successful framework to depict the photoemission from solid surfaces is the one-step model. The main idea is to describe the photoemission mechanism as a single quantum-mechanically coherent process including all multiple-scattering events due to the different layers of the solid. This allows us to consider the effects of excitation on the energy spectrum of the photoelectrons or to deal with the photoemission from surface states, resonance states or with transitions involving evanescent bandgap states [129, 130].
Within the many-body theory framework, the photocurrent can be calculated from the transition probability in a first-order time-dependent perturbation theory. Here $\hat{H} = \hat{H_0} + \hat{\Delta}$ is the N-electron system Hamiltonian with H_0 being the unperturbed Hamiltonian. $\hat{\Delta}$ is a small perturbation due to the impinging electromagnetic radiation. Two N-electrons eigenstates of $\hat{H}$ are $\left|\Psi_i^N\right\rangle$ and $\left|\Psi_f^N\right\rangle$, respectively initial and final state of the transition. The transition probability per unit time $w_{f,i}$ is given by Fermi's Golden Rule:

$$w_{f,i} = \frac{2\pi}{\hbar} |\left\langle \Psi_f^N | \hat{\Delta} | \Psi_i^N \right\rangle|^2 \delta(E_F - E_B - \hbar\omega). \tag{3.3}$$

Dirac delta $\delta(E_F - E_B - \hbar\omega)$ ensures energy conservation between N-electron initial and final states. Within the electromagnetic dipole approximation, the interaction $\hat{\Delta}$ with the photon can be written as

$$\hat{\Delta} = \frac{e}{m_e c} \hat{\mathbf{A}} \cdot \hat{\mathbf{p}}, \tag{3.4}$$

where e is the fundamental electron charge, c the speed of light, m_e the electron mass. $\hat{\mathbf{A}}$ is the electromagnetic vector potential while $\hat{\mathbf{p}}$ is the electrons momentum operator. The photocurrent is derived from eq.(3.3) and can be written as [130]

$$I(\hbar\omega) = \frac{1}{\hbar}\sum_{f,i} M_{f,i}^{\mathbf{k}\,*} A_{\mathbf{k}}(E_B) M_{f,i}^{\mathbf{k}}. \tag{3.5}$$

Here,

$$A_{\mathbf{k}}(E_B) = \sum_n |<\Psi_n^{N-1}|\hat{a}_{\mathbf{k}}|\Psi_i^N>|^2 \delta(E_F - E_B - \hbar\omega) \tag{3.6}$$

and

$$M_{f,i}^{\mathbf{k}} = \left\langle \phi_f^{\mathbf{k}}|\hat{\Delta}|\phi_i^{\mathbf{k}} \right\rangle. \tag{3.7}$$

$A_{\mathbf{k}}(E_B)$ is the one-electron removal spectral function and $\hat{a}_{\mathbf{k}}$ is the fermionic annihilation operator which removes a particle with momentum $\mathbf{k}$. $A_{\mathbf{k}}(E_B)$ is related to the Density of States (DOS) by [131]

$$DOS(E) = \frac{1}{V}\sum_{\mathbf{k}} A_{\mathbf{k}}(E), \tag{3.8}$$

V is BZ's volume. We can relate $A_{\mathbf{k}}(E_B)$ to the system self-energy, i.e. to the correlations and interactions inside the crystal.
The one-electron removal spectral function (3.6) is connected to the retarded-Green function of the interacting system, i.e. the propagator in the linear response theory, by

$$A_{\mathbf{k}}(E_B) = -\frac{1}{\pi}\,\mathrm{Im}\{G_{\mathbf{k}}(E_B)\}. \tag{3.9}$$

Moreover, Green function satisfies Dyson's equation

$$G_{\mathbf{k}}(E_B) = G_{\mathbf{k}}^0(E_B) + G_{\mathbf{k}}^0(E_B)\Sigma_{\mathbf{k}}(E_B)G_{\mathbf{k}}(E_B), \tag{3.10}$$

where $G_{\mathbf{k}}^0$ is the one-electron propagator of the non-interacting system and $\Sigma_{\mathbf{k}}(E_B)$ is the self-energy, a complex function that represents all deviation from non-interacting systems, i.e. all many-body interactions [132].
By eq.(3.10), using expression of $G_{\mathbf{k}}^0$ in [133] and eq.(3.9), we can write the one-electron removal spectral function as a function of the imaginary and real part of the self-energy:

$$A_{\mathbf{k}}(E_B) = -\frac{1}{\hbar\pi}\frac{\mathrm{Im}\{\Sigma_{\mathbf{k}}(E_B)\}}{(E_B - \epsilon_{\mathbf{k}} - \mathrm{Re}\{\Sigma_{\mathbf{k}}(E_B)\})^2 + \mathrm{Im}\{\Sigma_{\mathbf{k}}(E_B)\}^2}, \tag{3.11}$$

$\epsilon_{\mathbf{k}}$ is the single-particle energy by calculation of the band structure (e.g. Density Functional Theory (DFT) or tight-binding models). These are Lorentzian

where $\mathrm{Im}\{\Sigma_{\mathbf{k}}(E_B)\}$ is the linewidth while the peak position is given by $\epsilon_{\mathbf{k}} + \mathrm{Re}\{\Sigma_{\mathbf{k}}(E_B)\}$.
Then, the photoelectron spectrum is strongly dependent on many-body interactions which dress the electron. They cause a shift of the energy peaks due to the real part of the self-energy that can generate also extra features where $\mathrm{Re}\{\Sigma_{\mathbf{k}}(E_B)\}$ is strongly dependent on the energy (e.g. in strongly correlated material). On the other hand, the imaginary part causes damping processes that appear in the finite life-time of the initial state [130].
Because the many-body interactions are characterized by energy and life-time, physical observables usually associated with particles, it is convenient to describe these interactions in the quasi-particle scheme. In other words, we describe the particles and the associated excitations like a unique physical entity. So, the electron is not isolated but it is dressed, for example, by the other electrons (electron-electron scattering) or by the phonons (electron-phonon scattering).
All interactions in the solid are fully described by the real and imaginary part of the self-energy and we can derive these two quantities from ARPES spectrum trough eq.(3.11). In principle, we can derive the self-energy directly from the energy distribution curves (EDCs) looking at the shift of the peak. However, this is hard because of the presence of the background, of the non-trivial self-energy dependence on E_B and of the cut-off due to the Fermi level [129].
A common method to obtain the self-energy is the analysis of momentum-distribution curves (MDCs) which is done by plotting ARPES map cuts at costant energy $\tilde{E_B}$ [134]. Assuming that the self-energy does not depend on $k_\perp$ and supposing to know the dispersion relation $\epsilon_{\mathbf{k}}$ and the group velocity $v_{\mathbf{k}}$ at a given point $\mathbf{k}$ for the non-interacting electronic system, the MDCs have Lorentzian shape [134]. By performing a fit it is possible to obtain the real and the imaginary parts as:

$$\mathrm{Re}\{\Sigma_{\mathbf{k}}(E_B)\} = \tilde{E_B} - \epsilon_{\mathbf{k}}, \quad \mathrm{Im}\{\Sigma_{\mathbf{k}}(E_B)\} = \hbar v_{\mathbf{k}} \Delta\mathbf{k}. \tag{3.12}$$

Here $\Delta\mathbf{k}$ is the full-width at half-maximum (FWHM) of the fitted lorentzian.

The term $M_{f,i}^{\mathbf{k}}$ in eq. 3.7 is the one-particle matrix element. At this stage, to obtain eq.(3.5) we have assumed only the so-called sudden approximation. In this approximation $\left|\Psi_F^N\right\rangle$ is described as the product between a single-particle state $\left|\phi_f^{\mathbf{k}}\right\rangle$, which describes the photoemitted electron, and a N-1-electrons state $\left|\Psi_f^{N-1}\right\rangle$ describing the excited system. The latter one can be projected on states of the N-1 particles system with eigenfunctions Ψ_n^{N-1}

and eigenvalues E_n^{N-1}. So,

$$\Psi_f^N = A\phi_f^{\mathbf{k}} \sum_n \Psi_n^{N-1}. \tag{3.13}$$

Sudden approximation is equal to assuming that the removal of the photo-electron from the unperturbed system is so fast to ensure that the particle leaves the sample before the photo-induced holes relaxation takes place. In other words, we can neglect the electron-sample interaction [129, 130]. This approximation is generally good for electrons with kinetic energy larger than $15 - 20$ eV and then for impinging photons with energy larger than 20 eV [135]. For laser-based ARPES setup, that generally uses photons of 6 eV, this approximation is not so stricktly satisfied. However, experimental results [136] show that the electronic structures at the Fermi level are qualitatively unchanged for electrons of less than 2-eV kinetic energy and for high-photon energy ARPES experiments ensuring that the sudden approximation is still valid in low-energy measurements.
In evaluating eq. 3.5, we have also assumed Hartree-Fock approximation for the initial N-particles state [129]. Under Hartree-Fock approximation we can write the initial state many-particles wave function Ψ_i^N as a single Slater determinant product of a one-electron vector $\phi_i^{\mathbf{k}}$ and an (N-1)-particle term Ψ_i^{N-1}. Thus, the interaction matrix element in eq. 3.3 can be rewritten as

$$\left\langle \Psi_f^N | \hat{\Delta} | \Psi_i^N \right\rangle = \sum_n \left\langle \phi_f^{\mathbf{k}} | \hat{\Delta} | \phi_i^{\mathbf{k}} \right\rangle \left\langle \Psi_n^{N-1} \middle| \Psi_i^{N-1} \right\rangle, \tag{3.14}$$

where we used eq. 3.13 for the evaluation of the final (N-1)-particles state. The latter term in eq. 3.14 is the (N-1)-particles overlap integral whose square modulus represents the probability that the interaction leaves the many-particles system in the excited state $\left|\Psi_n^{N-1}\right\rangle$. The first term is the one-particle matrix element $M_{f,i}^{\mathbf{k}}$. This term plays a fundamental role in the photoemission intensity (see eq. 3.5). One-electron matrix element is extremely dependent on electron momentum $\mathbf{k}$ and on the energy and polarization of the impinging beam, i.e. the experimental geometry [129]. For some photon energy and experimental geometry, this term could even lead to a total suppression of the photoemission intensity [128, 129].
Under the sudden approximation and considering finite temperature's effects, we can rewrite eq. 3.5 as

$$I(\mathbf{k}, E_B) = I_0(\mathbf{k}, \nu, \mathbf{A}) f_{FD}(E_B, T) A(\mathbf{k}, E_B), \tag{3.15}$$

where $f_{FD}(E_B, T)$ is the Fermi-Dirac distribution at temperature T. The presence of Fermi-Dirac distribution in the photoemission intensity limites

the probed electronic states to the occupied ones. We will see in the next sections that multi-photons approaches are required to experimentally access the unoccupied band structure. The term $I_0(\mathbf{k}, \nu, \mathbf{A})$ is proportional to the squared modulus one-electron final and initial state dipole interaction matrix element $|M^{\mathbf{k}}_{f,i}|^2$ [129].

Relativistic corrections like spin and spin-orbit coupling are fundamental for understanding the properties of ferromagnetic materials and topological insulators. A photoemission theory of these materials has to consider the influence of relativistic effects to describe and to understand phenomena like dichroism, i.e. the difference in emission of spin-polarized photocurrent by excitation of circularly polarized light.
The relativistic photocurrent of photoelectrons of final energy ϵ_F and parallel momentum $\mathbf{k}_{||}$ is represented by the spin-density matrix ρ. More details can be found in [130].

3.2 Out-of-equilibrium ultrafast spectroscopies

In the past few decades, the emergence of mode-locked ultrashort pulsed lasers has triggered the development of new techniques to study the ultrafast electronic dynamics. It has been realized in fact that these lasers pulses create out-of-equilibrium conditions in condensed matter on a time-scale faster than the relaxation processes. This allows to observe novel phenomena not detectable at equilibrium.

Nowadays, out-of-equilibrium ultrafast spectroscopies are a fundamental tool for the investigations of condensed matter. This novel approach offers in fact the opportunity to unfold unsolved problems in solid state physics and in other branches of science. The femtoseconds-timescale allows to experimentally access the quasiparticles interaction in solids; electron-electron, electron-phonon scattering, etc. occur in this typical timescale as shown in Fig. 3.3. Purely electronic interactions are faster than the ones involving for example the lattice, i.e. phonons, leading to an experimental criterion for their identification. This represents a terrific advantage: while in the frequency, i.e. energy, domain certain mechanism are degenerate, in the time-domain it is possible to disentangle them unveiling the most important interactions in solid. Thus, it is possible to identify the main underlying mechanism of phenomena not-completely addressed by traditional spectroscopies, such superconductive or charge-ordered phase. In addition, the increased interest on quantum materials (like topological insulators) in view of

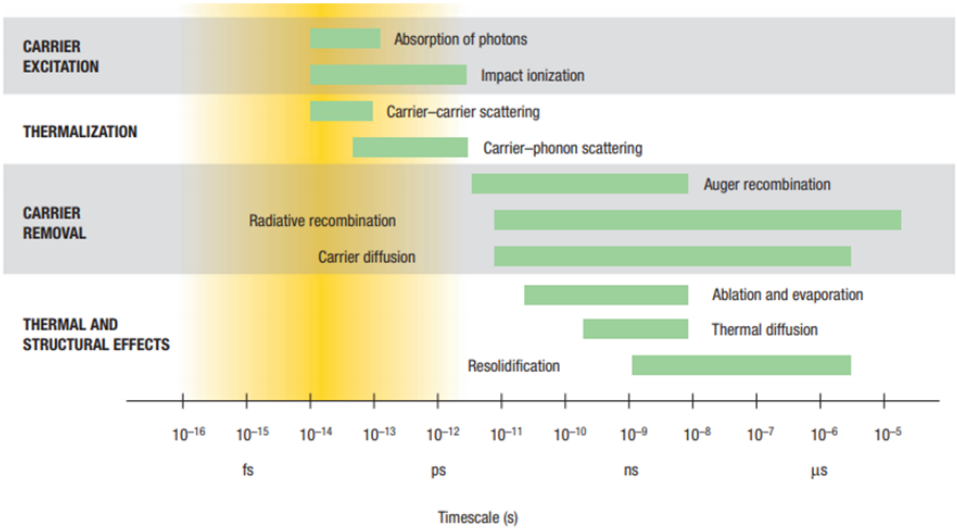

Fig. 3.3: Typical timescales of electron and lattice interactions in out-of-equilibrium solid. From [124].

faster generation of (opto-) electronic devices requires a deeper attention to the out-of-equilibrium phenomena.
The great success of these class of techniques can be attributed to the fact that, experimentally, a common single scheme can be applied to study a large variety of phenomena in different physical systems: the so-called pump-probe scheme [123]. In a nutshell, an ultrashort laser pulse (the *pump*) hits the sample leading to an out-of-equilibrium condition. Then, a second controlled delayed ultrashort pulse (the *probe*) provides a snapshot of the sample in the excited state. The nature of the probe determines the physical quantity we are interested in. It could be the intensity of reflected beam (TR- Reflectivity), the polarisation of the laser pulse (Kerr-effect) or the photoemission intensity (TR-ARPES). Changing the delay between pump and probe, it is possible to track the evolution of these observables in the time-domain. The characteristics of the two beams depend on the kind of observables that we want to study. In general, the pump is an optical pulse ranging from the infrared to the ultraviolet while the probe could be a broadband pulse (like for example time-resolved refelectivity or time-resolved magneto-optical Kerr-effect) or an X-ray pulse (like in the time-resolved X-ray diffraction).
Two are the foundamental experimental requirements for any pump-probe experiment:

- the size of the probe beam must be smaller than the size of the pump;

- the temporal length of pump and probe must be ultrashort.

The first requirement is to ensure that the probed region is homogeneously excited. The pulse duration determines the shortest timescale we can investigate. Thus, if one wishes to unreveal electronic dynamics, ultrashort (femtoseconds) pulses must be employed.

Depending on the investigated sample, three mainly frameworks related to the pump effect can be identified [123]:

- non-equilibrium spectroscopies;
- coherent excitation of bosonic-modes;
- ultrafast optical manipulation.

In the first framework, the aim is to investigate the out-of-equilibrium properties of the system using the pump mainly to create an initial non-equilibrium condition. To first approximation, a promotion of electrons into unoccupied states can describe the effect of the pump. If the perturbations is weak enough, the system relaxes back to the equilibrium conditions via the thermodynamical parameters ruling the equilibrium properties. From a microscopical point of view, the out-of-equilibrium population of electrons and bosonic modes (e.g. phonons) recovers to a quasi-equilibrium distribution, i.e. the same distribution at the equilibrium characterized by a higher effective temperature, with a proper timescale given by the equilibrium strength of the interactions (e.g. electron-phonon coupling). Time-resolved measurements shown in this work mainly belong to this first approach.

In the second approach, the general idea is to exploit any kind of impulsive excitation that directly couples with a bosonic mode such as spin/charge order or lattice vibrations. In this way, the pump triggers a coherent oscillation with a frequency proper of the mode and a relaxation time related to the de-tuning time, i.e. the lifetime of the coherent mode.

In the latter, the pump carries a strong excitation that drives the system extremely in out-of-equilibrium, triggering a phase transition to novel state-of-matter. This is the case for example of the so-called ultrafast demagnetization in which a strong pump pulse reduces dramatically the magnetization of a ferromagnet on a sub-ps timescale [137, 138]. In this approach, the excitation is indeed strong enough to induce several novel macroscopical photo-induced phenomena. We exploited this approach for example in the study of the photo-induced spin-current at the surface of topological insulators.

We point out that this is an arbitry classification strongly sample-dependent; in some case in fact all these main effects could realize together. It is, for example, the case of the layered transition metal dichalcogenides 1T-$TiSe_2$ as shown in Chapter 5 of this thesis.

3.2.1 Time- and angle-resolved photoemission spectroscopy

What we have described in the first section of this chapter, is the traditional steady-state ARPES. As seen in Sec. 3.1.1, the presence of the Fermi-Dirac distribution in the photoemission intensity (eq. 3.15) means that we can only access occupied states with this technique. In order to study unoccupied states, inverse photoemission spectroscopy (IPS) should be used. In IPS, an electron beam hits the sample emetting a photon which energy is related to the binding energy of the unoccupied state filled by the electron. Unfortunately, the cross section of this process is extremely low leading to a very small signal.
The development of pulsed lasers led to novel spectroscopies for the study of the unoccupied states: two-photon photoemission (2PPE) and time- and angle-resolved photoemission spectroscopy (TR-ARPES).
In the following, we will introduce TR-ARPES by which it is possible to access the unoccupied states and even the temporal dynamics of particles (and quasi-particles) in the reciprocal lattice.
TR-ARPES is developed on the pump-probe scheme illustrated so far. Figure 3.4(a) shows an example of a TR-ARPES map at a fixed pump-probe delay of 500 fs: we notice that there is photoemission signal even from bands above the Fermi level. The out-of-equilibrium states induced by the pump cannot be described by a Fermi-Dirac distribution, i.e. the unoccupied bands are filled by the optical pump pulse.
The experimental temporal resolution of a TR-ARPES setup is due to the convolution between pump and probe pulses, so in principle one desires the two beam's temporal lengths to be as short as possible. However, there is a limit due to Heisenberg principle; in fact, the shorter the pulse ($\bar{\Gamma}$ in Fig. 3.4(b)), the worse the energy resolution and some spectral features in the electronic band structures can be blurred like in Fig. 3.4(b).

Generally, TR-ARPES setups are based on an infrared Ti:Sapphire laser, with fondamental radiation $h\nu = 1.55$ eV, pulse duration $100 - 200$ fs [140, 141]. The fondamental radiation is used as pump, and its fourth-harmonic is used as UV probe (6.2 eV). The measurements shown in the Chapter 3

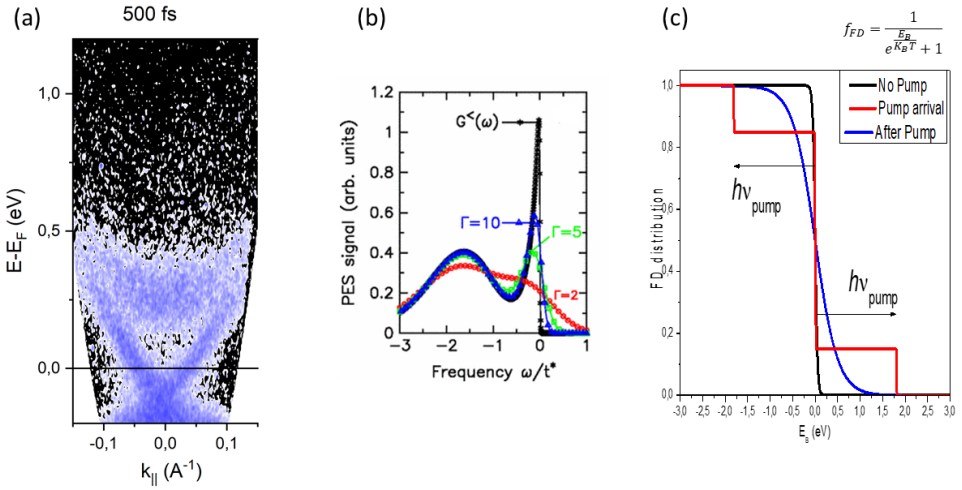

Fig. 3.4: (a) ARPES on topological insulator, at a fixed pump-probe delay; the solid black line indicates the Fermi level. (b) Blurring effects associated with the probe temporal width $\bar{\Gamma}$ on the TR-ARPES spectrum; in black is marked the continuous beam photoemission curve [139]. (c) Evolution of the electronic distribution upon pump excitation.

of this thesis work have been obtained on a slightly different setup recently developed in the laboratories of Politecnico di Milano (shown in Fig. 3.5). In synthesis, starting from a 100 kHz-repetition rate Yb:laser, a cascade of non-linear processes (such as Non-collinear optical parametric amplifier (NOPA) and sum-frequency generation (SHG)) provide a 1.85 eV 25-fs pump pulse and a 6.02 eV 65-fs transform limited probe pulse. More details are described in [2]. The principal limitation of this configuration is that, according to eq. 3.2, only a small region around the center of the Brillouin zone is accessible because of the low probing energy. To overcome this limit TR-ARPES setups based on high-harmonic generation in gas-phase have been developed [142–146]. The accessible probe energies typically range from 30 eV to 100 eV allowing to map the whole Brillouin zone. Unfortunately, the high pulse power required for laser high harmonic generation processes is available only with low repetition rate sources and, consequently, this setups are characterized by a very low signal-to-noise ratio. This leads in addition to a huge space-charge effect: at low-repetition rate, the photoemitted electrons feel the presence of the photoemitted electronic cloud making distortion in the electrons path into the analyzier. This originates artifact in the detected pho-

toemission signal [147]. For this reason, different schemes for high-repetition rate high-harmonic generation are being developed in these years [148–150].

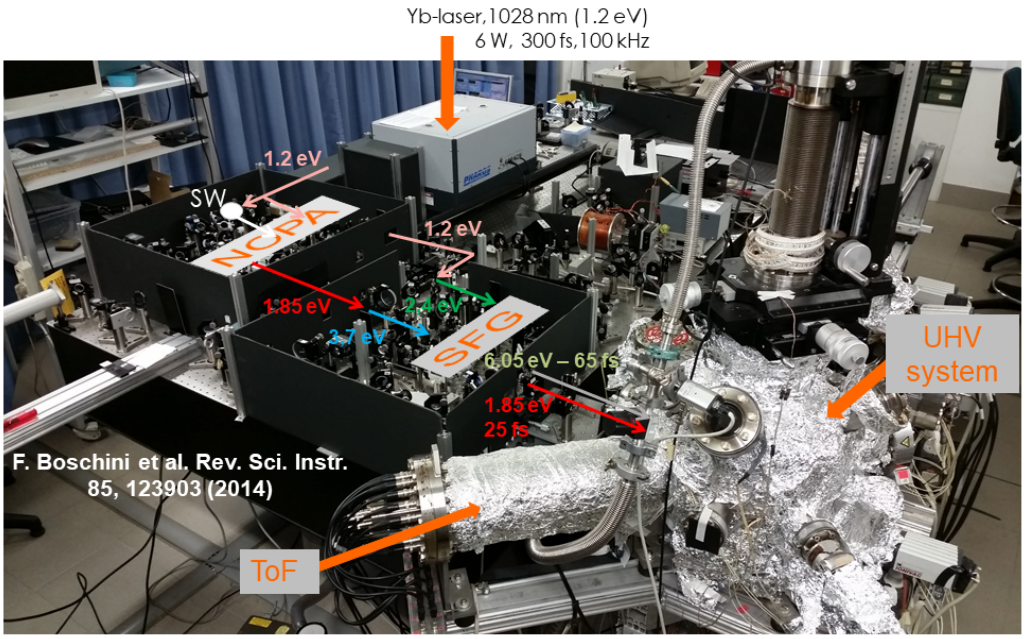

Fig. 3.5: Picture of the TR-ARPES setup employed in this thesis. Starting from the fundamental frequency of an Yb: laser a 1.85 eV 25-fs pump pulse and a 6.02 eV 65-fs transform limited probe pulse are provided by a cascade of non-linear processes. NOPA: non-collinear parametric amplifier, SFG: sum-frequency generation. More details in Ref. [2].

The study of non-equilibrium phenomena in solids by TR-ARPES is not trivial. One of the main problems emerging from TR-ARPES measurements is the data interpretation. The conventional interpretation of TR-ARPES is ideally depicted in Fig. 3.4(c): at room temperature the electronic distribution of the system is described by a Fermi-Dirac distribution (black line). The $h\nu$ pump excites electrons from a range of energy $h\nu$ below the Fermi level into empty states (red line). In other words, the pump creates non-thermal electronic distribution. Then, due to scattering processes (commonly electron-electron and electron-phonon), excited electrons gradually cool thermalizing in a new Fermi-Dirac distribution with a larger effective electronic temperature (T^*_{el}) (blue line) within tens to hundreds of femtsoseconds. Focusing on the Fermi level, TR-ARPES can be used to estimate different values of T^*_{el} at different delays between the pump and the probe

pulses [59, 61]. Recently, a novel approach based on the temporal evolution of the quasi-particles interactions trough a careful investigation of the dynamical one-electron spectral function have been sucessfully exploited to the study of the superconducting phase-transition in high-T_C cuprates [151].
A dynamical extension of the one-step model (see Sec. 3.1.1) has recently been developed [139]. The most remarkable result of this theory is that the pump-probe photocurrent is proportional to the lesser Green function $G^{<}_{\mathbf{k}_{||}}(\omega)$ that provides the description of the time evolution of the electronic structure on a femtosecond time scale following a strong pump pulse [152]. For an interacting system in equilibrium the lesser Green function is simply related to the spectral function and the electronic distribution by the relation:

$$G^{<}_{\mathbf{k}_{||}}(\omega) = iA_{\mathbf{k}_{||}}(\omega) f^0_{FD}(\omega). \tag{3.16}$$

This relation is important because it proposes useful Ansatz if the equilibrium distribution function $f^0_{FD}(\omega)$ is replaced by some unkown non-equilibrium function. This is the common interpretation of TR-ARPES data but in the lesser function there is more. In fact, we have seen in section 1.4 that $A_{\mathbf{k}_{||}}(\omega)$ is strongly dependent on many-body interactions and a very high pump fluence is a strong Couloumb interaction that affects the many-body correlations. In this case, also the sudden approximation can fail for very slow electrons (e.g. electrons close to the bottom of valence band): they are too slow to escape the correlations such as electron-electron screening due to the strong Couloumb interaction. All this can modify the detected spectra with extra features also below the Fermi level complicating the interpretation of TR-ARPES spectra.
We have seen in Sec. 3.1.1 that photoemisison intensity can be related to one-electron spectral function trough eq. 3.15. This relation is strictly valid only at equilibrium. As described so far, in the presence of pulsed electric fields, the proper description of the photoemission intensity involves the lesser Green function. However, as soon as the system reaches a quasi-equilibrium distribution characterized by an effective-temperature T^*_{el}, eq. 3.15 can be extended to describe the photoemission signal. According to eq. 3.15, defining as τ the pump-probe delay, we can describe the photoemission intensity as

$$I(\mathbf{k}, E_B, \tau) \approx |M^{\mathbf{k}}_{f,i}(\tau)|^2 f_{FD}(E_B, \mathbf{k}, T^*_{el}(\tau)) A_{\mathbf{k}}(E_B, \tau). \tag{3.17}$$

The evolution of $f_{FD}(E_B, \mathbf{k}, T^*_{el}(\tau))$ as a function of τ describes the relaxation processes for any binding energy E_B at any $\mathbf{k}$, i.e. the quasi-particle dynamics. Observed ultrafast metal-to-insulator phase transitions [15, 107] or superconducting gap-filling via ultrafast quenching of phase coeherence

in cuprates [151] are paradigmatic examples of the temporal evolution of the one-particle spectral function $A_{\mathbf{k}}(E_B, \tau)$, i.e. of the many-body interactions. The matrix element $|M^{\mathbf{k}}_{f,i}(\tau)|^2$ can evolve via modification of the initial and final states wavefunctions due to the activation of bosonic modes. To our knowledge, direct observation of ultrafast evolution of this term has not been reported. Our TR-ARPES and TR-Reflectivity meausuremets suggesting its evolution are presented in Chapter 3.

Chapter 4

Ultrafast light-spin interaction in topological insulators

Pause of light
Pulse of life
New face dawns

The imploding voice
from MACHINA/
The Machines of God (2000),
The Smashing Pumpkins

In the last decade the continuing quest to control and manipulate the spin of the electrons for a new generation of faster devices triggered the investigation of materials presenting a spin-order. In this framework, as described in chapter 1, topological insulators (TIs) represent a hot-topic because of the in-plane spin-polarized surface states (TSS) arising within the bulk insulating energy gap [3–5, 16]. The inhibition of the spin-flip events [4, 19], the control of the spin polarization using ultrashort light pulses [6, 7] together with the experimentally proved optically-triggered surface spin current [8] open new scenarios in the use of this class of materials for future opto-spintronic devices.
In order to better exploit the potentialities of TIs in spintronic applications, a deep understanding of their electronic ultrafast dynamics is required. In particular, to characterize their response upon ultrashort light pulses as a function of binding energy and crystal momentum is fundamental to disentangle the role of the TSS in the observed ultrafast phenomena. As seen in chapter 3, time- and angle-resolved photoemission spectroscopy (TR-ARPES) allows to access all these informations.

In this chapter we will present our TR-ARPES results on the $Bi_xSb_{2-x}Te_ySe_{3-y}$ (BSTS) topological insulators family. We will show a careful study of electronic dynamics as function of the stoichiometry [9]. Then, our measurements investigating the microscopic mechanism at the base of the observed optically-triggered surface spin-current in Bi_2Se_3 will be reported [10, 11]. In conclusion, we will show the first experimental proof of temporal evolution of the photoemission matrix elements by combination of TR-ARPES and TR-Reflectivity measurements [12].

4.1 Introduction

In this chapter, we will present our TR-ARPES measurements on the topological insulators family $Bi_xSb_{2-x}Te_ySe_{3-y}$ (BSTS). In particular, we have investigated the ultrafast dynamics on different stoichiometries. We have found an extremely short lifetime of TSS population for stoichiometries resulting in extremely p- and n-doped samples while an extraordinary long TSS lifetime have been retrieved for a stoichiometry leading to a vanishing binding energy of the Dirac point [9].
In order to investigate spin-order in these materials, we have performed TR-ARPES measurements with circularly-polarized ultrashort pulses. Exciting the Bi_2Se_3 sample by circularly-polarized pump pulses, we have been able for the first time to track in reciprocal space the mechanism underlying the origin of the opto-induced spin current at the surface of TIs [10, 11].
In conclusion, combined time-resolved reflectivity (TR-Reflectivity) and TR-ARPES measurements on $Bi_{1.1}Sb_{0.9}Te_2S$ topological insulators allowed us to observe for the first time the dynamical evolution of ARPES matrix elements [12].

We have measured BSTS samples grown by prof. Zhou's group at the National Lab for Supeconductivity - Chinese Academy of Science in Beijing. High quality single crystals TIs were grown by the self-flux method. Powders of bismuth, antimony, tellurium and selenium were stoichiometrically mixed, put in alumina crucibles and sealed in a quartz tube under vacuum. The materials were heated to 1000° C for 12 hours and slowly cooled down to 500° C over 100 hours before reaching room temperature [36].
Crystals of several millimeters in size were cleaved in situ at ultra-high vacuum (UHV) pressure $<5 \times 10^{-10}$ mbar for the TR-ARPES measurements. Their layered crystral structure allow natural cleave along the (111) crystallographic plane. All measurements here reported were performed with the TR-ARPES setup in our laboratory of the DEpartment of Physics of

the Politecnico di Milano. The setup is described in detail in Ref. [2]. A commercial Yb-based laser (Pharos, Light Conversion) seeds a cascade of non-linear optics stages with pulses of 300 fs duration and photon energy $h\nu = 1.2eV$ at 100 kHz. By a home-built non-collinear optical parametric amplifier (NOPA) pump pulses shorter than 30 fs at 1.85 eV are obtained. A sum-frequency generation stage (SFG) provides probe pulses at 6.02 eV with 65 fs time duration. The temporal resolution given by the convolution of pump and probe pulses is ≈70 fs. Pump and probe beams impinge almost collinearly on the sample at an angle of about 45°. The helicity of the pump and probe beam is adjusted with a broadband quarter-wave plate. By means of a motorized delay stage, the delay between pump and probe pulses is changed. Photoemitted electrons are detected by means of a time-of-flight (TOF) analyzer equipped with a micro channel plate (MCP) with energy resolution of approximatively 50 meV. The angular acceptance of the TOF analyzer is about 0.8°. The angular dispersion maps were acquired by rotating the sample's normal with respect to the analyzer axis in 2° steps. All the measurements here presented have been performed at room temperature.

Bulk-insulating high-quality single crystals $Bi_{1.1}Sb_{0.9}Te_2S$ have been grown by the vertical Bridgman technique and doped with a very small percentage of Sn by prof. Cava's group in Frick Chemistry Laboratory at Princeton University. The required amounts of elements with high purities were placed in carbon-coated, bottom-pointed quartz ampoules with an inner diameter of 4 mm. The high-purity starting materials bismuth, antimony and tellurium were further purified by heating under vacuum of $\approx 10^{-5}$ mbar at 950°C in the presence of carbon, in sealed quartz tubes. The crystal growth ampoules were sealed under a vacuum of $\approx 10^{-5}$ mbar. The crystal growth was performed at ≈ 700°C with a translation rate of ampoule of $1\frac{mm}{h}$ through the crystallization zone and 15-cm-long crystal boules were obtained. This stoichiometry is the result of a careful combination of concepts in crystal and defect chemistry, strain-mediated chemical stability, electronegativity and resonant level doping leading to a high-quality large single crystal characterized by a low-carrier concentration, an overhelming surface transport and a DP well isolated from bulk conduction and valence bands. In addition, it exibits excellent cleavage reproducibility. More details can be found in [153]. TR-ARPES measurements on the $Bi_{1.1}Sb_{0.9}Te_2S$ sample have been performed by Dr. Fabio Boschini and Marta Zonno on the Ti:sapphire laser-based setup developed by prof. Damascelli's group at the University of British Columbia. The Ti:sapphire laser (VitesseDuo and RegA 9000 by Coherent) provides 1.55 eV pulses with 180 fs pulse duration at a repetition rate of 250 kHz. This fundamental frequency is used as pump to bring the system out-of-equilibrium.

Then, the band structure is probed by 6.2 eV pulses achieved by fourth harmonic generation starting from the fundamental frequency. Pump and probe beams run almost parallel and are focused onto the sample under an angle of 45° using the same focusing lens. This results in spot sizes approximately of 250 μm and 120 μm for pump and probe beam, respectively. Both beams are vertically (s) polarized. The linear polarization of the beams is controlled by means of a broadband half-wave plate. The time delay between pump and probe is controlled by a motorized delay stage. Photoemitted electrons are collected by a SPECS Phoibos 150 emispherical analyzer, with 19 meV and $0.0003A^{-1}$ energy and angular resolution, respectively. The total temporal resolution is about 250 fs. More details can be found in [151]. Samples have been cleaved by the tape method at a base pressure of 3 x10^{-11} mbar. All measurements have been performed at room temperature.
We have performed time-resolved reflectivity measurements on $Bi_{1.1}Sb_{0.9}Te_2S$ topological insulator on the broadband ultrashort pump-probe setup developed at the Politecnico di Milano. Three NOPAs operating in different frequency ranges are driven by 150 fs pulses at a central wavelength of 780 nm provided by a 1 kHz repetition rate Ti:Sapphire amplifier (Clark-MXR model CPA-1). White light continuum generated in a sapphire plate is used as seed for all three NOPAs. The first NOPA (NOPA 1) covers a spectral range between 0.83 eV and 1.24 eV. The pulses are temporally compressed to a transform-limited pulse duration of 8.5 fs by a deformable-mirror-based pulse shaper. The second NOPA (NOPA 2) provides pulses ranging from 1.2 eV to 1.5 eV with a transform-limited pulse duration of 13 fs by a pair of fused silica prism. Both NOPA 1 and NOPA 2 are used as probe of the transient response of the sample. They are synchronized with the third NOPA (NOPA 3) that works as pump to photoexcite the sample out-of-equilibrium. NOPA 3 spans an energy range between 1.8 eV and 2.4 eV with a pulse duration of 7 fs by multiple reflections between a pair of chirped mirrors. The overall temporal resolution of the pump-probe setup below 19 fs. The time delay between pump and probe is adjusted by a motorized delay stage. Pump and probe beams are focused on the sample by a spherical mirror in a quasi-collinear geometry. More details about the generation of pump and probe beams can be found in [154]. The polarization of the pump and probe beams is adjusted by means of a broadband half-wave plate. TR-Reflectivity measurements have been performed at room temperature on in air-cleaved samples surface.

4.2 Electronic dynamics in $Bi_xSb_{2-x}Te_ySe_{3-y}$ topological insulators family

As discussed so far, topological insulators (TIs) represent a phase of matter that is extremely interesting for bringing the actual information technology, based on the electronic charge, to the future faster and less consuming spintronic technology, i.e. based on the spin of the electrons. However, some practical limitation have prevented the large diffusion of TIs in working spintronic devices. First of all, to exploit the Dirac fermions properties, it is mandatory that the surface contribution overwhelms the bulk one in transport [155]. In fact, even if the bulk has a strong insulating character, in most TIs sinthesized up to date the bulk transport is still large enough to hide the spin-polarized surface contribution. As seen in Chapter 1, the $Bi_xSb_{2-x}Te_ySe_{3-y}$ (BSTS) topological insulator represent an ideal platform for future applications. ARPES measurements have reported how varying the stoichiometry the position of the Dirac point (DP), the point in which the upper and lower branch of the topological surface state (TSS) Dirac cone cross, can be tuned with respect to the Fermi level (E_F) [28, 156, 157]. This represents a great advantage since it is possible to finely tune the desired properties keeping the bulk insulating behavior. In particular, the most promising compounds are Bi_2Te_2Se [44], $Bi_xSb_{(x-2)}Te_3$ [158], $Bi_{0.5}Sb_{1.5}Te_{1.8}Se_{1.2}$ [159] and $BiSbTeSe_2$ [160] where transport measurements have shown a strong surface signal overwhelming the bulk conduction.
In order to realize ultrafast opto-spintronic devices, the out-of-equilibrium dynamics of TSS electrons has to be deeply characterized. In particular, one wants a long lasting electronic population upon optical pump excitation in order to employ it in device applications. In this section we report a careful investigation of electronic dynamics as a function of the different stoichiometries. Our results show how varying the position of the DP with respect to the Fermi level the electronic population lifetime in TSS changes over a range of tens of picoseconds. The excited electronic population lasts for an extraordinary long time only for particular stoichiometry in which the DP has a vanishing binding energy .

Figure 4.1 shows TR-ARPES for six selected samples of the BSTS family at three different pump-probe delays: before the pump arrival (left panel), at the maximum overlap between the pump and the probe, i.e. at time-zero (central panel) and 1 ps after the excitation (right panel). Going from panels (a) to (f) in Fig. 4.1, the amount of bismuth and selenium increases at the

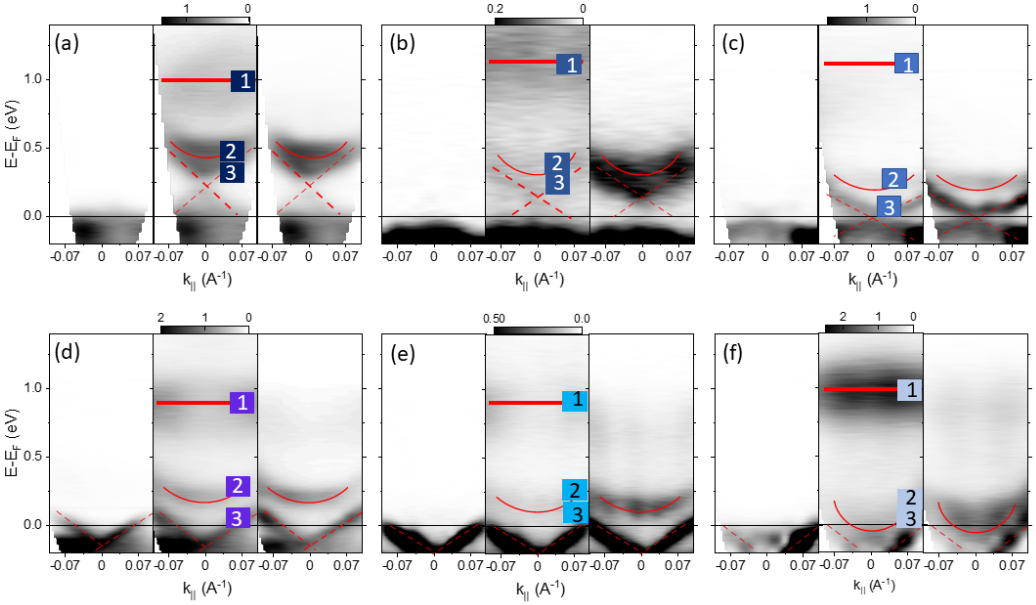

Fig. 4.1: TR-ARPES maps before the pump arrival (left panle), at time-zero (central panel) and 1 ps after the pump excitation (right panel) for six BSTS samples: (a) Sb_2Te_3, (b) $Bi_{0.5}Sb_{1.5}TeSe_2$, (c) $Bi_{0.8}Sb_{1.2}Te_3$, (d) Bi_2Te_3, (e) $Bi_2Te_{2.65}Se_{0.35}$ and (f) $Bi_2Te_{0.5}Se_{2.5}$. The Fermi level is indicated by the solid horizonatl black line. Dashed red lines are eye-guides for the TSS. Solid parabolic curves mark the CB. Solid lines indicate the high-energy BBs.

expense of antimony and tellurium. The DP binding energy varies linearly passing from positive binding energy in Sb_2Te_3 (panels (a)) to extremely negative in $Bi_2Te_{0.5}Se_{2.5}$ (group (f)) in agreement with previous steady-state ARPES measurements [28]. This implies that TSS becomes gradually more and more occupied going from (a) to (f) in Fig. 4.1. At zero pump-probe delay, electrons are promoted to states lying above the Fermi level. Looking at the central panel for each group in Fig. 4.1, three common features can be identified: flat bulk bands lying around 1 eV above the Fermi level (labeled BB, marked by a solid flat thick red line), the parabolic dispersing bulk conduction bands (CB, marked by a solid parabolic red line as guide for eyes) and the unoccupied part of the TSS (mostly for panels (a)-(d)). After 1 ps, the spectral weight induced by the pump in the BB has almost completely transferred to the CB and the unoccupied part of the TSS. This behavior is in agreement with previous TR-ARPES measurements that report the high energy lying bulk bands acting as electronic reservoir for TSS and CB [54, 57, 58].

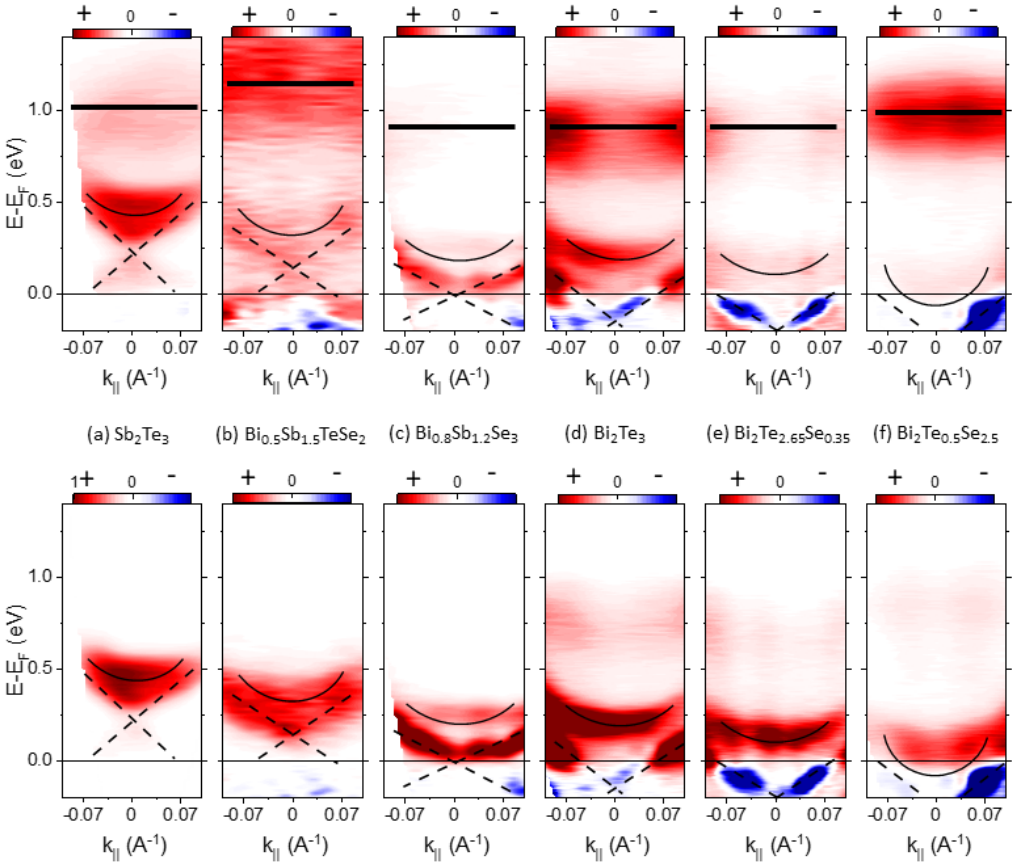

Fig. 4.2: Photo-induced electronic population (red) and depletion (blue) at time-zero (top row) and after 1 ps from the pump excitation (bottom row) of BSTS samples of Figure 4.1.

In order to highlight the photo-excitation due to the pump pulses and the evolution of the electronic population in time, we have plotted in Fig. 4.2 difference ARPES map. They are obtained subtracting the quasi-steady-state map before the pump arrival (left panel) to central, i.e. time-zero, and right, i.e. at 1 ps delay, panels of Fig. 4.1. The upper row in Fig. 4.2 reports the difference ARPES map for zero pump-probe delay; the lower row the same at 1 ps after pump excitation. Red color represents an increment of spectral weight after pump excitation while blue color is a depletion signal. The same scale is kept at zero and 1 ps delay for each compound.
Figure 4.2 highlights what we have discussed so far. At zero pump-probe delay we observe in general a stronger positive signal associated with the BB (solid thick black line). The TSS (dashed black line) and CB (solid black parabola) have at this delay a very weak spectral weight. In contrast, at 1

ps the BB has almost disappeared while a strong spectral weight appears in the CB and TSS. This indicates that there is not a direct optical coupling with of TSS and CB states. Electrons are first promoted to the high-energy lying BB. Then, these high-energy electrons decay into partially unoccupied CB and TSS.
We point out that for samples having DP at large positive binding energies (Fig. 4.2 (a) and (b)) the lower branch of the TSS shows a very weak spectral weight compared with the upper part even one picosecond after the optical excitation. This dynamical effect has already been reported in Sb_2Te_3 [62], but our data suggest that it is a more general feature. The low spectral weight of the lower part of the TSS is due to the so-called bottleneck effect. The reduced phase space at the DP in fact inhibits intra-band scattering mechanism at the DP resulting in an electronic accumulation into the upper branch of the Dirac cone.

We report the dynamics of each band (BB, CB and TSS) in Figure 4.3. Electronic dynamics are obtained integrating the photoemission intensity within the boxes reported in the upper row of Fig. 4.2 for several pump-probe delays. Boxes 1, 2 and 3 refer to BB, CB and TSS respectively. In Fig. 4.3, the electronic dynamics are reported according to the colors of the boxes in Fig. 4.2. In particular, the color scheme is the following: the color turns lighter as the DP binding energy decreases. All the curves in Fig. 4.3 have been normalized to their respective maxima for an easier comparison through different compounds.
The dynamics of the bulk bands BB is reported in Fig. 4.3 (a). We observe that, within the experimental noise, all curves are almost identical. They display a fast rising due to the pump beam followed by an exponential decay related to electronic relaxation processes. The normalized intensity profile can be fitted by a phenomenological function given by the convolution between a Gaussian function representing our instrumental response and an exponential decay function. The resulting fit is represented by the red dashed line in Fig. 4.3 (a) and it is reported in panels (b)-(d) as reference. According to our fits, upon pumping electrons are transferred to the BB and then relax towards low energy bands with a characteristic decay time $\tau_D \approx 220 fs$. This dynamics is in agreement with previously reported TR-ARPES measurements [54, 57, 58].
Remarkably, the dynamics of BB is the same for all compounds, i.e. for all binding energies of DP. Thus, the relaxation of the optically-induced electronic population in BB seems to be unaffected by the filling degree of the TSS. This observation suggests a preferential coupling between BB and CB: inter-band scattering from BB to CB is the main relaxation mechanism for

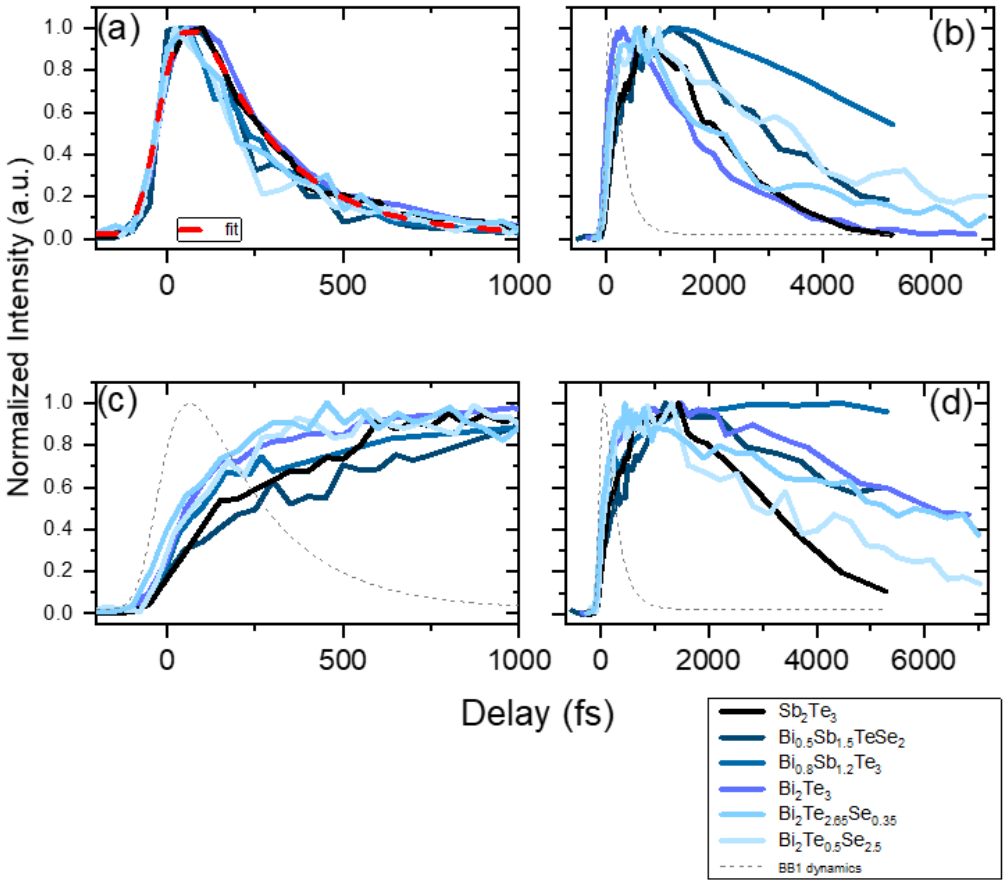

Fig. 4.3: Electronic dynamics for different bands as a function of the stoichiometry (same color code as Figure 4.1). The curves are normalized to their respective maxima. (a) BB dynamics (box 1 in Figure 4.1). The dashed red lines is a phenomenological fit reproduced in all panels as a comparison. (b) CB dynamics (box 2). (c) and (d) TSS dynamics (box 3).

the photo-induced electronic population in BB. Since CB is almost unoccupied for all the BSTS samples here investigated, it can easily accomodate the electronic population coming from BB bands. In addition, looking at the CB dynamics shown in Fig. 4.3 (b), we can notice that it is not directly populated by the optical pump (the dashed black line resulting from the fit of BB dynamics). By contrast, CB is mostly populated around 250 fs past the pump, in agreement with the decay time τ_D retrieved for the BB population decay. Panel (c) in Figure 4.3 shows the fast temporal evolution of the TSS. In contrast with the CB, we observe only a small spectral weight associated

with the BB characteristic decay time of 220 fs. These observations confirm that the BB population dynamics is not significantly affected by the TSS. Figure 4.3 (b) and (d) show the electronic dynamics associated to the CB and to the TSS, respectively, on the same time-scale. A comparison between these two dynamics suggests an interplay between CB states and TSS.
In particular, looking at the data three experimental evidences are remarkable:

i. the relaxation dynamics of CB states and TSS occurs on the picosecond time-scale, much longer with respect to the relaxation of high-energy BB;

ii. compounds in which the DP lies above the Fermi level exhibit a longer rise time among the BSTS samples;

iii. for the $Bi_{0.8}Sb_{1.2}Te_3$ sample we observe the slowest relaxation for the TSS electronic population.

To better understand these three experimental observations we have fitted TSS dynamics reported in Fig. 4.3(d) with a bi-exponential function convoluted with the instrumental response in order to include the experimentally observed delayed build-up of the photoemission signal. The resulting fit for the upper branch of the Dirac cone in the Sb_2Te_3 is reported in Fig. 4.4(a). Here, τ_R represents the characteristic rise time of the exponential growth while τ_D is the decay time constant. Figure 4.4(b) shows the resulting characteristic time constants for all the investigated samples as function of the binding energy of the DP with respect to the Fermi level, i.e. as a function of stoichiometry.

Two trends can be identified in Fig. 4.4(b). (i) As discussed so far, BSTS compounds in which the DP is at positive binding energy, i.e. with most of the Dirac cone unoccupied, exhibit a longer build-up with respect to the ones in which the TSS is almost completely occupied. The latter are perfectly matching the decay time $\tau_D \approx 220fs$ of bulk bands (BB). (ii) For $Bi_{0.8}Sb_{1.2}Te_3$, ie. for the sample characterized by the DP at the Fermi level, the dynamics is slower with respect to the other compounds investigated. In particular, the decay time is out of the delays window investigated by us.
Simple considerations based on Fermi's Golden Rule (FGR) defined as

$$w_{f,i} = \frac{2\pi}{\hbar} |\left\langle \phi_f | \hat{V} | \phi_i \right\rangle|^2 \delta(\omega), \tag{4.1}$$

i.e. the probability of electronic transitions from BB, CB or TSS to other states, can help us address our experimental observation. FGR explains the

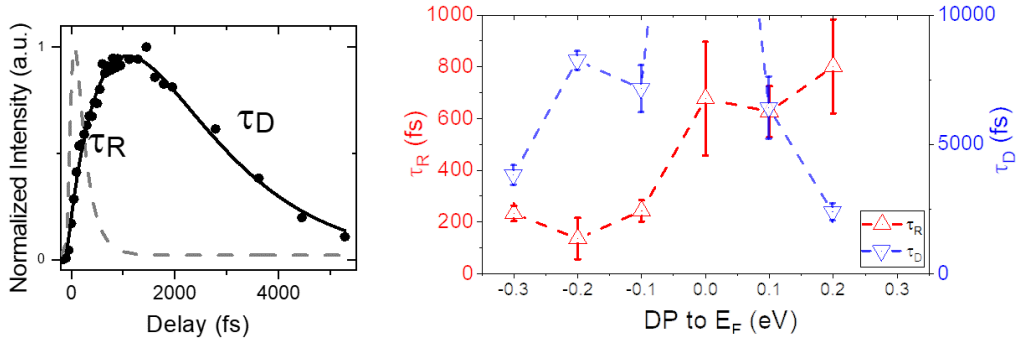

Fig. 4.4: (a) Phenomenological fit of the TSS electronic dynamics (data of Sb_2Te_3 sample): a bi-exponential function with rise time τ_R and decay time τ_D convoluted with the instrumental response function. Red dashed curve indicate the BB dynamics from Figure 4.3. (b) τ_R (red dashed curve, red up trangles) and τ_D (blue dashed curve, blue down triangles) as a function of the position of the Dirac point (DP) with respect to the Fermi level, i.e. the stoichiometry. τ_R refers to the red right axis, τ_D refers to the blue left axis.

very fast decay of BB photo-induced population: electrons promoted at high-energy have in fact a large number of unoccupied states at lower energies. Then, there are several decay-channels opened for these electrons. This implies a very fast decay time.
Also the shorter decay time for Sb_2Te_3 and $Bi_2Te_{0.5}Se_{2.5}$ can be interpreted in terms of FGR. In both these, the VB and the CB are partially unoccupied in steady-state conditions providing additional scattering channels for high-energy excited electrons. This mechanism is in agreement with the bulk diffusion process previously proposed [61]. Only for systems in which the Fermi level is lying in the bulk energy gap and bulk states do not interfere with TSS, a long persistence of electronic population can be achieved. We should mention that in condition of TSS well isolated from the bulk bands an additional effect could occur leading to an increased lifetime of the TSS population: a photo-induced surface band bending [57, 58]. Optical excitation creates in this case a different transient chemical potential for electrons and holes. The result is a Schottky barrier for electronic relaxation. Analogously, as seen in Chapter 1, a surface photovoltage has been reported leading to a microsecond lifetime of the TSS population in different topological insulator compounds [60]. However, the role of these effects in the long-lasting population of TSS is still an open-question [161]. Other mechanisms like inefficient surface-bulk phonon scattering [56] or spin-mediated channels [78] and spin-polarized bulk hybridized surface resonance [66, 77] states have been

proposed. We remark that they can be consider as the microscopic theory of our more general approach with FGR.
The extremely long-lasting TSS population observed for $Bi_{0.8}Sb_{1.2}Te_3$ (dark cyan curve in Fig. 4.3(c-d)) deserves a special deeper discussion. As we have already stated, a long persistence of the excited population in TSS is a fundamental requirement to apply TIs in working spintronic devices. In this particular case, the Fermi level is exactly in the middle of the gap and at the DP. Then valence band states are completely occupied and cannot contribute as additional decay channels if not through carrier recombination with the small transient generated holes population. As discussed so far, the absence of bulk states alone does not lead to such exceptional long lifetime. In this case also the extremely reduced phase space at the DP plays a fundamental role. In steady-state condition the VB and lower part of the TSS are completely filled while upper branches and the CB are unoccupied. Upon pump excitation, electrons are promoted to high-energy BB as previously described. Then, they fastly decay mostly into bulk CB. Bulk diffusion is hampered, then electrons fill the unoccupied part of TSS. Intra-band scattering events reduce the energy of Dirac fermions. However, when they approach the Fermi level the vanishingly small available density of states at the DP leads to an accumulation of fermions. Then the electronic population has an extraordinaly long lifetime due to the very small number of decay-channels with a strongly enhanced bottleneck effect.

In conclusion, we have investigated electronic dynamics for different BSTS stoichiometries characterized by different energies of the DP with respect to the Fermi level. This strongly affects the electronic relaxation dynamics of the Dirac fermions in TSS. We have explained our observation in terms of Fermi's golden rule and bottleneck-effect due to the reduced phase space at DP. In particular, for an intrinsic TI, we have observed a terrific long persistence of the electronic population in TSS. Our results provide a careful investigation of the out-of-equilibrium properties of TIs necessary for their sucessful implementation in spintronic devices. In particular, the reported long lifetime for intrinsic TIs represents an ideal platform for future application.

4.3 Microscopic origin of surface spin-current in Bi_2Se_3

The spin-momentum locked texture of TSS imposes to counter-propagating electrons to have opposite spin[162]. Then, a surface current leads to a spin current in TIs. For these reasons in the last decade TIs became a hot topic in materials science representing a promising platform for the realization of these devices.
The capability of circularly polarized light to generate a net surface spin current in TIs has been demonstrated by several groups [8, 67–72]. In analogy with the optical orientation in semiconductors [163], circularly polarized photons can trigger electronic transitions in a spin-selective way. As seen so far, the spin-texture of the TSS is momentum-dependent. Then, an asymmetric population in the reciprocal space might be excited by circular photons. As a consequence, a spin current occurs in the surface states [73, 74]. However, this mechanism has not been yet experimentally observed. Optical and transport experiments can in fact provide only information in which bulk and surface states are entangled while ARPES, able to disentangle bulk and surface contributions in **k**-space, can only access steady-state conditions. We want in any case to remark that spin-resolved ARPES measurements highlighted the possibility to optically manipulate the spin of photoelectrons as function of the polarization of impinging light [6, 7]. This confirms once again the fundamental role played by polarized photons in TIs phenomenology.
As experimentally shown by us in the previous sections, and in agreement with several independent TR-ARPES measurements, in TIs the unoccupied states of the TSS do not directly couple with the near-IR pump photons commonly exploited in TR-ARPES setups [9, 54, 57, 58]. In other words, it is not possible to directly excite a population in the TSS using optical-near IR beams. In contrast, the TSS is populated by the inter-band electronic decay of bulk conduction bands electronic population. Recently, TR-ARPES measurements investigating the photoinduced-depletion of the TSS or exploiting mid-IR pump photons to directly access TSS empty states of Sb_2Te_3 topological insulators have reported an asymmetric electronic population in crystal momentum space generating a photocurrent [75, 76]. However, the role of the spin in this process is not fully addressed to date.
In the following, we will show our TR-ARPES measurements exploiting circularly-polarized pump pulses to study the ultrafast mechanism at the origin of the surface spin-current in Bi_2Se_3 [10, 11]. The prototypical topological insulator Bi_2Se_3 in fact owns an empty topological surface state (ESS) within a bulk energy gap located about 1.8 eV above the Fermi level as ex-

perimentally established by 2PPE measurements [63, 64]. Thus, the 1.85 eV pump photons provided by our TR-ARPES setup might directly fill the ESS. In addition, other TR-ARPES measurements exploiting circularly-polarized pump pulses have reported a spin-selective population of the empty states [164–167].
Our observation of an asymmetric population of the ESS upon circularly-polarized excitation and a subsequent ultrafast momentum-dependent intra-band relaxation within 10-100 femtoseconds represent the first momentum-resolved proof of the optically induced spin current at the surface of topological insulators.

We investigated high quality single crystals of Bi_2Se_3 grown by self-flux method as described in the introduction to this chapter. Unfortunately, on these samples it has been not possible to have clear LEED patterns and therefore identify high-symmetry cristalline directions. However, the TSS and the bulk band structure have isotropic character within a region of $|\mathbf{k}_{||}| \approx 0.1\mathring{A}^{-1}$ around the Γ-point comparable to the one experimentally accessible in our measurements. Thus, the in-plane orientation of the sample is not relevant for our purpose.

Thanks to the selenium-vacancies, Bi_2Se_3 is intrinsically n-doped. This means that the Fermi level (E_F) crosses the bulk conduction band and the TSS is completely occupied in equilibrium conditions. The 6 eV-probe energy ARPES map of Bi_2Se_3 is reported in Figure 4.5(a), similar to the ones reported by other 6-eV TR-ARPES measurements (e.g. see supplementary materials of [77]). It is possible to retrieve in Fig. 4.5(a) a Dirac-cone like dispersion associated with the occupied TSS (blue and red solid lines are added to Fig. 4.5(a) as a guide for the eyes). The binding energy of the DP is about -0.25 eV. In addition, photoemission intensity associated with the occupied part of the bulk conduction band (CB) is clearly visible and marked with a light blue parabolic solid line. The TSS merges with the gapped bulk bands. In particular, for Bi_2Se_3 the Dirac point (DP) is well centred within the bulk energy gap and the TSS is superimposed to the valence band (VB) for lower energies and with the bulk CB for higher energies. In spite of this, ARPES measurements allow us to get the group velocity of TSS. In fact, the Dirac point and the linear branch around the Dirac point are free from any superposition since they are within the bulk band gap. Following the linear dispersion superimposed in Fig. 4.5(a) we estimate a group velocity of $5.7 \pm 0.3 \cdot 10^5 \frac{m}{s}$, in agreement with the previously reported value of $5.4 \cdot 10^5 \frac{m}{s}$ [63].

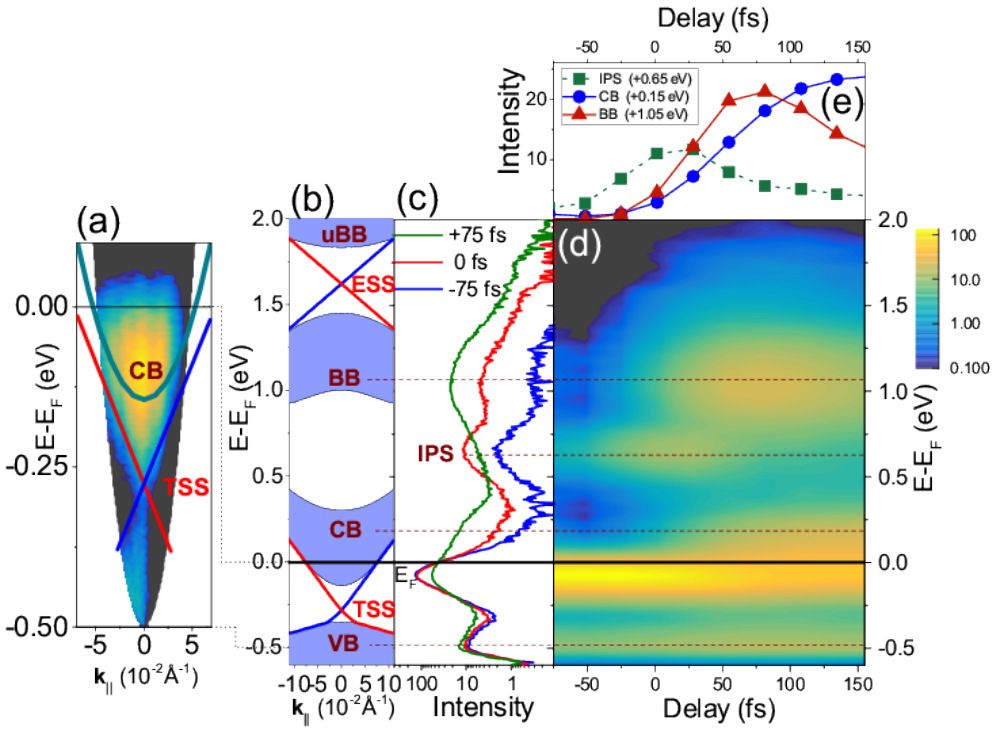

Fig. 4.5: (a) ARPES map of the first occupied topological surface state (TSS). Colored lines are eye-guides to follow the dispersion of the TSS and of the bulk conduction band (CB). (b) Cartoon of the band structure (deduced from our experimental data) of Bi_2Se_3; VB: valence band, CB: conduction band, BB: bulk band, uBB: upper bulk band, TSS: topological surface state, ESS: empty topological surface state. At 1° angle of emission (c) energy distribution curves (EDCs) for three different pump-probe delays and intensity chart binding energy versus pump-probe delay. (e) Dynamics of the main spectral features: CB, IPS and BB. The zero pump-probe delay has been determined with respect the maximum intensity of the IPS peak. From [10]

In Figure 4.5(b) we report schematically the band structure of Bi_2Se_3 derived from our measurements and from [63]. In particular, two unoccupied bulk bands (labeled as BB and upper BB (uBB)) lie in the energy window ranging from +1 eV to +2 eV. Within the local bulk energy gap between BB and uBB, the presence of a second completely empty topological surface state (ESS) has been experimentally shown [63, 64]. In particular, the DP of ESS has been found at ≈ 1.8 eV above the Dirac point of the first filled TSS.
The electronic dynamics is highlighted in Figure 4.5(c-e). Figure 4.5(c) reports energy distribution curves (EDCs) for three pump-probe delays mea-

sured under an emission angle of 1°, i.e. very close to the $\bar{\Gamma}$-point. We observe that the main effect of the pump beam is to promote electrons into empty bulk bands up to +1.85 eV above the Fermi level, as discussed in previous sections. In particular, the empty BB represented by the broad peak at +1 eV is the mainly populated feature at the maximum overlap between pump and probe beams (i.e. at zero delay). Within few hundreds of femtoseconds (see the electronic temporal dynamics reported in Fig. 4.5(e)), BB electrons relax into the lower bulk CB (between 0 and +0.4 eV). In Figure 4.5(d) we report the binding energy vs. pump-probe delay normalized intensity map that helps highlight the dynamics of electrons in Bi_2Se_3. The decay of the photo-filled BB at 1 eV within the 500-fs temporal window is clearly observable. A feature around 1.6 eV indicates the uBB. The population of the CB changes on a longer time-scale, indicating a relaxation-assisted population process as already described in previous sections. Within the emission angle range explored by our measurements (±5°), the TSS lies entirely below E_F within the energy gap of VB and CB. Based on EDCs reported in Fig 4.5(c), the ESS is located at a binding energy $\approx$ +1.6eV at the edge of the higher energy tail of the BB.
Around +0.7 eV we retrieve a peak present also at negative delays. This peak in addition exhibits a reverse dynamics, i.e. a dynamics towards negative delays (see dashed line in Fig. 4.5(e)) suggesting that this feature is optically pumped by the 6.05 eV-probe and photoemitted by the 1.85 eV-pump beam. This clearly indicate that this +0.7 eV peak represents an image potential state (IPS) [55, 168, 169], already reported by TR-ARPES measurements on p-doped Bi_2Se_3 [54]. Although the IPS presence does not add any information about the electronic dynamics of the TSS and ESS, it testifies a good surface quality and morphology. In addition, it is an excellent way to determinate the zero pump-probe delay that corresponds to the maximum intensity associated with the IPS peak.

In the following, we will focus on the ESS electronic dynamics. Our TR-ARPES measurements on the ESS dynamics have been performed with a pump fluence of $\approx 500 \frac{\mu J}{cm^2}$, high enough to populate the empty surface state, but below the multi-photon absorpion thershold. Figure 4.6(a) reports an ARPES binding energy vs. crystal momentum map measured with p-polarized pump and probe beams. We focus on the binding energy ranging from 1.25 eV to 1.85 eV where the ESS lies. A Dirac-cone like linear dispersion represented by the red dashed lines in Fig. 4.6(a) can be observed. Following this linear feature, we derived a value of $3.6 \pm 0.3 \cdot 10^5 \frac{m}{s}$ of the group velocity, comparable with the values found in literature ($3.3 \cdot 10^5 \frac{m}{s}$).

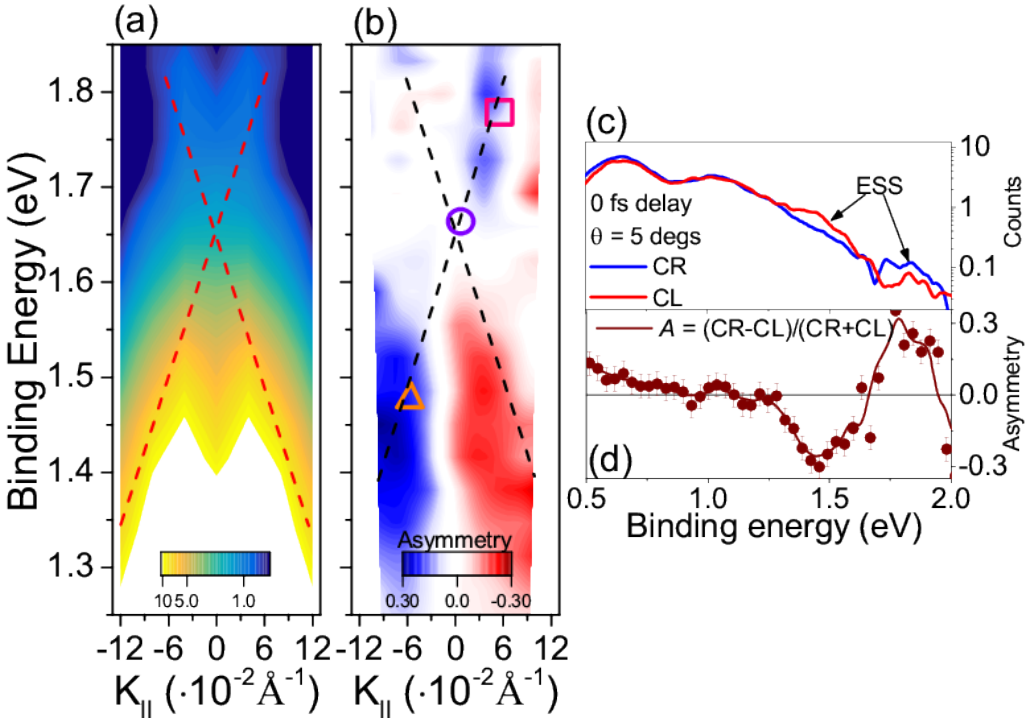

Fig. 4.6: At time zero (a) symmetrized ARPES map for linearly p-polarized pump and probe beams and (b) ARPES map of the asymmetry signal due to the circularly polarized pump beam. Red and black dashed lines in panels (a,b) follow the TSS dispersion. (c) EDCs at 5° emission-angle and time-zero for two opposite pump helicities (circular rightCR and circular leftCL). (d) Asymmetry induced by the circularly-polarized pump showing the two branches of the ESS. From [10].

This is a fundamental experimental observation that allows us to state that we are really observing the ESS and not a replica of the first occupied TSS into the unoccupied bulk continuum bands due to the pump-induced optical transition.

The capability to directly photo-excite an electronic population into the ESS allows us to investigate its spin-polarization using circularly polarized pump photons. We mention that other groups have recently reported the generation of spin-selective optical transitions as main effect of circularly-polarized pump beam in TR-ARPES, in analogy with the well-established optical orientation in semiconductors [163]. Therefore, considering the difference between photoemission spectra photoexcited by photons with opposite helicities we can reveal the polarization of the ESS. As described in Sec. 1.3, the asymmetry

signal highlights the underlying polarization. The resulting asymmetry map at zero fs pump-probe delay is reported in Figure 4.6(b). Following the linear dispersion retrieved from ARPES data acquired with linearly polarized pump and probe (black dashed line), we can clearly observe two opposite polarizations for the two linear branches of the ESS. In particular, the polarization signal perfectly agrees with the circularly-polarized 2PPE measurements by Niesner et al [64]. The upper part of the Dirac cone exhibits an asymmetry around 20% at positive $\mathbf{k}_{||}$ while it is almost zero in the opposite $\mathbf{k}_{||}$ region. In contrast, the asymmetries for negative and positive $\mathbf{k}_{||}$ are very similar (30% for negative $\mathbf{k}_{||}$ and 25% for positive $\mathbf{k}_{||}$). We ascribe the difference in the asymmetry of the upper part of the cone to matrix element effects that can lead to a total suppression of one branch of the TSS [32, 170]. We want to remark that a photo-induced asymmetric population has been observed in the almost empty TSS of Sb_2Te_3 using mid-IR pump TR-ARPES; this **k**-space asymmetry has been considered as the evidence of a photo-induced current [75, 76].
To better clarify the role of the circularly-polarized pump, in Figure 4.6(c) we report the EDCs at 5° emission angle and at zero fs pump-probe delay in the 0.5-2.0 eV binding energy range for the two opposite helicities of the pump: circular right (CR, in blue) and circular left (CL, in red). We notice that the BB in the energy region around 1 eV does not show any difference for the two helicities as expected for an unpolarized bulk band. In contrast, in the binding energy region where we have observed the ESS, two polarization-dependent features appear at different energies. Figure 4.6(d) shows the asymmetry computed for the EDCs in panel (c) and the asymmetry reverses sign at 1.6 eV, i.e. the ESS Dirac point binding energy. We can consider the two shoulders depending on pump helicities as the electronic population into the ESS, i.e. spin-polarized Dirac fermions optically photo-excited by the circularly polarized pump. This observation once again suggests that circularly-polarized visible photons promote electronic transitions in a spin-selective way.

To study the dynamics of the ESS Dirac fermions we have considered the difference $D = I_{CR} - I_{CL}$ instead of the asymmetry parameter A defined in Eq. refdichroism. The latter diverges at negative delays when dealing with unoccupied states. The difference D dynamics are reported as black squares in Figure 4.7(a) for three different momenta (+0.06 $\mathring{A}^{-1}$, +0.01 $\mathring{A}^{-1}$ and -0.05 $\mathring{A}^{-1}$) along the most intense branch of the ESS (see symbols in Fig. 4.7(b)). As a comparison, the transient population of the BB is also reported (red circles).

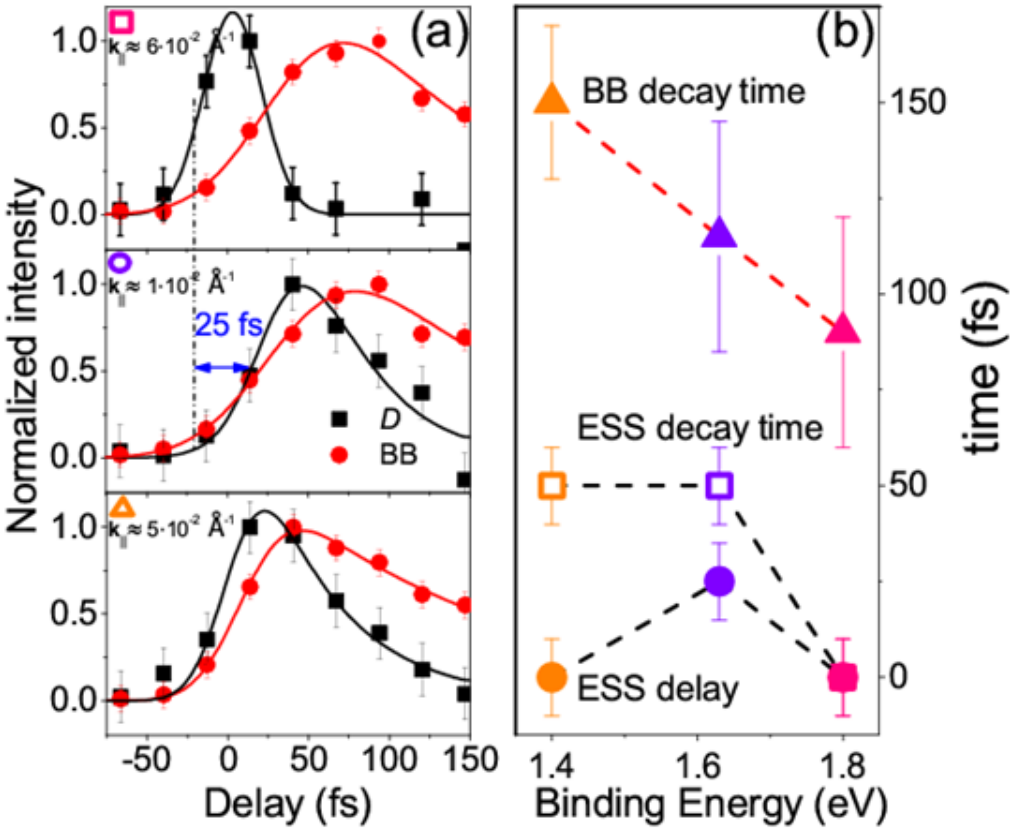

Fig. 4.7: (a) Difference signal D (black squares) and spectral intensity of the BB (red circles) as a function of the pump-probe delay for the most intense branch of the ESS at three different crystal momenta $\mathbf{k}_{||}$: 0.06 $\mathring{A}^{-1}$ (top), 0.01 $\mathring{A}^{-1}$ (middle) and 0.05 $\mathring{A}^{-1}$ (bottom) (see corresponding symbols in the ARPES map of figure 4.6(b)). Solid lines are fits. Panel (b) shows the extrapolated time constants and delays. From [10].

Looking at the dynamics of the difference in Fig. 4.7(a), we notice that for crystal momenta away from the $\bar{\Gamma}$-point, i.e. away from the Dirac point of the ESS, the difference signal arises within our temporal resolution. Close to the $\bar{\Gamma}$-point instead it shows a 25±10 fs delayed-response. In addition, at +0.01 $\mathring{A}^{-1}$ the difference signal shows also a build-up as determinated by a phenomenological fitting (solid line in Fig. 4.7(a)) using an exponential growth and decay convoluted with the instrumental resolution Gaussian function. The difference signal shows a pulsewidth-limited decay at +0.06 $\mathring{A}^{-1}$. Elsewhere D has a decay characterized by a time costant of $\tau_D = 50\pm10$

fs. We stress that also the BB population exhibits an energy and momentum dependence: going from 0.06 $\mathring{A}^{-1}$ to -0.05 $\mathring{A}^{-1}$, i.e. binding energy from 1.8 eV to 1.4 eV, the decay costant passes from 90 ± 30 fs to 150 ± 20 fs. The results of the fits are summarized in Fig. 4.7(b); here triangles represents BB decay time constants while circles and open squares stay for ESS difference τ_R and τ_D, respectively. Colors of the points in Fig. 4.7(b) correspond to crystal momenta marked with the same colors in Fig. 4.6(b). As discussed in details in Sec. 4.2, the decreasing of the decay constant, i.e. a faster relaxation process, for higher binding energies is not surprising and it can be understood in terms of Fermi's golden rule. In contrast, the dynamics of the difference signal related to the ESS is less trivial and more intriguing. In the following, we will focus only on the most intense ESS branch signal but the discussion can be applied also to the other branch reversing pump helicities and signs.

The difference signal reported in Fig. 4.7(a) shows a faster, pump-triggered response away from the DP of the ESS while the signal appears delayed and with a slow build-up close to the $\bar{\Gamma}$-point. As previously discussed, the two topological surface states of Bi_2Se_3, i.e. TSS and ESS, have different group velocities. Due to the this difference and looking at the band structure of Fig. 4.7(b) the only optical transitions matching our pump photon energy are those connecting the valence and conduction bands to the second surface state for outer photo-emission angles, i.e. at momenta away from the $\bar{\Gamma}$ point. The TSS to ESS transition would be resonant just around the $\bar{\Gamma}$ point. The two DPs in fact have been found to be separated by 1.8 eV in binding energy. Close to the Dirac point the finite energy resolution of the pump pulse and the finite angular resolution of the experiment would naturally smear out any dichroic signal even if it originates from direct transitions from the TSS. Despite the experimental smearing, we observe a delayed dichroic signal in the region around the $\bar{\Gamma}$ point. This implies that this region is not directly populated. Besides, the density of states of both TSS and ESS is negligible close to the respective DPs. Therefore, an optical transition between them would be unlikely. Since we can rule out any possible replica of the TSS as already discussed, the delayed signal should be related only to decay processes involving the ESS. The fast response time observed at larger $|\mathbf{k}_{||}|$ then suggests a dominant bulk-to-ESS transition. Even if we cannot rule out a possible contribution from the TSS-to-ESS transition also at these $\mathbf{k}_{||}$-points, we can confidently state that it should be smaller than the bulk-to-ESS one. As seen for the electronic dynamics of the BSTS topological insulator family, the delayed build-up of the signal associated to the ESS close to $\bar{\Gamma}$-point suggests a flow of polarized electrons along the branch of the Dirac cone. In other words, this signal is due to the electrons promoted

in this binding energy-momentum region by intraband scattering mechanism such as electron-electron, electron-phonon events or scattering with defects. Due to the very short timescale experimentally observed, electron-electron scattering seems to be the dominant mechanism at the base of the electronic flow. Even the recombination of electrons into bulk bands, i.e. interband scattering, is present playing a role in the observed very fast decay of the asymmetry signal. We want to stress that only electron-electron intraband flow along the Dirac cone branch can explain the delayed build up observed at the DP in tens of femtoseconds.
The observed dynamics suggests the following mechanism: polarized-electrons are photo-excited into one branch of the ESS only for a given helicity. Then, they flow along the branch of the Dirac cone to lower energy states. Eventually, they recombine into bulk states. This phenomenological interpretation is able to explain the experimental observations in Fig. 4.7. In particular,

1) the delayed occurrence of the difference signal close to the DP of the ESS (central panel of Fig. 4.7(a));

2) the larger decay time constants for the difference signal for crystal momenta $\mathbf{k}_{||} \leq 0$ (central and bottom panels of Fig. 4.7(a)).

In addition, this phenomenological model agrees with recently proposed theoretical predictions about the circularly-polarized light triggered spin current in Bi_2Se_3 [74]. In this theoretical framework, a spin-dependent optical transition of the electron is at the base of the spin-current. A given spin-polarized electron couples selectively with a given circularly-polarized photon making a transition into unoccupied states. Due to the momentum-locked spin texture of Dirac cone, this spin-dependent transition leads to an asymmetric electronic population in the reciprocal space. Then, a total current occurs. Three terms are describing the total current:

(i) the absorption of a photon due to the photo-excitation into empty states,

(ii) the resulting intraband mechanisms of the electrons,

(iii) the interband recombination decays.

The first term is the dominant one. Until a scattering event occurs, this term grows linearly. The other two terms are describing the scattering events with electrons, defects or phonons.
We can retrieve these three points also in our phenomenological model. The observed photo-induced population into the ESS in a spin-selective way

(point (i)) is the most important term indicating the number of possible carriers for the spin-current. Then, Dirac fermions flow in **k**-space along the linear-dispersing branch due to electron-electron scattering events (point (ii)). This originates a macroscopic spin current. The finite short-lifetime of the polarized signal is due to the interband decay of electrons into unpolarized bulk bands (point (iii)).

In conclusion, our experimental results clearly prove for the first time the capability to optically induce a population in the empty topological surface state of Bi_2Se_3. In particular, exploiting circularly-polarized pump photon it is possible to induce a spin-polarized fermion population. The decay of this population in tens of femtoseconds allows these electrons to flow along the linear branch of the Dirac cone leading to a photo-triggered spin-current. An empty topological surface state has been reported also in p-type topological insulators Bi_2Te_3 and Bi_2Te_2Se [65], in which the surface transport overwhelms the bulk contribution [44]. In fact, recently TR-ARPES measurements have shown the capability to optically access the ESS of the Bi_2Te_2Se topological insulator [171]. Then, these compounds are ideal candidate for spintronic devices. We believe that our results demonstrate the capability to trigger a spin-current even in these p-type compounds by tuning the energy of the pump excitations in order to directly couple with the empty surface states. These results are fundamental for the realization of future operative opto-spintronic devices.

4.4 Transient matrix-element effect in time-resolved photoemission signal of topological insulator $Bi_{1.1}Sb_{0.9}Te_2S$

In order to better clarify the following discussion, we recall here the expression for the photocurrent at any momentum $\mathbf{k}$ and for any binding energy E_B. The photoemission intensity can be expressed as:

$$I(\mathbf{k}, E_B) \propto |M^{\mathbf{k}}_{f,i}|^2 f(E_B, T) A(\mathbf{k}, E_B), \tag{4.2}$$

where $M^{\mathbf{k}}_{f,i}$ is the initial-final state electromagnetic dipole matrix element, $f(E_B, T)$ is an electronic distribution function and $A(\mathbf{k}, E_B)$ is the one-electron removal spectral function related to bare elctronic band dispersion and many-body interactions.
Once a quasi-equilibrium condition is restored after thermalization, generally within hundreds of femtoseconds, we can consider the temporal evolution of eq. 4.2 as a good approximation of the transient photocurrent. Within this framework, we have the temporal evolution of the electronic distribution $f = f_{FD}(E_B, \mathbf{k}, T^*_{el}(\tau))$ describing the relaxation processes of the quasiparticles and the transient dynamics of the one-electron removal spectral function $A = A_{\mathbf{k}}(E_B, \tau)$.
Also the matrix element $M = M^{\mathbf{k}}_{f,i}(\tau)$ can in principle evolve upon pump photo-excitation trough modification of the initial and final state wavefunctions. However, to our knowledge, the ultrafast modification of this term has not been experimentally observed up to day.
In the following, we will show our TR-ARPES and TR-Reflectivity measurements on the $Bi_{1.1}Sb_{0.9}Te_2S$ topological insulator suggesting for the first time a non-trivial temporal evolution of the initial-final state electromagnetic dipole matrix element. TR-ARPES measurements have been performed bringing the system out-of-equilibrium with 1.55 eV pump pulses. The photoelectrons have been emitted with a 6.2 eV probe beam and collected by means of a hemispherical analyzer. In addition, high-temporal resolution broadband TR-Reflectivity measurements have been performed confirming the presence of optically triggered coherent A_{1g} optical and acoustic phonons (for more details about these setups see introduction to this Chapter). The matrix-element contribution has been disentangled by means of a careful probe-polarization analysis.

We chose a topological insulator for our investigation for the well reported photo-induced band structure modification via phonons [172]. This, in addition with the non trivial interference of the layered orbital texture in the

photoemission signal [32], makes this system the ideal platform for studying transient effects in the matrix element. We have preferred the recently synthetized $Bi_{1.1}Sb_{0.9}Te_2S$ [153] to other prototypical topological insulators such as BSTS family compounds for the following reasons:

(i) the higher chemical stability of the surface that ensures a long lifetime of the sample upon ultrashort pulse pumping;

(ii) a large bulk energy gap;

(iii) the presence of a large energy momentum range in which the TSS is isolated from bulk bands avoiding any possible TSS-to-bulk hybridization contributions.

The crystal structure of $Bi_{1.1}Sb_{0.9}Te_2S$ topological insulator is reported in Figure 4.8(a). Alternating layers of Te-Bi/Sb-S-Bi/Sb-Te form the fundamental brick of any topological insulator: the quintuple layers structure which repeats along the lattice c-direction. It is still an open question if the Bi/Sb layers are an ordered pattern of the two species or if they form a solid solution [153].

Steady-state ARPES maps of the TSS along $\overline{\Gamma M}$ direction (see surface projected Brillouin zone in Fig. 4.8(c)) acquired for vertical (s) and horizontal (p) incident polarizations 6.2 eV probe beam are reported in Figure 4.8(b). The position of the DP is found $\approx$ 120 meV below the Fermi level (E_F). Comparing the two ARPES maps in Fig. 4.8(b) a probe-polarization dependent modulation of the photoemission intensity is evident. This can be ascribed to matrix-element effects as already reported in literature [32, 170]. In particular, a total suppression of one-branch of the Dirac cone spectral weight occurs probing TSS with p-polarized light. As discussed in Chapter 1, this $\mathbf{k}_{||}$-asymmetry apparently violates Kramers' degeneracy, i.e. the time-reversal symmetry that protects the existence of the TSS. However, the suppression of spectral weight of one branch is due to matrix element effects strongly-enhanced by the interference inside the quintuple-layer structure [32]. The non-trivial layer-dependent spin-orbital entanglement of the TSS introduces a k_z dependence in the ARPES matrix element. Surface states electrons photoemitted from different layers interfere leading to the observed TSS asymmetry. We want to remark that even if this effect is well-know in steady-state ARPES of topological insulators, it was never observed in pump-probe based TR-ARPES. The TSS iso-energy contour at 100 meV above the Fermi level and at 600 fs after optical excitation is shown in Fig. 4.8(d) for

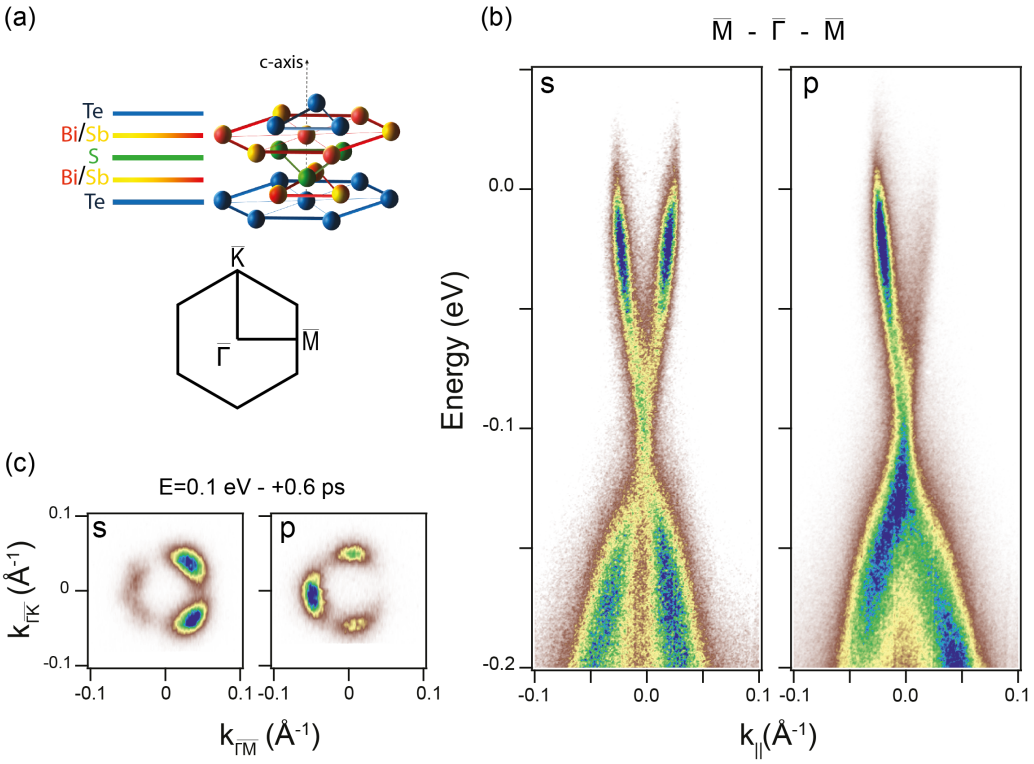

Fig. 4.8: (a) Layered-crystal structure of $Bi_{1.1}Sb_{0.9}Te_2S$ topological insulator. (b) Surface projected Brillouin zone; two high-symmetry directions are highlighted. (c) Steady-state 6.2 eV ARPES maps along $\overline{\Gamma M}$ acquired with vertically (s) and horizontally (p) polarized light, respectively. (d) Costant energy cuts at 100 meV above the Fermi level and after 600 fs from the pump excitation acquired with the two linear polarizations of the probe. From [12].

both linear polarizations of the probe beam. A polarization-dependent trigonal intensity pattern is clearly observable. This three-fold rotation symmetry suggests the presence of an hexagonal warping, as discussed in Chapter 1.

To highlight the effect of the photo-excitation due to the pump pulses, in Figure 4.9(a) we report the differential ARPES map in the TSS binding energy region, along the $\overline{\Gamma M}$ high-symmetry direction at 300 fs and 3 ps pump-probe delays measured with linearly-vertically polarized (s) probe beam. The differential map is obtained subtracting the ARPES map obtained before the pump arrival from the photo-excited ARPES map at a given delay. The color scale is the following: blue indicates a negative signal, i.e. an electronic photo-induced depletion, while red represents an increment of spectral

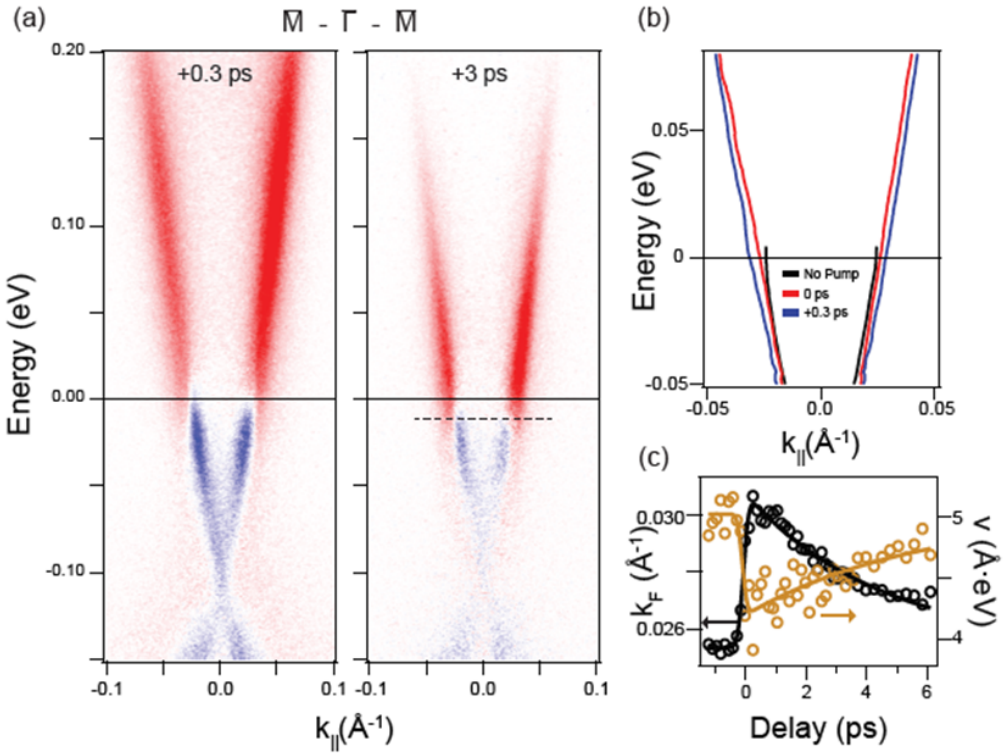

Fig. 4.9: (a) Differential pumped-unpumped maps of the TSS at 300 fs and 3 ps pump-probe delay, along $\overline{\Gamma M}$, probed with s-polarized light. The red color indicates a population while the blue stays for a depletion of the electronic states. The dashed black line in right panel indicates the shifting of the chemical potential. (b) TSS dispersion extracted by a double-Lorentzian fit of the MDCs for three different pump-probe delays: black curve - no pump, red curve at time-zero and blue curve after 300 fs from the pump arrival. (c) Temporal evolution of the extracted Fermi velocity (gold, right axis) and size in momentum of the TSS at the Fermi level (black, left axis). From [12].

weight, compatible in this case with a pump-promoted filling of the empty states of the TSS. The pump fluence is about $40\frac{\mu J}{cm^2}$.
Difference maps in Fig. 4.9(a) seem to suggest a deviation from the linear dispersion of the occupied TSS. This is better clarified in Figure 4.9(b) in which the TSS dispersion extracted by a double-Lorentzian fit of the momentum-distribution curves (MDCs) is reported for three different pump-probe delays: before the pump arrival (black curve), at the maximum pump-probe overlap, i.e. 0 fs (red curve) and after 300 fs (blue curve). A clear photo-induced modification of the TSS dispersion is observable. In particular, as reported

in Figure 4.9(c), we retrieve a transient change of both Fermi velocity and Fermi momentum, i.e. Fermi surface area. Similar modifications have been reported by Sobota et al. [172] as consequence of photo-induced lattice distortion by photo-triggered coherent bosons, even if they used a considerably higher pump fluence than the one in our measurements. We observe at 3 ps a shift of the chemical potential at negative energy with respect to the steady-state Fermi level E_F as reported by the black dashed line in Fig. 4.9(a). A similar effect has been reported in previous TR-ARPES measurements as a surface photo-voltage or transient Schottky barrier [57, 58, 60].

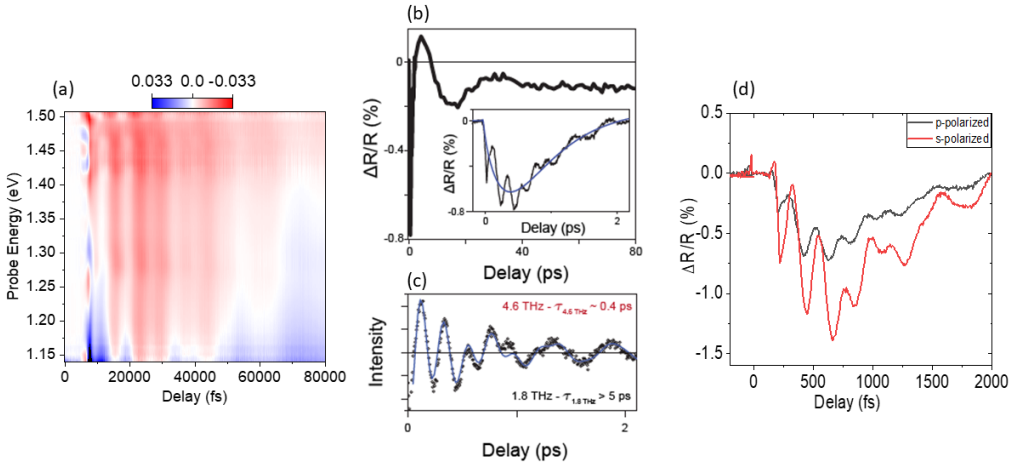

Fig. 4.10: (a) Differential reflectivity $\Delta(R)/R$ intensity map as a function of broadband probe energies and pump-probe delays. (b) Differential reflectivity $\Delta(R)/R$ trace for pump 2.25 eV and probe 1.37 eV. The inset highlights the fast dynamics within the first 2 ps. The blue curve represents a phenomenological fit with a bi-exponential function. (c) $\Delta(R)/R$ curve subtracted by the bi-exponential fitting function shown in (b). The blue curve is a double damped-sinusoidal function fit. (d) Comparison between differential reflectivity $\Delta(R)/R$ traces for two linear polarizations of the 1.37 eV probe beam.

To identify the bosonic modes triggered out-of-equilibrium, we performed sub 10 fs- broadband TR-Reflectivity. Optical measurements have been performed at room temperature on a cleaved surface. We exploited the maximum achievable fluence in order to clearly identify the triggered bosonic modes. The maximum fluence configuration corresponds to pumping the system with 2.25 eV visible pulses; the incident fluence is about 3 $\frac{mJ}{cm^2}$. The

pump-induced variation in reflectivity has been probed by broadband infrared pulses. Over the whole energy-range of the probe, the response of the system has been found to be identical (see Fig. 4.10(a)). A selected transient reflectivity $\frac{\Delta R}{R}(\tau)$ trace at 1.37 eV is shown in Figure 4.10(b). Two optical phonons can be seen in the first 2 ps. A following acoustic phonon is evident on the long-time scale. This latter has a frequency of 34 GHz (0.14 meV) with a damping time of almost 15 ps. On the short time-scale, within the first 2 ps, the $\frac{\Delta R}{R}(\tau)$ trace can be fitted by a bi-exponential function taking in account the initial rising and then the exponential decay (see the inset of Fig. 4.10(b), the blue curve represents the bi-exponential fit). We find an initial rise time of $\tau_R = 330 \pm 50$ fs and a $\tau_D = 650 \pm 100$ fs subsequent relaxation time. The recovery time observed in Fig. 4.10(b) exceeds the 80 ps investigated temporal range. This time resembles heat dissipation of the system an it is suggesting a long-lasting pump-triggered lattice distortion at which the band structure modifications are associated. Subtracting the overall transient dynamics within 2 ps from the $\frac{\Delta R}{R}(\tau)$ trace in Fig. 4.10(b) we can highlight the phononic coherent oscillations modulating the transient reflectivity response (Fig. 4.10(c)). These oscillation are nicely fitted by a double-damped sinusoidal function allowing us to extract the frequency of the photoinduced fast coherent mode: 4.60 THz (19.0 meV) and 1.79 THz (7.4 meV) with 400 fs and > 5 ps damping time, respectively. The first one is in agreement with the A^2_{1g} mode while the latter can be associated with the commonly reported A^1_{1g} optical phonon [69, 172].
The observed TSS dispersion modification takes place within our temporal resolution of 250 fs, comparable with the period of the fastest optical phonon A^2_{1g} retrieved in transient reflectivity measurements. However, the A^2_{1g} mode decays within 1 picosecond while the TSS modified dispersion endures for longer times. We notice that the A^1_{1g} instead lasts for several picoseconds. In addition, the acoustic phonon has been found to last for ≈ 15 ps. Thus, we confidently state that the TSS dispersion modulation is due to a non-trivial interplay among the photoexcited coherent phononic modes.
We stress that the complex interplay among the layers of the quintuple-layers strongly affects the photoemission signal [32]. Here, the observed modification in the dispersion of the TSS can be related to the deformation potential inside the quintuple-layers, i.e. the structure at the origin of the TSS dispersion. The observed modification of the Dirac cone dispersion upon transient deformation potential, ie. photo-triggered phonons, might then affect the photoemission intensity influencing also the retrieved transient dynamics in TR-ARPES. In the following we move our attention to the temporal evolution of the photoemission intensity in well-defined energy-momentum regions upon the two different linear polarizations of the probe. As we will show, this

allows us to disentangle the transient evolution of the photoemission matrix elements.

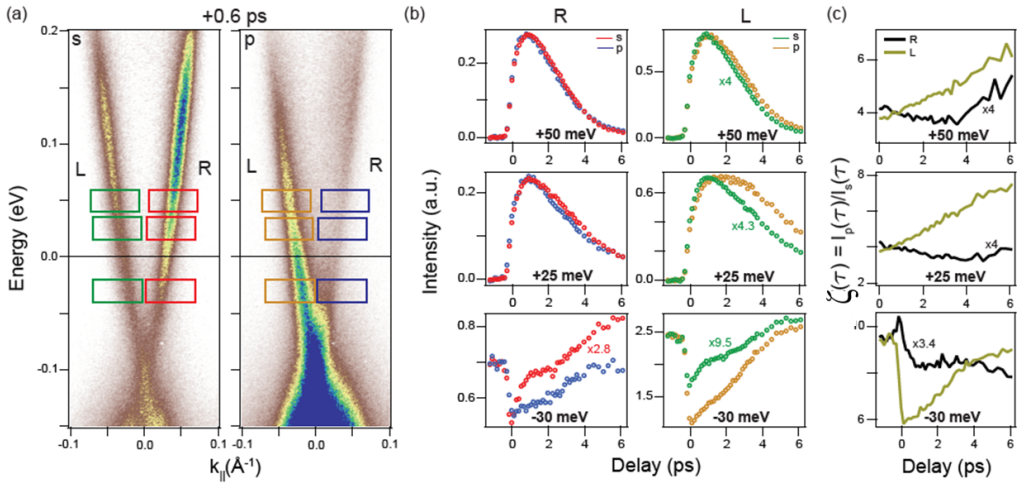

Fig. 4.11: (a) Out-of-equilibrium band mapping of the TSS at 600 fs pump-probe delay, probed with s (left) and p (right panel) polarization. (b) electronic dynamics at +60 meV, +30 meV, -30 meV and -60 meV resulting from the integration in colored boxes in (a). Red curves indicate s polarization, blue stay for p-polarization in the right (R) branch of the TSS. Green curves indicate s polarization, orange stay for p-polarization in the left (L) branch of the TSS. (c) Temporal evolution of $\zeta(\tau)$ as defined by eq. 4.4. From [12].

The TSS ARPES binding energy vs crystal momentum map is shown in Figure 4.11(a) at 600 fs pump-probe delay for two probe linear polarizations: vertical (s), left panel, and horizontal (p), right panel. Color boxes in Fig. 4.11(a) represent the integration region for the transient curves displayed in the panels of Fig. 4.11(b). In particular, red and blue circles are used for the right (R) branch of the TSS probed with s and p light, respectively. In analogy, green and yellow colours refer to the left branch probed by s and p probe light, respectively. The integration window used to extract the transient dynamics is 20 meV, comparable to our energy resolution. Remarkably, we observe that the temporal evolution of the integrated photoemission signal depends on the probe polarization. The intrinsic relaxation times of the TSS, described by the temporal evolution of the electronic distribution $f = f_{FD}(E_B, \mathbf{k}, T^*_{el}(\tau))$, should be independent of the probe polariza-

tion. Electronic relaxation mechanisms are in fact intrinsically related to the avaible decay channels characteristic of any fermionic bands. In addition, we have already discussed a transient modification of the TSS dispersion due to the coupling with pump-activated coherent phonons. This, within the photoemission intensity framework, is described by the temporal evolution of the one-electron removal spectral function $A = A_{\mathbf{k}}(E_B, \tau)$. We stress that even this term is probe-polarization independent. Thus, the discrepancy observed in the transient signal upon the two different probe polarization should be related just to the last term of the photoemisison intensity i.e. the matrix element $M = M^{\mathbf{k}}_{f,i}(\tau)$. As discussed in Chapter 3, the photoemission matrix element is the only term in the photoemission intensity which depends on the probe beam polarization. As already described, the photoemission matrix element can be written, in the sudden approximation, as:

$$M^{\mathbf{k}}_{f,i} = \left\langle \phi^{\mathbf{k}} f | \Delta | \phi^{\mathbf{k}}_i \right\rangle , \tag{4.3}$$

with $\phi^{\mathbf{k}} f$ and $\phi^{\mathbf{k}} i$ are the one electron final- and initial-state wavefunctions of the photoemission process. Δ is the light-matter interaction perturbation hamiltonian; in the dipole approximation it contains the probe vector potential $\mathbf{A}$ that is polarization-dependent. In addition, as shown by the comparison reported in Figure 4.10(d), transient reflectivity performed with the two linear polarizations of the probe does not show any different dynamics. The only remarkable difference between the two traces acquired with s and p probe polarization is an enhanced phonon signal for s-light. This implies two fundamental conclusions:

(i) one polarization has a greater sensibility in probing band structure parts mainly distorted by the activated transient deformation potential;

(ii) the observed difference in the dynamics observed by TR-ARPES is not related to physical properties of the sample.

Having identified the origin of the observed different dynamics, we need to develop a procedure to disentangle the transient evolution of the matrix-elements from the TR-ARPES intensity. We notice that the ratio between photoemission intensities achieved with different probe-polarizations is related only to the matrix elements of the two polarizations. The ratio function $\zeta(\tau)$ is defined as

$$\zeta(\tau) = \frac{I_p}{I_s}(\tau) = \frac{|M^p_{f,i}|^2}{|M^s_{f,i}|^2}(\tau). \tag{4.4}$$

Under the assumption that the pump excitation influenced just only electronic distribution $f = f_{FD}(E_B, \mathbf{k}, T^*_{el}(\tau))$ and one-removal spectral function

$A = A_{\mathbf{k}}(E_B, \tau)$, $\zeta(\tau)$ should be constant over any pump-probe delay. Given the observed dependence of the transient signal on the probe polarization in Fig. 4.11(b), we expect instead a temporal evolution of $M^p_{f,i}$ and $M^s_{f,i}$ and then of $\zeta(\tau)$.
To better clarify our experimental evidence we have plotted $\zeta(\tau)$ in Figure 4.11(c) as a function of pump-probe delay for the four binding energies previously investigated: +60 meV and + 30 meV, i.e. steady-state unoccupied bands, and -30 meV and -60 meV, i.e. equilibrium filled states. For the two energies above the Fermi level E_F, we plot $\zeta(\tau)$ only for positive delays in order to avoid division by zero due to unoccupied states before the pump arrival. Looking at Fig. 4.11(c), we clearly observed for all considered binding energies a temporal evolution of the ratio function $\zeta(\tau)$. Following the previous considerations, this confirms a modification of the matrix-elements ratio in time, i.e. a transient evolution of the matrix elements.
In the following, we try to address a possible mechanism at the base of the observed transient evolution of the ratio function $\zeta(\tau)$ in the $Bi_{1.1}Sb_{0.9}Te_2S$ topological insulator. Firstly, we notice that at negative binding energies, the dynamics of $\zeta(\tau)$ is pulsewidth limited (L branch at -30 meV and -60 meV panels in Fig. 4.11(c)). The temporal evolution of $\zeta(\tau)$ shows indeed a strong dependence on the binding energies and on the branch of the TSS. This suggests a strong dependence on the initial state wavefunction $\Psi_i = \Psi_{TSS}$. In particular, Ψ_{TSS} can be written as a complex combination of layer-dependent atomic orbitals. Thus, we state that the observed modification of the TSS due to the photo-excited phonon modes is followed by a non-trivial re-organization of the orbital character of Ψ_{TSS} through the quintuple-layer leading to the observed momentum and energy dependence of $\zeta(\tau)$. In addition, matrix element phase factors, i.e. interlayers quantum interference effects, can change upon lattice distortion via the modification of atomic layer distances. Both intertwined phenomena can resonably lead to a temporal evolution of $M^{s,p}_{f,i}(\tau)$. As a final remark, the system has been probed by a 6.2 eV probe beam. Thus, the final state in photoemission process cannot be approximated as a free-electron state. A modification of the final state, similar to the one occuring in the TSS initial state, could definitely contribute to the observed temporal evolution of the matrix element effect.

In conclusion, we thoroughly investigated transient response photoemission signal in $Bi_{1.1}Sb_{0.9}Te_2S$ topological insulator reporting a sizable photoinduced modification of the electronic band structure of the topological surface state. High-resolution transient reflectivity measurements identify fast and long standing phonon modes, i.e a photo-induced transient lattice distortion at

the base of the observed TSS dispersion modification. In addition, we have reported for the first time how this band dispersion modification leads to a transient evolution of the photoemission matrix elements trough a careful polarization-dependent investigation. These findings remark the complexity of the interpretation of TR-ARPES data that refer to quasi-particles temporal evolution. In particular, we provide an experimental way to determine whether dynamical matrix-elements contributions are present in the measured TR-ARPES.

Chapter 5

Origin of charge-density waves in 1T-$TiSe_2$

Glaciers melting in the dead of night
And the superstars sucked into the supermassive
(Ooh, you set my soul alight)

Supermassive Black Holes
from Black Holes and Revelations (2006), Muse

1T-$TiSe_2$ is a well-know layered transition metal dichalcogenides exhibiting a charge density wave (CDW) ground state below the critical temperature $T_{CDW} = 202$ K [108]. While this system is metallic above the transition temperature, the CDW formation comes together with a shift of the valence band ($\Delta E \approx 100$ meV) that turns 1T-$TiSe_2$ into a semiconductor.
Since the '70s, this transition has been extensively investigated. Despite the large number of studies reported in literature about the 1T-$TiSe_2$ CDWs phase transition, its driving underlying force has not been unambigously identified up today.
The reason for the ambiguity about the origin of the CDW phase in this compound is the fact that different possible scenarios equally explain the experimental observations. In addition, electron-hole, i.e. exciton, and electron-phonon interactions are usually simultaneously strong in real materials making it extremely difficult to resolve the dominant mechanism. The degeneracy about this interactions is lifted in the time-domain. In fact, purely electronic mechanisms are much faster than the one involving the lattice leading to different characteristic time-scales. Previous TR-ARPES experiments exploited extreme ultraviolet ultrashort pulses to investigate the CDW phase transition [107, 122, 173].These measurements observed a melting of the charge-order

within 100 fs. This temporal scale is too fast for a lattice-based mechanism suggesting the excitonic origin of the CDW phase in layered 1T-$TiSe_2$.

In this Chapter we will present our TR-ARPES measurements on the layered transition metal dichalcogenide 1T-$TiSe_2$. Our temporal resolution of 65 fs together with an energy resolution of ≈ 50 meV allows us to track the dynamics of the valence band shift upon optical excitation. Our results hint for key-role played by the lattice in the metal-to-insulator transition due to the CDW formation in 1T-$TiSe_2$.

5.1 Introduction

The layered transition metal dichalcogenide 1T-$TiSe_2$ undergoes a charge density wave (CDW) phase transition below the critical temperature $T_{CDW} =$ 202 K together with a 2x2x2 periodic lattice distortion (PLD) [108].
Despite this transition has been widely investigated since the '70s, an unambigous evidence of what is the driving force is not present up to today. Previous TR-ARPES measurements on 1T-$TiSe_2$ have been performed exploiting ultrashort extreme ultraviolet probe pulses [107, 122, 173]. Unfortunately, the energy resolution of this experimental configuration does not allow to track the temporal dynamics of the CDW insulating gap and the previous studies focus on the folded VB at the M-point. Its disappearing and recovery have been observed within 30 fs suggesting a purely electronic, i.e. excitonic, scenario. However, recent TR-optical spectroscopy [125] and TR-ARPES measurements [126] have pointed out a fundamental role of the PLD re-opening the question about the dominant mechanism of the (semi)metal-to-semiconductor transition in 1T-$TiSe_2$.

In the following sections we will present our TR-ARPES measurements investigating the dynamics of the CDW insulating gap. In particular, our optical fluence-dependent measurements hint to a non-trivial role of the phonons in the phase transition [15].

High quality 1T-$TiSe_2$ single crystals were grown by Charles Sayers under the supervision of Prof. Enrico Da Como at the Centre for Nanoscience and Nanotechnology (CNAN) and Centre for Photonics and Photonic Materials (CPPM) at the University of Bath (UK) using the chemical vapour transport method. Titanium (99.9%) and selenium (>99.9%) powders were sealed inside an evacuated quartz ampoule, together with iodine (>99.9%) which acts as the transport agent. To ensure the correct stoichiometry, a slight selenium

excess was included. Single crystals with a typical size of 4 x 4 x 0.1 mm^3 were selected for TR-ARPES measurements. Transport measurements confirmed the high-quality of these samples retrieving the characteristic features of th metal-to-semiconductor transition at T_{CDW} = 202 K [15].
TR-ARPES experiments have been performed on home built setup in Politecnico di Milano laboratories that is described in detail in Ref. [2] (see also Sec. 4.1). TR-reflectivity measurements have been performed in our laboratory at the Politecnico di Milano using as pump and probe the 1.85 eV pump beam of the TR-ARPES setup. The temporal resolution is about 30 fs. TR-reflectivity data have been taken in crossed polarization pump-probe scheme.
For TR-ARPES measurements, $TiSe_2$ samples were mounted on copper samples holder with conductive epoxy resin-based glue. A clean surface was obtained post-cleaving the samples in-situ at UHV pressure lower than 5 x 10^{-10} mbar. The samples orientation was verified by LEED measurements. All measurements have been performed at liquid nitrogen temperature or at room temperature, i.e. below and above T_{CDW}. The pump fluence has been set by means of linear attenuators.
The 6.02 eV probe energy does not allow to access the M-point but limits the measurable Brillouin zone to 0.2 $\mathring{A}^{-1}$ around the $\bar{\Gamma}$-point. However, the unique exceptional combination of temporal and energy resolution allows us to investigate the ultrafast dynamics of the CDWs energy gap providing a novel approach in the study of $TiSe_2$.

5.2 Ultrafast dynamics of charge-density waves band gap

Figure 5.1 shows the 6.02 eV probe ARPES maps around $\bar{\Gamma}$-point at 80 K, i.e. in the CDW phase, of 1T-$TiSe_2$ for three different pump-probe delays: (a) before the pump arrival, (b) at time zero, i.e. the maximum overlap between pump and probe beam and (c) 430 fs after the pump excitation.
In steady-state conditions, i.e. before the pump arrival (Fig. 5.1(a)), we retrieve the hole-like dispersion of the completelly occupied valence band (VB) marked by orange dashed lines. The maximum of the VB is $\approx$ 100 meV below the Fermi level hinting the presence of the CDW energy gap. Due to our short pulse duration, our energy resolution does not allow to clearly distinguish the two valence bands derived from Se-4p orbitals. In any case, this will not harm our conclusions. In particular, we point out that the top subband is the main responsible for the opening of the energy band gap Δ

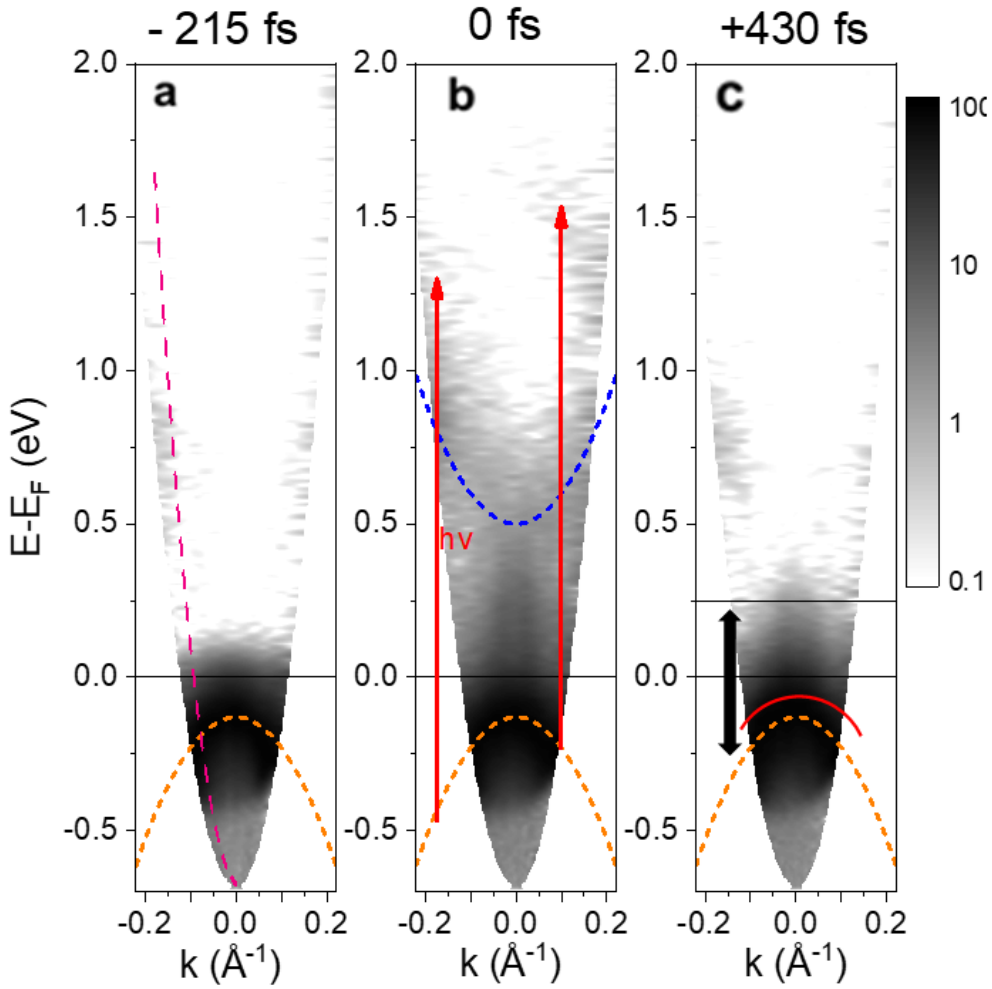

Fig. 5.1: ARPES maps of 1T-$TiSe_2$ at three different time delays between pump and probe: (a) before the pump arrival, (b) at time-zero and (c) after 430 fs from the pump excitation. The VB and CB curvatures are superimposed as orange and blue dotted curves, respectively. Dashed pink curve in (a) represents the -14° emission angle for the analysis of the VB dynamics. Red arrows in (b) indicate the optical transition associeted with the 1.85 eV pump beam. Black arrow and solid red curve in panel (c) indicate the VB spectral weight and maximum shift, respectively.

and for the overall shift of the VB [174]. Figure 5.1(b) reports the ARPES map as soon as the pump photoexcites the system. We observe a parabolic-like dispersing band about +1 eV above the Fermi level indicated by the blue dashed line. This feature can be ascribed to the pristine conduction

band (CB_p) at the $\bar{\Gamma}$-point. We want to stress that this is not in any relation with the folded conduction band from the $\bar{M}$-point. The pump beam mainly promotes electrons from the VB into the CB_p for **k**-states at the edge of our detectable window as shown by vertical red arrows in Fig. 5.1(b). The electrons relaxation from the CB_p is extremely fast. As shown in Fig. 5.1(c), after 400 fs the CB_p is almost empty. The extremely fast carrier relaxation in few hundreds of femtoseconds of the CB_p is in agreement with the semimetallic character of 1T-$TiSe_2$ [175]. Looking at Fig. 5.1(c), we notice that after photoexcitation the spectral weight of the valence bands shifts to higher energies as indicated by the black arrow. We report the shifted VB dispersion as red solid parabola in Fig. 5.1(c) to compare with the unperturbed one (orange dashed parabola). This observed shift to higher-energy suggests a reduction of the band gap. Therefore, it is indicative of a possible melting of the CDW phase and of a photo-induced transition to the metallic undistorted one.

In order to better clarify the closing of the band gap due to the VB shift and understand in more detail the physics behind the CDW phase transition in 1T-$TiSe_2$, we performed detailed time-resolved scans at one selected emission angle: -14° with respect to normal emission. This angle corresponds in reciprocal space to the pink dashed parabolic curve reported in Fig. 5.1(a). At the Fermi level, a crystal momentum $\mathbf{k}_{||}^{*} \approx -0.1\mathring{A}^{-1}$ coincides with the fixed emission angle. At this specific emission angle, the VB is well-separated from the Fermi level. Thus we can confidently disentangle the VB shift and the smearing of the Fermi-Dirac electronic distribution due to the transient photo-induce effective temperature. Figures 5.2 reports the time-resolved results at this cut. In particular, panels (a) and (c) refer to room temperature measurements, i.e. in the normal phase, while Fig. 5.2 (b) and (d) represent measurements performed at liquid nitrogen temperature T≈ 80 K, i.e. in the CDWs phase. Normalized energy distribution curves (EDCs) for some specific time delays are reported in Fig. 5.2 (a) and (b). Above the critical temperature (Fig. 5.2 (a)), the effect of the pump is to promote electrons above the Fermi level. At the same time, VB states below the Fermi level deplete. This behavior is in agreement with the general paradigma of TR-ARPES (see for example Chapter 4). In contrast, at low temperature (Fig. 5.2(b)) we observe a less trivial behavior. We point out that despite the presence of an energy band gap in the CDW phase, a non-zero electronic density of states (DOS) is found at the Fermi level even before the pump arrival (red curve). This is in agreement with measurements reported in Ref. [176]. At low temperature, after 50 fs from the pump arrival (blue curve), we observe an EDC remarkably different with respect to the steady-state one.

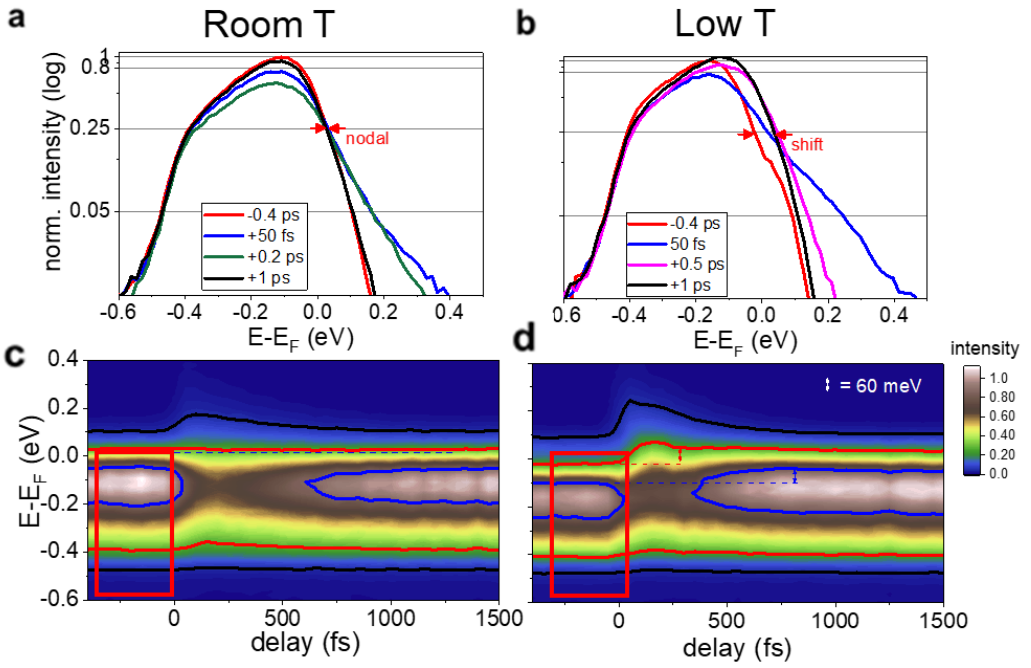

Fig. 5.2: Normalized energy distribution curves (EDCs) for selected pump-probe delays for measurements (a) above and (b) below the critical temperature T_{CDW}. Red arrows indicate the nodal point in room temperature measurements while they mark the shift of the VB in low temperature measurements. Photoemission intensity map binding energy vs pump-probe delays for measurements performed (c) above and (d) below the transition temperature. Black, red and blue contours stay for 0.05, 0.25 and 0.8 photoemission intensity in (a) and (b). Small arrows in panel (d) indicate 60 meV shift.

In particular, the smearing of the VB peak suggests a filling of the band gap in analogy with the quenching of the superconductivity gap recently reported in Ref. [151]. After hundreds of femtoseconds from the pump optical perturbation (pink and black curves), EDCs resemble the equilibrium one. Remarkably, the position of the peak edge is shifted up in energy by about 60 meV. Comparing the evolution of EDCs from spectra acquired above (a) and below (b) the critical temperature T_{CDW} the photo-induced shift of the valence bands becomes evident (see small red arrows). The dynamics of the VB shift is more evident looking at Figures 5.2 (c) and (d) where the normalized photoemission intensity is reported in a binding energy vs pump-probe delay map. The colored lines are constant intensity contour cuts, useful to identify specific features. In particular, blue lines represent 80% of the photoemission

intensity signal corresponding to the VB peak after 50 fs upon pump excitation both in room and low temperature measurements. Red lines stand for 25% intensity where we found the nodal and shift point of the VB in Fig. 5.2 (a) and (b). Finally, black lines represent 5% of the photoemission intensity, i.e. the electrons promoted above the Fermi level by the pump excitation. This latter one exhibit a trivial dynamics. A steep enhancement at time-zero followed by a relaxation within 500 fs is clearly present above and below the critical temperature in black lines. The dynamics of the peak (blue lines) and of the shift point (red lines) are by far more interesting. In particular, above the transition temperature T_{CDW} (Fig. 5.2(c)), both lines do not show any dynamics. This implies that the position of the valence bands peak does not change upon pumping. In contrast, for low temperature measurements (Fig. 5.2(d)), the same constant intensity cuts display a prompt step of about 60 meV (marked by colored arrows) around the zero pump-probe delay. This is a clear evidence of a photo-induced drifting to higher energies of the valence band. This process is extremely rapid. It occurs in fact within 100 fs. This short time scale suggests a purely electronic, i.e. excitonic, interaction as reported by previous TR-ARPES experiments focusing on the folded valence band at the M-point.
To better clarify whether this process is purely electronic or not, we compare the energy gap dynamics with a certainly purely electronic process: the temporal evolution of the spectral weight below the Fermi level. The results are shown in the following.

Figures 5.3(a) and (b) show the temporal evolution of the spectral weight obtained integrating all states up to the Fermi level (red rectangles in Fig. 5.3 (c) and (d)). At room temperature, panel (a), we observe a strong reduction (about 30% of the spectral weight) whithin few hundreds of femtoseconds. Then, the spectral weight completely recovers in few picoseconds. This large reduction is in agreement with the depletion of the VB due to the pump optical excitation. We point out that the maximum depletion is slightly delayed occuring 150-200 fs after the pump optical excitation. This is explained considering the possible vertical optical transitions promoted by the pump beam (as a reference, see Fig. 5.1(b)). The direct optical transition between the valence band and the pristine conduction band takes place for $\mathbf{k}_{||}$ values away from the $\bar{\Gamma}$-point. Thus, in the deeper energy region of the valence bands holes remain. Via intraband scattering processes these holes move toward the $\bar{\Gamma}$-point, i.e. the highest available energy level. Equivalently, electrons migrate to larger binding energies and fill the empty states left behind by the optical transition. The observed build-up of the depletion strongly suggests the presence of these intraband scattering processes.

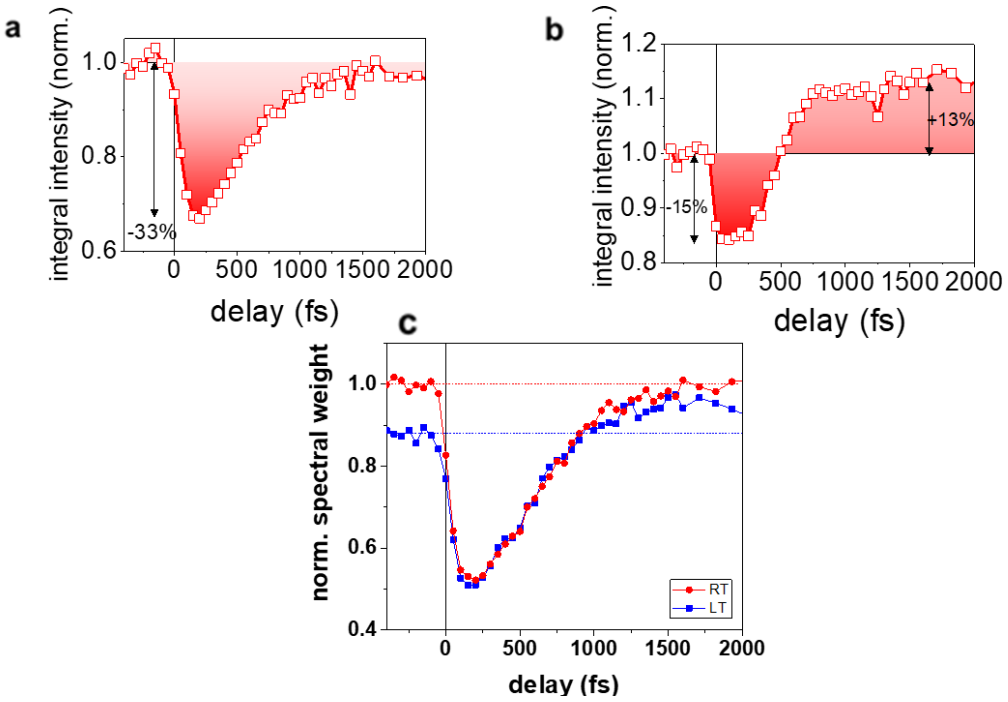

Fig. 5.3: Spectral weight temporal evolution for measurements performed (a) above and (b) below the transition temperature. The spectral weight is obtained integrating over all the states below the Fermi level (red rectangles in Fig. 5.2(c) and (d)). (c) Comparison between normalized spectral weight dynamics for measurements above (red circles) and below (blue squares) the transition temperature.

In the CDW phase (panel (b)) we still observe a very fast but less pronounced reduction of the spectral weight ($\approx 15\%$). In addition, at large delays we observed an increment of the spectral weight of about 13%. We attribute this enhancement of the spectral weight to the unfolding of the VB at the pristine $\bar{M}$-point as a consequence of the photo-induced melting of the CDW/PLD. Unfortunately, from these data it is not possible to infer the time scale of the unfolding, i.e. of the CDW melting, because of the strong entanglement with the depletion process.

The origin of the gain in spectral weight observed in Fig. 5.3(b) is confirmed by directly comparing integrated intensities above and below the transition temperature T_{CDW} as shown in Fig. 5.3(c). Here, the red circles represent the integrated intensity for room temperature measurements while the blue squares for low temperature measurements. We point out that we performed in rapid sequence time-resolved acquisition of photoemission spectra above and below the transition temperature in order to ensure high laser stability

and the same optical fluence. This allows us also to track the position on the sample during the cooling ensuring to measure the same spot on the surface in both cases. Comparing red (room temperature) and blue (low temperature) curves in Fig. 5.3(c) we can easily see that before pumping the spectral intensity in the VB peak is lower in the CDW phase than in the metallic undistorted phase. This indicates a loss of the spectral weight associated with this feature during the CDWs phase transition. The lower spectral weight in the CDW phase suggests that it has transferred from the $\bar{\Gamma}$-point to the folded band in $\bar{M}$-point. This conclusion is enforced looking at the dynamics of the two curves in Fig. 5.3(c). Although they start from different values they both approach the same spectral weight at long delays. Then, upon the pump excitation the charge-order is melted and the folded valence bands at the $\bar{M}$-point vanishes. As consequence, the spectral weight is transferred back to the $\bar{\Gamma}$-point.

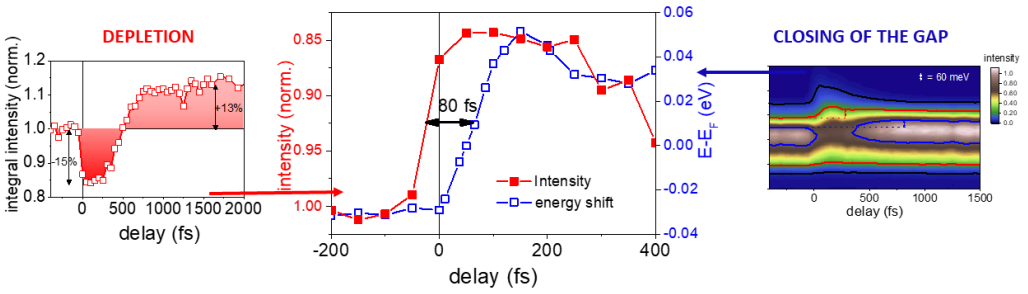

Fig. 5.4: Comparison between spectral-weight (red filled squares) and VB shift (blue empty squares) dynamics. A clear delay of about 80 fs is found.

Having clarified the dynamics of the spectral weight associated with the VB, we now want to compare this electronic effect with the previously discussed ultrafast dynamics of the energy band gap, i.e. the shift of the spectral weight. In figure 5.4 the comparison between the dynamics of the spectral weight associated with the photo-induced depletion (red curve) and of the gap closing (blue curve) as deduced for the contour plot in the binding energy vs. pump-probe delay map is reported. Data have been rescaled for an easier visualization. The most striking fact is the presence of a delay of about 80 fs between the VB peak intensity (i.e. depletion plus unfolding) dynamics and the change of the VB peak position (i.e. the gap closing). Previous TR-ARPES measurements have discussed the ultrafast disappering of the folded VB at the $\bar{M}$-point as a signature of the optically-induced CDW transition to the metallic phase [107, 122, 173]. This dynamics is represented by our

data about the temporal evolution of the spectral weight associated with the VB at $\bar{\Gamma}$-point. Following this assumption, we have evidence that the energy shift is subsequent to the phase transformation.
In a purely excitonic scenario, the CDWs phase transition is described by a non-zero order parameter Δ that rules directly the electronic dispersion relation of valence and conduction bands (see Sec. 2.1.7) [112, 117, 120]. In this scenario, Δ is at the base of the spectral weight transfer and of even the energy shift of the valence band, i.e. the opening of the CDWs gap, at temperature below T_{CDW}. Above the transition temperature, Δ drops to zero leading the system to the undistorted ungapped band structure. Thus, a photo-induced modification of the spectral weight represents a photo-induced modification of Δ and as a consequence an optically-triggered semimetal-to-semiconductor transition. If we assume that the CDW in 1T-$TiSe_2$ is a purely excitonic phenomenon, we expect that the evolution of the spectral weight and of the VB shift occur simultaneously, since a unique parameter rules both of them. This is clearly in contrast with what we experimentally observed and reported in Fig. 5.4.

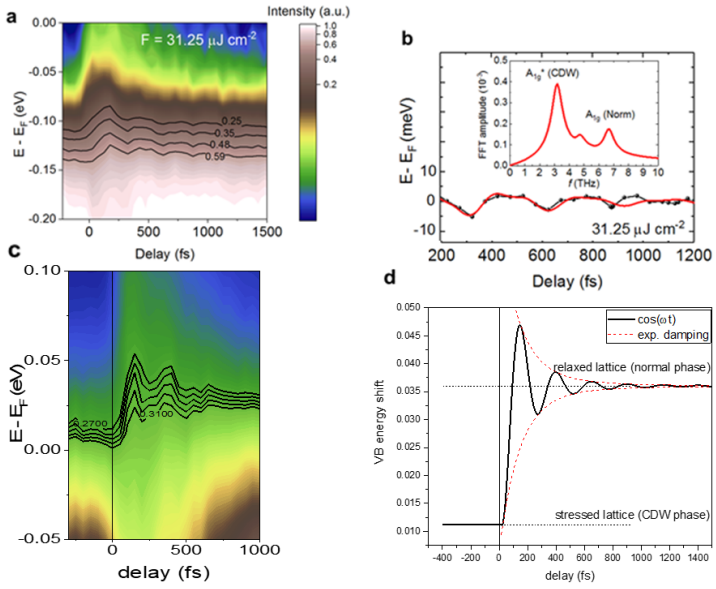

Fig. 5.5: (a) and (c) Coherent oscillations in the VB dynamics for two independent sets of measurements. The black lines are tentative fits with the model in (d): a damped cosine function with the A_{1g}^* phonon mode. (b) VB dynamics after subtraction of the intensity decay (black dots) superimposed to sinusoidal fitting functions (red). The inset shows the FFT amplitude for the three frequencies used in the fitting.

Looking closely at the VB shift dynamics reveals additional intersting aspects helpful to clarify the mechanism ruling the gap dynamics and the reason of the delay with respect to the spectral weight temporal evolution discussed so far. Figures 5.5 (a) and (c) show a closeup of the VB shift dynamics at low temperature within 200 meV around Fermi level for two independent sets of measurements. Some contour cuts of the spectral intensity are highlighted (black curves) to help the following discussion. Besides the prompt energy shift of the valence band position already discussed, Fig. 5.5(a) and (c) highlight the presence of some strongly damped oscillations at positive delay. Subctracting an exponential intensity decay from Fig. 5.5(a), the oscillating dynamics (black dots) can be fitted by a combination of sinusoidal functions with different characteristic frequencies (red solid line) as shown in Fig. 5.5(b). The inset of Fig. 5.5(b) shows the fast Fourier transform (FTT) for the three frequencies used in the fitting. In particular, we observe that the VB dynamics oscillations are in agreement with the phonon frequencies of A_{1g}^{*} mode in CDW/PLD phase (3 THz) and the A_{1g} mode in the undistorted lattice phase ($\approx$ 7 THz). This observation strongly suggests a fundamental role played by the phonons population in the VB dynamics. As discussed in Chapter 2, theoretical calculations have shown how the lattice distortion through a modification of the Ti-Se bond length can lower the energy of the VB via a pseudo Jahn-Teller effect, i.e. opening of the CDW band gap [96, 101, 102, 108]. The thick black curves in Fig. 5.5(c) are tentative

fits based on a simple model shown in Fig. 5.5(d): an exponentially damped cosine function oscillating with a period of 250-280 fs, in good agreement with the period of the A_{1g}^{*} phonon mode [126].

The observation of the phononic oscillations in the VB shift dynamics helps to clarify the delay reported in Fig. 5.4. This delay is just apparent. It is due to the presence of two different mechanisms, (i) electronic interactions vs (ii) lattice-based mechanism, that are simultaneously triggered by the pump laser excitation but take place on different typical time-scales. In particular, the pump photo-induces lattice motion, i.e. we have an impulsive response of the phononic population (as suggested by the cosine function used in the fits of Fig. 5.5(c) and (d)) that justifies the observed apparent delay.

Our experimental observation focusing on the CDW gap closing dynamics rather than the unfolding of the VB at the $\bar{M}$-point highlights the fundamental key role played by the lattice in the CDW phase transition in 1T-$TiSe_2$. The purely excitonic scenario is not consistent with the experimental data that suggests instead a cooperative Jahn-Teller-excitonic model (as recently suggested [177]).

In the following, we show our TR-ARPES measurements of the VB shift as function of the pump optical -fluence. These measurements help us clarify

the fundamental role of the lattice in the CDW phase transition.

5.2.1 Fluence dependent measurements

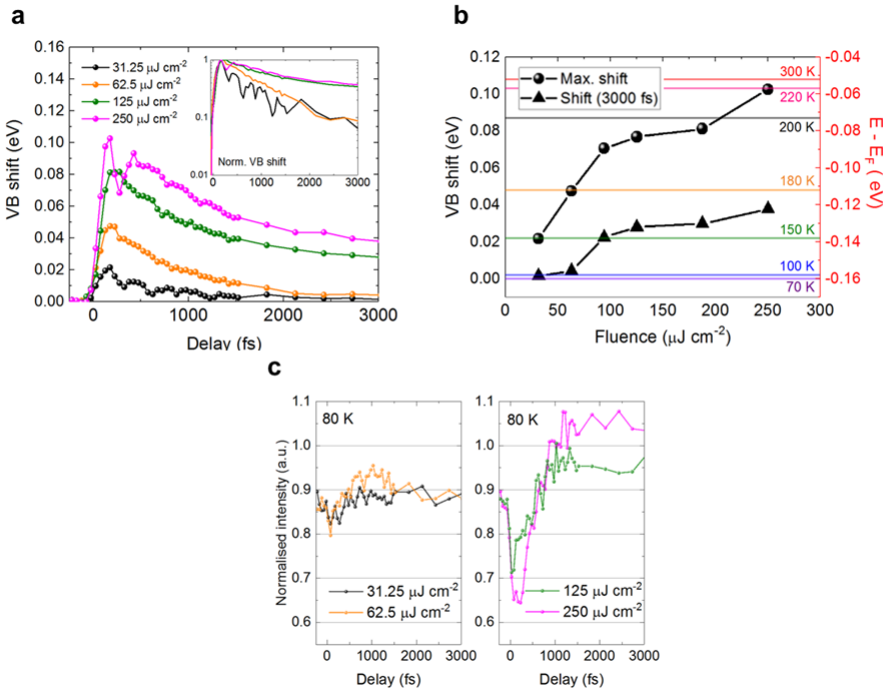

Fig. 5.6: (a) VB energy shift temporal evolution for different pump laser fluences as indicated in the main panel, sample temperature is 80 K. The inset shows the same data normalized at the maximum VB energy shift on a logarithmic energy scale. (b) Maximum VB shift (dots) and shift at 3 ps (triangles) extracted from panel (a) as a function of fluence. The horizontal lines are linked to right axis and are the VB energy determined by high resolution steady state ARPES at different temperatures as indicated, reproduced from Ref. [178]. (c) Spectral weight temporal evolution at 80 K scaled for the normalized intensity at room temperature and for different laser fluence as indicated. From [15].

Figure 5.6 summarizes the VB shift and the temporal evolution of the spectral weight as a function of the fluence. Figure 5.6(a) reports a comparison among the VB dynamics for selected fluences. For all traces, the maximum of the shift occurs within 200 fs. The largest shift of 100 meV is found for fluences of $250\frac{\mu J}{cm^2}$, comparable with the CDWs energy band gap. Looking at the VB dynamics, we notice that only for the two lowest fluences

(31 $\frac{\mu J}{cm^2}$ and 62.5 $\frac{\mu J}{cm^2}$) there is a complete recovery of the VB position, i.e a re-opening of the band gap, after 2 picoseconds from the pump pulse. In contrast, for higher fluences, a complete recovery is never detected within the measured time window. The inset of Fig. 5.6(a) shows the same data normalized and plotted on a logarithmic scale. Here, the different recovery dynamics appear more clearly. In particular, the inset of Fig. 5.6(a) suggests the presence of two regimes, with a thresold between them. At fluences larger than 62.5 $\frac{\mu J}{cm^2}$ an extremely long life time of the VB shift with a non mono-exponential decay is revealed while for lower fluences an exponential faster decay is observed.
Figure 5.6(b) shows the VB shift as a function of the fluence for the time delay corresponding to the maximum shift (dots) and for $\Delta t = 3$ ps to help clarify the different relaxation time-scale discussed so far. The colored lines reported in Fig. 5.6(b) refer to the right red ordinate axis and they represent the VB position at different temperatures derived from high-resolution temperature-dependent ARPES measurements [178]. The aim of this comparison is to highlight the correlation between the valence band shift and the perturbation of the charge-order. For fluences lower than ≈ 100 $\frac{\mu J}{cm^2}$, the VB shifts linearly with the fluence. Then, a plateu region is identified between 100 $\frac{\mu J}{cm^2}$ and 200 $\frac{\mu J}{cm^2}$. Only for fluences larger than 200 $\frac{\mu J}{cm^2}$ the VB is transiently shifted above the 200 K black horizontal line, i.e. above the critical temperature T_{CDW}. This is in agreement with the previous observation of a complete closing of the energy gap Δ for this fluence. For this reason, in the following, we will refer to this fluence as $F_{CDW} = 200$ $\frac{\mu J}{cm^2}$, i.e. the critical fluence to achieved the transient complete suppression of the CDW/PLD band gap.
The position of the VB shift at $\Delta t = 3$ ps (triangles in Fig. 5.6(b)) helps identify the threshold between the two regimes discussed so far. The Vb shift after 3 picoseconds from the pump excitation exhibits a flex point around 70 $\frac{\mu J}{cm^2}$ suggesting in this fluence the threshold where the VB shift dynamics changes and a longer recovery occurs. This threshold fluence F_{Th} does not coincide with F_{CDW} but occurs at about a third of its value, i.e. $F_{Th} \approx \frac{F_{CDW}}{3}$.

We now look at the temporal evolution of the spectral weight as a function of the pump fluence. The left panel of Fig. 5.6(c) shows the spectral weight obtained as integration on all states below the Fermi level for fluences lower than F_{Th}. The data have been normalized on the spectral weight of the metallic phase, i.e. from room temperature measurements, before the pump arrival. Here we can clearly notice an initial fast loss of spectral weight associated with a pump-induced depletion. The spectral weight recovers within 600 fs for both fluences. We want to point out that for a fluence of 62.5

$\frac{\mu J}{cm^2}$ (orange curve), at around 500 fs the spectral weight crosses the initial normalized intensity showing a small, ultrafast enhancement. A similar effect has been described in the previous section and ascribed to the unfolding of the VB at the M-point. In the right panel of Fig. 5.6(c) we report the evolution of the spectral weight for the higher fluences in Fig. 5.6(a), i.e. for the fluences exhibiting a persistent perturbation of the VB shift. Even in this case, we notice a similar enhancement of the spectral weight around 500 fs. For these two fluences, the *gain* is more pronounced and long-lasting. This gain can be related to the unfolding of the spectral weight of the VB at the M-point, i.e. the loss of PLD.

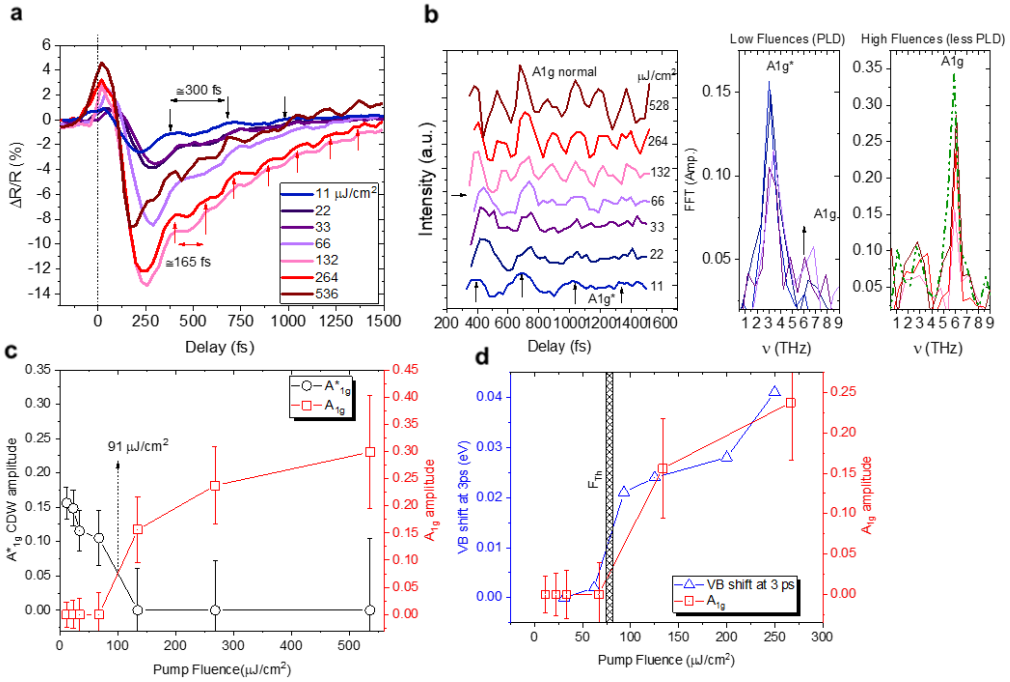

Fig. 5.7: (a) Differential reflectivity dynamics for different fluences. (b) Coherent oscillations after subtraction of the exponential decay by the traces in (a). Right panels report FFT amplitude for the oscillations. Green dashed curve represents the FFT of oscillations measured in a 300 K time-resolved reflectivity experiment. (c) Amplitude of the A^*_{1g} and of the A_{1g} modes, representative of the distorted lattice and normal phase structure respectively, as a function of fluence. (d) Comparison between the fluence dependence of the A_{1g} amplitude and the VB shift at 3000 fs (black triangles) from Fig. 5.1.

As seen in the previous section, our TR-ARPES data suggest that the en-

ergy band gap Δ, the order parameter of the CDW phase, has both excitonic and lattice contributions, the extent of which remains unknown. Our fluence dependent measurements in a regime so-far unexplored in TR-ARPES experiments on 1T-$TiSe_2$ confirm this cooperative mechanism. Previous transient optical experiments in the low fluence regime have clarified that the initial perturbation of the CDW upon pump excitation is non-thermal, i.e. mainly related to the electronic order since purely electronic interactions occur on the time scale of a few tens of femtoseconds [125, 179]. This means that a femtosecond optical pump mainly perturbs the excitonic order rather than heating up the lattice system. Following this interpretation, the dynamics of the VB shift observed for the lower fluences, i.e below F_{Th}, can be undestrood in terms of electronic dynamics only, rather than electronic and lattice. Thus, for a fluence regime lower than F_{Th}, only the excitonic part of Δ is influenced by the pump optical perturbation. In contrast, the long recovery time observed above for fluences above the F_{Th} suggests the presence of a different mechanism, additional to the excitonic photo-induced perturbation. We notice that the VB shift at the F_{Th} almost corresponds to an equivalent VB shift at 150 K ARPES measurements. Remarkably, this temperature has been reported as the critical temperature to observe the disappearance of the PLD signatures in recent THz experiments. This suggests that the long-lasting shift for large fluences is due to a photo-induced melting of the PLD [125]. As discussed at the end of the previous section, the VB shift dynamics is strongly modulated by the A_{1g} phonons in agreement with a pseudo Jahn-Teller mechanism.

In order to better characterize the role played by the phonon modes in the shift of the valence band, we have performed high- temporal resolution time-resolved reflectivity measurements. 1T-$TiSe_2$ single crystal have been optically excited by 1.85 eV, 30 fs pump pulses, i.e the same pump beam of TR-ARPES experiments. The 1.85 eV beam has been used also to probe the reflectivity with crossed polarization with respect to the pump. Figure 5.7(a) reports the differential reflectivity signal for different pump fluence. Two different frequency oscillations can be observed for lower and higher fluences. After a subtraction of an exponential decay for traces in Fig. 5.7, oscillations are clearly observable for all fluences (see Fig. 5.7(b) (left panel)). The right panels of Fig. 5.7(b) show the Fast Fourier Transform (FFT) of the oscillations oberved in the differential reflectivity traces. We can clearly notice that for lower fluences the A_{1g}^* phonon mode is dominant. This mode is a consequence of the 2x2x2 PLD and it is not present in the undistorted structure of 1T-$TiSe_2$. In contrast, for higher fluences the amplitude of the A_{1g} mode is the most relevant. The FFT of the differential reflectivity trace acquired at room temperature, i.e. in the normal phase (green dashed line),

confirms that the A_{1g} is the proper mode of the normal undistorted structure. Figure 5.7(c) shows how the contribution of the coherently coupled phonons changes as a function of different fluences. For fluences lower than F_{Th} the largest contribution is due to the A^*_{1g} phonon mode. Increasing the fluence, the A^*_{1g} phonon mode reduces, while the A_{1g} mode of the undistorted lattice structure becomes more and more relevant. The progressive shift of the coupling towards the A_{1g} mode implies a progressive loss of the PLD as also supported by the unfolding mechanism highlighted by spectral-weight dynamics in Fig. 5.6(c). Remarkably, the switching of the dominant mode occurs around F_{Th}, i.e. the threshold fluence between the two VB dynamics regimes dicussed above. As shown in Fig. 5.7(d), the VB shift at 3 ps reported from Fig. 5.6(b) (black open triangles) exhibits the same fluence-dependence of the A_{1g} amplitude mode. Thus, we can understand the different dynamical regime in terms of coupling with the lattice. For all fluences the recovery of the CDW order parameter, i.e. the energy gap Δ is coupled with phonons. For fluences lower than F_{Th}, the A^*_{1g} excited phonon mode, proper of the distorted lattice, favors the re-establishment of the perturbed excitonic order as reported in Ref. [179]. In contrast, for higher fluences the photo-induced heating of the lattice drives the melting of the PLD. The rearrangement of the lattice to the pristine unperturbed structure diminishes the population of the A^*_{1g} phonon mode. The VB then, according to the pseudo Jahn-Teller mechanism, moves up towards the Fermi level. In this condition, the A_{1g} excited phonon population does not favor the PLD, i.e. the restoring of the CDW phase and the re-opening of the band gap. Therefore, the VB position remains at higher energy for a longer time as observed in Fig. 5.6(a).

In conclusion, our TR-ARPES measurements focusing for the first time on the dynamics of the valence bands at the $\bar{\Gamma}$ point provide a new insight about the origin of the charge density waves phase in the layered transition metal dichalcogenide 1T-$TiSe_2$. In particular, we found a clear evidence of a fundamental role played by the phonon population, suggesting an excitonic-lattice cooperative scenario.

Conclusions and Outlooks

In this thesis we employed photoemission pump-probe measurements on the layered metal chalcogenides $Bi_xSb_{2-x}Te_ySe_{3-y}$ topological insulator and on 1T-$TiSe_2$ to investigate phenomena triggered by ultrashort light pulses. In the following we summarized the major findings of this thesis.

In the $Bi_xSb_{2-x}Te_ySe_{3-y}$ family stoichiometry strongly affects the morphology of the TSS and the position of the Dirac point, i.e. the point where the two branches of the Dirac cone cross with respect to the Fermi level [9, 28]. Our TR-ARPES measurements as a function of the stoichiometry reveal the central role of the Dirac point position in the dynamics of the TSS [9]. In particular, we observed that for stoichiometries where the Fermi level crosses the valence or conduction bulk bands the TSS photo-excited population exhibits a fast decay. In contrast, when the Dirac point lies at the Fermi level, the TSS is less affected by the presence of the bulk and an extraordinary long lifetime of Dirac fermions is found. We provided a complete description of these observations in terms of Fermi's Golden rule and bottleneck effect at the Dirac point due to the reduced phase-space. Our investigation of the out-of-equilibrium properties of the $Bi_xSb_{2-x}Te_ySe_{3-y}$ as a function of the stoichiometry reveals the capability to efficiently manipulate the Dirac fermions population providing an excellent platform to novel devices based on topological insulators.

In order to reveal the microscopical mechanism at the base of the reported surface spin current induced by circularly-polarized photons [8], we have performed TR-ARPES measurements using circular pump beam. Theoretical works have described the origin of the spin-current in the asymmetric population excited by circular photons [73, 74]. They in fact predicted that in the presence of a non-zero spin-orbit coupling the circular photons trigger

electronic transitions in a spin-dependent way, in analogy with the optical orientation in semiconductors [163]. Due to the spin-momentum texture of the TSS, this selective excitation leads to a **k**-space asymmetry and then to a spin current in surface states. While in topological insulators no TR-ARPES measurement has shown a direct coupling of visible pump photons with the TSS, we have demonstrated to be able to directly populate the empty topological surface state (ESS) of the Bi_2Se_3 because of our pump energy of 1.85 eV. In addition, we have observed that a given helicity of the pump is able to populate only one branch of the ESS generating a k-asymmetric spin-population. The $\mathbf{k}_{||}$-dependent temporal evolutions of the spin-polarized population of the ESS has been found to be in agreement with theoretical models. In particular, the observation of an ultrafast build-up of the spin-polarized electron population in the ESS reveals the optically-triggered spin-current in the Bi_2Se_3, the prototypical topological insulator [10, 11].

Our high temporal resolution TR-Reflectivity measurements on the topological insulator $Bi_{1.1}Sb_{0.9}Te_2S$ clearly reveal the optically-triggered optical and acoustic phonon modes. These observations help clarify the TR-ARPES measurements performed at the University of British Columbia by prof. Damascelli's group. They observed a different dynamics of Dirac fermions as a function of the linear polarization of the probe beam. Combining TR-Reflectivity and TR-ARPES data we explained this discrepancy as a consequence of the modification of the TSS wavefunction due to the optically-triggered phonon modes. This leads to transient changes of the photoemission matrix elements, strongly dependent on the non-trivial TSS wavefunction. This fundamental result raises doubts about how much the transient TR-ARPES intensity is related to the evolution of the electronic and quasiparticles populations [12].

The layered 1T-$TiSe_2$ is an attracting material being the first in which the Bose-Einstein condensate of excitons has been experimentally found [13]. It shows a (semi)metal-to-insulator transition driven by the formation of a charge density wave together with a periodic lattice distortion [14]. The driving force of this transition is not clear and is still debated. Our fluence-dependence TR-ARPES and TR-Reflectivity measurements suggest an excitonic-lattice cooperative mechanism as the origin of the charge density wave phase in 1T-$TiSe_2$ [15]. Fluence-dependence TR-ARPES data reveal two different dynamics of the optically-triggered collapse of the electronic gap: below a threshold fluence F_{Th} the perturbed gap restores within several picoseconds, at higher fluences it shows a long standing perturbation. Remarkably, we have observed the same fluence-dependence in the dominant

phonon oscillation in our TR-Reflectivity measurements. For fluences lower than F_{Th} in fact the reflectivity signal is modulated by the phonon mode proper of the charge density wave phase while at higher fluences the normal phase phonon mode becomes relevant. This strong entanglement between band gap and phonon modes behavior as a function of the fluence suggests a key-role played by the lattice in the dynamics of the electronic band-gap and it indicates a cooperative excitonic-lattice model.

In conclusion, out-of-equilibrium spectroscopies are fundamental tools for investigating layered two-dimensional systems as shown in this thesis. Nowadays, this class of materials is increasing fast, proffering ever-new electronic properties and physical challenges. It is for example the case of the very recently reported enhanced charge density wave order of the monolayer VSe_2 grown on bi-layer graphene/SiC [180]. This is just one example indicating the sensitive balance that can be realised between competing interacting phases in monolayer transition-metal dichalcogenides. In this growing interesting field, TR-ARPES and TR-optical spectroscopies provide a fundamental insight to clarify the arising novel phenomena.

Acknowledgments

Per ogni giorno, ogni istante, ogni attimo
Che sto vivendo
Grazie mille

Grazie Mille
from Grazie Mille (1999), 883

When you start a PhD you are like a novel Don Quixote, full of ideals, brave-heart, ready to fight any adversity and overcome any challenges to achieve your goals, to improve the World. At the end, you have crashed against so many *giants*, invincible windmills and sheeps armies that they can break your soul if you do not have very special people around you, able with a smile and a good word to make your day. Here I want to thank all of these people, so fundamental during this picaresque adventure called Doctorate.
Writing the acknowledgments, however, is usually considered one of the most difficult part of writing a thesis: you have to remember any important person being sure to forget someone. This will be the case, I am sure, and I apologize in advance for those I will forget to mention. If we have shared a coffee or a short chat in a bad day, I sincerely thank you.
Of course, there are people that it is impossible to forget.
First of all, I would like to thank Claudia and Ettore for the great opportunity that you have offered me three years ago. I learnt a lot from you, about the joy and the beauty of the research, the required skills to pursue a goal. I arrived in your group as a young grad student, I hope to leave having gained a bit of your wide knowledge. Thank you for your patience, for your support. Working with you, having the possibility to receive your advices and teachings has been for me a great honor. I will hold onto this experience for every day of my life.
I would like to thank Prof. Marco Grioni for hosting me in his group at

the EPFL. This experience is extraordinary and it is teaching me a lot not only about the science and the reasearch. And I would like to thank the Swiss State Secretariat for Education, Research and Innovation (SERI) for the Scholarship that supported my visiting period at Lausanne.
Thanks to Hamoon, that during this three years helped me in the lab and not only. The time that we have spent together discussing about our setups, our experiments and data but also about our travels, countries, politics, anything has been extremely precious for me. I wish you all the best for your future and your career and I hope to work again with you one day.
Thanks to Fabio, for being a good friend. Even if you are literally on the other side of the World you have always found time for chatting with me. Your advices are precious as much as your friendship for me.
Thanks to EPFL people: Alberto, Silvan, Michele that are patiently teaching and helping me, thank you so much. And Gianmarco, Mauro, Tania, Luca, Gloria, Patrick, Michael to have made the time in Switzerland funnier and easier. I will miss our board-games dinner. And thanks to PoliMi people: Michele, Sara, Matteo, Stefano, Argyro, Lavinia, Carlo, Giulia, Alberto, Davide, Ross, Cristian for any coffee break and funny discussion.
The life is a journey and any stop is important. For this reason I would like to thank Francesco, Diego, Carlo, friends from my previous stop as master students. You are the best guys! When I needed help you were on my side and I will always be present when you will need.
Thanks to my family, to my parents that still believe I am playing with magic. You probably are still secretly thinking that I am not doing a real job but you supported all my choices. Everyday you make me feel how much you are proud and love me. I am so lucky to have you!
And last but never least, thanks to Egle, *mo cuisle*, my support and my strength. Without you the discouragement would have won. Thanks for sharing all this with me. Thanks for patiently going through these years. Thanks for supporting my decisions. Even if this last year has been a little bit tough for us, you have been by my side. You are the best and I can just say to you once again: thank you!

Bibliography

[1] M. Grioni, S. Pons, and E. Frantzeskakis, "Recent ARPES experiments on quasi-1D bulk materials and artificial structures," *Journal of Physics: Condensed Matter*, vol. 21, no. 2, p. 023201, 2008.

[2] F. Boschini, H. Hedayat, C. Dallera, P. Farinello, C. Manzoni, A. Magrez, H. Berger, G. Cerullo, and E. Carpene, "An innovative Yb-based ultrafast deep ultraviolet source for time-resolved photoemission experiments," *Review of Scientific Instruments*, vol. 85, no. 12, 2014.

[3] B. Yan and S.-C. Zhang, "Topological materials," *Reports on Progress in Physics*, vol. 75, no. 9, p. 096501, 2012.

[4] Y. Ando, "Topological insulator materials," *Journal of the Physical Society of Japan*, vol. 82, no. 10, p. 102001, 2013.

[5] M. Z. Hasan and C. L. Kane, "*Colloquium* : Topological insulators," *Rev. Mod. Phys.*, vol. 82, pp. 3045–3067, Nov 2010.

[6] C. Jozwiak, C.-H. Park, K. Gotlieb, C. Hwang, D.-H. Lee, S. G. Louie, J. D. Denlinger, C. R. Rotundu, R. J. Birgeneau, Z. Hussain, *et al.*, "Photoelectron spin-flipping and texture manipulation in a topological insulator," *Nature Physics*, vol. 9, no. 5, pp. 293–298, 2013.

[7] Z.-H. Zhu, N. Veenstra, C. S. Zhdanovich, P. Schneider, M. T. Okuda, K. Miyamoto, S.-Y. Zhu, H. Namatame, M. Taniguchi, W. Haverkort, M. S. Elfimov, I. and A. Damascelli, "Photoelectron spin-polarization control in the topological insulator Bi_2Se_3," *Phys. Rev. Lett.*, vol. 112, p. 076802, Feb 2014.

[8] J. McIver, D. Hsieh, H. Steinberg, P. Jarillo-Herrero, and N. Gedik, "Control over topological insulator photocurrents with light polarization," *Nature nanotechnology*, vol. 7, no. 2, pp. 96–100, 2012.

[9] H. Hedayat, D. Bugini, H. Yi, C. Chen, X. Zhou, G. Cerullo, C. Dallera, and E. Carpene, "Surface state dynamics of topological insulators investigated by femtosecond time- and angle-resolved photoemission spectroscopy," *Applied Sciences*, vol. 8, p. 694, Apr 2018.

[10] D. Bugini, F. Boschini, H. Hedayat, H. Yi, C. Chen, X. Zhou, C. Manzoni, C. Dallera, G. Cerullo, and E. Carpene, "Ultrafast spin-polarized electron dynamics in the unoccupied topological surface state of Bi_2Se_3," *Journal of Physics: Condensed Matter*, vol. 29, no. 30, p. 30LT01, 2017.

[11] D. Bugini, H. Hedayat, F. Boschini, H. Yi, C. Chen, X. Zhou, C. Manzoni, C. Dallera, G. Cerullo, and E. Carpene, "Circularly polarized light interaction in topological insulators investigated by time-resolved ARPES," in *Journal of Physics: Conference Series*, vol. 903, p. 012036, IOP Publishing, 2017.

[12] F. Boschini, M. Zonno, D. Bugini, E. Razzoli, M. Minchiardi, H. da Silva Neto, E, S. Dal Conte, P. Day, R, M. Schneider, B. Zwartsenberg, P. Nigge, K. Kushwaha, S, J. Cava, R, S. Zhdanovich, K. Mills, A, G. Levy, C. Giannetti, G. Cerullo, J. Jones, D, and A. Damascelli, "Role of matrix-elements in the time-resolved photoemission signal: the case of $Bi_{1.1}Sb_{0.9}Te_2$s topological insulator," *In preparation.*

[13] A. Kogar, M. S. Rak, S. Vig, A. A. Husain, F. Flicker, Y. I. Joe, L. Venema, G. J. MacDougall, T. C. Chiang, E. Fradkin, *et al.*, "Signatures of exciton condensation in a transition metal dichalcogenide," *Science*, vol. 358, no. 6368, pp. 1314–1317, 2017.

[14] K. Rossnagel, "On the origin of charge-density waves in select layered transition-metal dichalcogenides," *Journal of Physics: Condensed Matter*, vol. 23, no. 21, p. 213001, 2011.

[15] H. Hedayat, C. Sayers, D. Bugini, C. Dallera, T. Batten, S. Karbassi, S. Friedmann, G. Cerullo, J. van Wezel, S. R. Clark, E. Carpene, and E. Da Como, "Phonon bottleneck in the recovery of 1T-$TiSe_2$ excitonic charge density waves," *In preparation.*

[16] B. A. Bernevig and S.-C. Zhang, "Quantum Spin Hall Effect," *Phys. Rev. Lett.*, vol. 96, p. 106802, Mar 2006.

[17] X.-L. Qi and S.-C. Zhang, "Topological insulators and superconductors," *Rev. Mod. Phys.*, vol. 83, pp. 1057–1110, Oct 2011.

[18] J. J. Sakurai and J. Napolitano, *Modern quantum mechanics*. Addison-Wesley, 2011.

[19] T. Zhang, P. Cheng, X. Chen, J.-F. Jia, X. Ma, K. He, L. Wang, H. Zhang, X. Dai, Z. Fang, X. Xie, and Q.-K. Xue, "Experimental Demonstration of Topological Surface States Protected by Time-Reversal Symmetry," *Phys. Rev. Lett.*, vol. 103, p. 266803, Dec 2009.

[20] M. J. Klein, "On a degeneracy theorem of kramers," *American Journal of Physics*, vol. 20, no. 2, pp. 65–71, 1952.

[21] J. E. Moore, "Chapter 2 - Theory of Three-Dimensional Topological Insulators," in *Topological Insulators* (M. Franz and L. Molenkamp, eds.), vol. 6 of *Contemporary Concepts of Condensed Matter Science*, pp. 35 – 57, Elsevier, 2013.

[22] L. Fu, "Hexagonal warping effects in the surface states of the topological insulator Bi_2Te_3," *Phys. Rev. Lett.*, vol. 103, p. 266801, Dec 2009.

[23] W.-C. Lee, C. Wu, D. P. Arovas, and S.-C. Zhang, "Quasiparticle interference on the surface of the topological insulator Bi_2Te_3," *Phys. Rev. B*, vol. 80, p. 245439, Dec 2009.

[24] X. Zhou, C. Fang, W.-F. Tsai, and J. Hu, "Theory of quasiparticle scattering in a two-dimensional system of helical Dirac fermions: Surface band structure of a three-dimensional topological insulator," *Phys. Rev. B*, vol. 80, p. 245317, Dec 2009.

[25] S. Souma, K. Kosaka, T. Sato, M. Komatsu, A. Takayama, T. Takahashi, M. Kriener, K. Segawa, and Y. Ando, "Direct measurement of the Out-of-Plane Spin Texture in the Dirac-Cone Surface State of a Topological Insulator," *Phys. Rev. Lett.*, vol. 106, p. 216803, May 2011.

[26] Y. Xia, D. Qian, D. Hsieh, L. Wray, A. Pal, H. Lin, A. Bansil, D. Grander, Y. S. Hor, R. J. Cava, and M. Z. Hasan, "Observation of a large-gap topological-insulator class with a single Dirac cone on the surface," *Nature Physycs*, vol. 5, pp. 398–402, 2009.

[27] D. Hsieh, Y. Xia, D. Qian, L. Wray, J. Dil, F. Meier, J. Osterwalder, L. Patthey, J. Checkelsky, N. Ong, *et al.*, "A tunable topological insulator in the spin helical Dirac transport regime," *Nature*, vol. 460, no. 7259, p. 1101, 2009.

[28] T. Arakane, T. Sato, S. Souma, K. Kosaka, K. Nakayama, M. Komatsu, T. Takahashi, Z. Ren, K. Segawa, and Y. Ando, "Tunable Dirac cone in the topological insulator $Bi_{2-x}Sb_xTe_{3-y}$ Se_y," *Nature communications*, vol. 3, p. 636, 2012.

[29] S. Souma, K. Kosaka, T. Sato, M. Komatsu, A. Takayama, T. Takahashi, M. Kriener, K. Segawa, and Y. Ando, "Direct measurement of the Out-of-Plane Spin Texture in the Dirac-Cone Surface State of a Topological Insulator," *Phys. Rev. Lett.*, vol. 106, p. 216803, May 2011.

[30] H. Zhang, C.-X. Liu, X.-L. Qi, X. Dai, Z. Fang, and S.-C. Zhang, "Topological insulators in Bi_2Se_3, Bi_2Te_3 and Sb_2Te_3 with a single dirac cone on the surface," *Nature Physics*, vol. 5, pp. 438–442, 2009.

[31] Y. Cao, J. Waugh, X. Zhang, J.-W. Luo, Q. Wang, T. Reber, S. Mo, Z. Xu, A. Yang, J. Schneeloch, *et al.*, "Mapping the orbital wavefunction of the surface states in three-dimensional topological insulators," *Nature Physics*, vol. 9, no. 8, pp. 499–504, 2013.

[32] Z.-H. Zhu, C. N. Veenstra, G. Levy, A. Ubaldini, P. Syers, N. P. Butch, J. Paglione, M. W. Haverkort, I. S. Elfimov, and A. Damascelli, "Layer-By-Layer Entangled Spin-Orbital Texture of the Topological Surface State in Bi_2Se_3," *Phys. Rev. Lett.*, vol. 110, p. 216401, May 2013.

[33] A. Sterzi, G. Manzoni, A. Crepaldi, F. Cilento, M. Zacchigna, M. Leclerc, P. Bugnon, A. Magrez, H. Berger, L. Petaccia, *et al.*, "Probing band parity inversion in the topological insulator $GeBi_2Te_4$ by linear dichroism in ARPES," *Journal of Electron Spectroscopy and Related Phenomena*, 2018.

[34] L. A. Wray, S.-Y. Xu, Y. Xia, D. Hsieh, A. V. Fedorov, Y. San Hor, R. J. Cava, A. Bansil, H. Lin, and M. Z. Hasan, "A topological insulator surface under strong Coulomb, magnetic and disorder perturbations," *Nature Physics*, vol. 7, no. 1, pp. 32–37, 2011.

[35] Z.-H. Zhu, G. Levy, B. Ludbrook, C. N. Veenstra, J. A. Rosen, R. Comin, D. Wong, P. Dosanjh, A. Ubaldini, P. Syers, N. P. Butch, J. Paglione, I. S. Elfimov, and A. Damascelli, "Rashba Spin-Splitting Control at the Surface of the Topological Insulator Bi_2Se_3," *Phys. Rev. Lett.*, vol. 107, p. 186405, Oct 2011.

[36] C. Chen, S. He, H. Weng, W. Zhang, L. Zhao, H. Liu, X. Jia, D. Mou, S. Liu, J. He, *et al.*, "Robustness of topological order and formation of

quantum well states in topological insulators exposed to ambient environment," *Proceedings of the National Academy of Sciences*, vol. 109, no. 10, pp. 3694–3698, 2012.

[37] Y. Chen, J.-H. Chu, J. Analytis, Z. Liu, K. Igarashi, H.-H. Kuo, X. Qi, S.-K. Mo, R. Moore, D. Lu, *et al.*, "Massive Dirac fermion on the surface of a magnetically doped topological insulator," *Science*, vol. 329, no. 5992, pp. 659–662, 2010.

[38] M. R. Scholz, J. Sánchez-Barriga, D. Marchenko, A. Varykhalov, A. Volykhov, L. V. Yashina, and O. Rader, "Tolerance of Topological Surface States towards Magnetic Moments: Fe on Bi_2Se_3," *Phys. Rev. Lett.*, vol. 108, p. 256810, Jun 2012.

[39] I. Vobornik, G. Panaccione, J. Fujii, Z.-H. Zhu, F. Offi, B. R. Salles, F. Borgatti, P. Torelli, J. P. Rueff, D. Ceolin, *et al.*, "Observation of distinct bulk and surface chemical environments in a topological insulator under magnetic doping," *The Journal of Physical Chemistry C*, vol. 118, no. 23, pp. 12333–12339, 2014.

[40] Y. S. Hor, A. J. Williams, J. G. Checkelsky, P. Roushan, J. Seo, Q. Xu, H. W. Zandbergen, A. Yazdani, N. P. Ong, and R. J. Cava, "Superconductivity in $Cu_xBi_2Se_3$ and its implications for pairing in the undoped topological insulator," *Phys. Rev. Lett.*, vol. 104, p. 057001, Feb 2010.

[41] M. Kriener, K. Segawa, Z. Ren, S. Sasaki, and Y. Ando, "Bulk superconducting phase with a full energy gap in the doped topological insulator $Cu_xBi_2Se_3$," *Phys. Rev. Lett.*, vol. 106, p. 127004, Mar 2011.

[42] J. L. Zhang, S. J. Zhang, H. M. Weng, W. Zhang, L. X. Yang, Q. Q. Liu, S. M. Feng, X. C. Wang, R. C. Yu, L. Z. Cao, L. Wang, W. G. Yang, H. Z. Liu, W. Y. Zhao, S. C. Zhang, X. Dai, Z. Fang, and C. Q. Jin, "Pressure-induced superconductivity in topological parent compound Bi_2Te_3," *Proceedings of the National Academy of Sciences*, vol. 108, no. 1, pp. 24–28, 2011.

[43] Z.-H. Pan, A. V. Fedorov, D. Gardner, Y. S. Lee, S. Chu, and T. Valla, "Measurement of an exceptionally weak electron-phonon coupling on the surface of the topological insulator Bi_2Se_3 using angle-resolved photoemission spectroscopy," *Phys. Rev. Lett.*, vol. 108, p. 187001, May 2012.

[44] Z. Ren, A. A. Taskin, S. Sasaki, K. Segawa, and Y. Ando, "Large bulk resistivity and surface quantum oscillations in the topological insulator Bi_2Te_2Se," *Phys. Rev. B*, vol. 82, p. 241306, Dec 2010.

[45] M. R. Scholz, J. Sánchez-Barriga, J. Braun, D. Marchenko, A. Varykhalov, M. Lindroos, Y. J. Wang, H. Lin, A. Bansil, J. Minár, H. Ebert, A. Volykhov, L. V. Yashina, and O. Rader, "Reversal of the circular dichroism in angle-resolved photoemission from Bi_2Te_3," *Phys. Rev. Lett.*, vol. 110, p. 216801, May 2013.

[46] F. Vidal, M. Eddrief, B. Rache Salles, I. Vobornik, E. Velez-Fort, G. Panaccione, and M. Marangolo, "Photon energy dependence of circular dichroism in angle-resolved photoemission spectroscopy of Bi_2Se_3 dirac states," *Phys. Rev. B*, vol. 88, p. 241410, Dec 2013.

[47] S. R. Park, J. Han, C. Kim, Y. Y. Koh, C. Kim, H. Lee, H. J. Choi, J. H. Han, K. D. Lee, N. J. Hur, M. Arita, K. Shimada, H. Namatame, and M. Taniguchi, "Chiral orbital-angular momentum in the surface states of Bi_2Se_3," *Phys. Rev. Lett.*, vol. 108, p. 046805, Jan 2012.

[48] J. Sánchez-Barriga, A. Varykhalov, J. Braun, S.-Y. Xu, N. Alidoust, O. Kornilov, J. Minár, K. Hummer, G. Springholz, G. Bauer, R. Schumann, V. Yashina, L. H. Ebert, Z. Hasan, M. and O. Rader, "Photoemission of Bi_2Se_3 with circularly polarized light: Probe of spin polarization or means for spin manipulation?," *Phys. Rev. X*, vol. 4, p. 011046, Mar 2014.

[49] Y. H. Wang, D. Hsieh, D. Pilon, L. Fu, D. R. Gardner, Y. S. Lee, and N. Gedik, "Observation of a warped helical spin texture in Bi_2Se_3 from circular dichroism angle-resolved photoemission spectroscopy," *Phys. Rev. Lett.*, vol. 107, p. 207602, Nov 2011.

[50] M. Neupane, S. Basak, N. Alidoust, S.-Y. Xu, C. Liu, I. Belopolski, G. Bian, J. Xiong, H. Ji, S. Jia, S.-K. Mo, M. Bissen, M. Severson, H. Lin, N. P. Ong, T. Durakiewicz, R. J. Cava, A. Bansil, and M. Z. Hasan, "Oscillatory surface dichroism of the insulating topological insulator Bi_2Te_2Se," *Phys. Rev. B*, vol. 88, p. 165129, Oct 2013.

[51] A. Crepaldi, F. Cilento, M. Zacchigna, M. Zonno, J. C. Johannsen, C. Tournier-Colletta, L. Moreschini, I. Vobornik, F. Bondino, E. Magnano, H. Berger, A. Magrez, P. Bugnon, G. Autès, O. V. Yazyev,

M. Grioni, and F. Parmigiani, "Momentum and photon energy dependence of the circular dichroic photoemission in the bulk rashba semiconductors BiTeX (X=I, Br, Cl)," *Phys. Rev. B*, vol. 89, p. 125408, Mar 2014.

[52] M. Mulazzi, G. Rossi, J. Braun, J. Minár, H. Ebert, G. Panaccione, I. Vobornik, and J. Fujii, "Understanding intensities of angle-resolved photoemission with circularly polarized radiation from a Cu(111) surface state," *Phys. Rev. B*, vol. 79, p. 165421, Apr 2009.

[53] H. Mirhosseini and J. Henk, "Spin texture and circular dichroism in photoelectron spectroscopy from the topological insulator Bi_2Te_3: First-principles photoemission calculations," *Physical review letters*, vol. 109, no. 3, p. 036803, 2012.

[54] J. A. Sobota, S. Yang, J. G. Analytis, Y. L. Chen, I. R. Fisher, P. S. Kirchmann, and Z.-X. Shen, "Ultrafast optical excitation of a persistent surface-state population in the topological insulator Bi_2Se_3," *Phys. Rev. Lett.*, vol. 108, p. 117403, Mar 2012.

[55] U. Höfer, I. Shumay, C. Reuß, U. Thomann, W. Wallauer, and T. Fauster, "Time-resolved coherent photoelectron spectroscopy of quantized electronic states on metal surfaces," *Science*, vol. 277, no. 5331, pp. 1480–1482, 1997.

[56] A. Crepaldi, F. Cilento, B. Ressel, C. Cacho, J. Johannsen, M. Zacchigna, H. Berger, P. Bugnon, C. Grazioli, I. Turcu, *et al.*, "Evidence of reduced surface electron-phonon scattering in the conduction band of Bi_2Se_3 by nonequilibrium ARPES," *Physical Review B*, vol. 88, no. 12, p. 121404, 2013.

[57] M. Hajlaoui, E. Papalazarou, J. Mauchain, L. Perfetti, A. Taleb-Ibrahimi, F. Navarin, M. Monteverde, P. Auban-Senzier, C. Pasquier, N. Moisan, *et al.*, "Tuning a Schottky barrier in a photoexcited topological insulator with transient Dirac cone electron-hole asymmetry," *Nature communications*, vol. 5, 2014.

[58] M. Hajlaoui, E. Papalazarou, J. Mauchain, G. Lantz, N. Moisan, D. Boschetto, Z. Jiang, I. Miotkowski, Y. Chen, A. Taleb-Ibrahimi, *et al.*, "Ultrafast surface carrier dynamics in the topological insulator Bi_2Te_3," *Nano letters*, vol. 12, no. 7, pp. 3532–3536, 2012.

[59] A. Crepaldi, B. Ressel, F. Cilento, M. Zacchigna, C. Grazioli, H. Berger, P. Bugnon, K. Kern, M. Grioni, and F. Parmigiani, "Ultrafast

photodoping and effective fermi-dirac distribution of the dirac particles in Bi_2Se_3," *Phys. Rev. B*, vol. 86, p. 205133, Nov 2012.

[60] M. Neupane, S.-Y. Xu, Y. Ishida, S. Jia, B. M. Fregoso, C. Liu, I. Belopolski, G. Bian, N. Alidoust, T. Durakiewicz, *et al.*, "Gigantic surface lifetime of an intrinsic topological insulator," *Physical review letters*, vol. 115, no. 11, p. 116801, 2015.

[61] A. Sterzi, G. Manzoni, L. Sbuelz, F. Cilento, M. Zacchigna, P. Bugnon, A. Magrez, H. Berger, A. Crepaldi, and F. Parmigiani, "Bulk diffusive relaxation mechanisms in optically excited topological insulators," *Phys. Rev. B*, vol. 95, p. 115431, Mar 2017.

[62] S. Zhu, Y. Ishida, K. Kuroda, K. Sumida, M. Ye, J. Wang, H. Pan, M. Taniguchi, S. Qiao, S. Shin, *et al.*, "Ultrafast electron dynamics at the dirac node of the topological insulator Sb_2Te_3," *Scientific reports*, vol. 5, p. 13213, 2015.

[63] J. A. Sobota, S.-L. Yang, A. F. Kemper, J. J. Lee, F. T. Schmitt, W. Li, R. G. Moore, J. G. Analytis, I. R. Fisher, P. S. Kirchmann, T. P. Devereaux, and Z.-X. Shen, "Direct optical coupling to an unoccupied dirac surface state in the topological insulator Bi_2Se_3," *Phys. Rev. Lett.*, vol. 111, p. 136802, Sep 2013.

[64] D. Niesner, T. Fauster, S. V. Eremeev, T. V. Menshchikova, Y. M. Koroteev, A. P. Protogenov, E. V. Chulkov, O. E. Tereshchenko, K. A. Kokh, O. Alekperov, A. Nadjafov, and N. Mamedov, "Unoccupied topological states on bismuth chalcogenides," *Phys. Rev. B*, vol. 86, p. 205403, Nov 2012.

[65] D. Niesner, S. Otto, T. Fauster, E. Chulkov, S. Eremeev, O. Tereshchenko, and K. Kokh, "Electron dynamics of unoccupied states in topological insulators," *Journal of Electron Spectroscopy and Related Phenomena*, vol. 195, pp. 258–262, 2014.

[66] C. Jozwiak, J. A. Sobota, K. Gotlieb, A. F. Kemper, C. R. Rotundu, R. J. Birgeneau, Z. Hussain, D.-H. Lee, Z.-X. Shen, and A. Lanzara, "Spin-polarized surface resonances accompanying topological surface state formation," *Nature communications*, vol. 7, p. 13143, 2016.

[67] D. Hsieh, F. Mahmood, J. W. McIver, D. R. Gardner, Y. S. Lee, and N. Gedik, "Selective probing of photoinduced charge and spin dynamics in the bulk and surface of a topological insulator," *Phys. Rev. Lett.*, vol. 107, p. 077401, Aug 2011.

[68] C. Kastl, C. Karnetzky, H. Karl, and A. W. Holleitner, "Ultrafast helicity control of surface currents in topological insulators with near-unity fidelity," *Nature communications*, vol. 6, p. 6617, 2015.

[69] F. Boschini, M. Mansurova, G. Mussler, J. Kampmeier, D. Grützmacher, L. Braun, F. Katmis, J. Moodera, C. Dallera, E. Carpene, *et al.*, "Coherent ultrafast spin-dynamics probed in three dimensional topological insulators," *Scientific reports*, vol. 5, p. 15304, 2015.

[70] M. C. Wang, S. Qiao, Z. Jiang, S. N. Luo, and J. Qi, "Unraveling photoinduced spin dynamics in the topological insulator Bi_2Se_3," *Phys. Rev. Lett.*, vol. 116, p. 036601, Jan 2016.

[71] S. Y. Hamh, S.-H. Park, S.-K. Jerng, J. H. Jeon, S.-H. Chun, and J. S. Lee, "Helicity-dependent photocurrent in a Bi_2Se_3 thin film probed by terahertz emission spectroscopy," *Phys. Rev. B*, vol. 94, p. 161405, Oct 2016.

[72] A. Shikin, I. Klimovskikh, M. Filyanina, A. Rybkina, D. Pudikov, K. Kokh, and O. Tereshchenko, "Surface spin-polarized currents generated in topological insulators by circularly polarized synchrotron radiation and their photoelectron spectroscopy indication," *Physics of the Solid State*, vol. 58, no. 8, pp. 1675–1686, 2016.

[73] V. Kaladzhyan, P. P. Aseev, and S. N. Artemenko, "Photogalvanic effect in the HgTe/CdTe topological insulator due to edge-bulk optical transitions," *Phys. Rev. B*, vol. 92, p. 155424, Oct 2015.

[74] P. Hosur, "Circular photogalvanic effect on topological insulator surfaces: Berry-curvature-dependent response," *Phys. Rev. B*, vol. 83, p. 035309, Jan 2011.

[75] J. Reimann, J. Güdde, K. Kuroda, E. V. Chulkov, and U. Höfer, "Spectroscopy and dynamics of unoccupied electronic states of the topological insulators Sb_2Te_3 and Sb_2Te_2S," *Phys. Rev. B*, vol. 90, p. 081106, Aug 2014.

[76] K. Kuroda, J. Reimann, J. Güdde, and U. Höfer, "Generation of transient photocurrents in the topological surface state of Sb_2Te_3 by direct optical excitation with midinfrared pulses," *Phys. Rev. Lett.*, vol. 116, p. 076801, Feb 2016.

[77] C. Cacho, A. Crepaldi, M. Battiato, J. Braun, F. Cilento, M. Zacchigna, M. C. Richter, O. Heckmann, E. Springate, Y. Liu, S. S. Dhesi,

H. Berger, P. Bugnon, K. Held, M. Grioni, H. Ebert, K. Hricovini, J. Minár, and F. Parmigiani, "Momentum-resolved spin dynamics of bulk and surface excited states in the topological insulator Bi_2Se_3," *Phys. Rev. Lett.*, vol. 114, p. 097401, Mar 2015.

[78] J. Sánchez-Barriga, M. Battiato, M. Krivenkov, E. Golias, A. Varykhalov, A. Romualdi, L. Yashina, J. Minár, O. Kornilov, H. Ebert, *et al.*, "Subpicosecond spin dynamics of excited states in the topological insulator Bi_2Te_3," *Physical Review B*, vol. 95, no. 12, p. 125405, 2017.

[79] G. Gruner, *Density waves in solids*. CRC Press, 2018.

[80] R. E. Peierls and R. S. Peierls, *Quantum theory of solids*. Oxford University Press, 1955.

[81] F. R. S. Fröhlich, "On the theory of superconductivity: the one-dimensional case," *Proceedings of the Royal Society of London A: Mathematical, Physical and Engineering Sciences*, vol. 223, no. 1154, pp. 296–305, 1954.

[82] T. Riste, *Electron-phonon interactions and phase transitions*, vol. 29. Springer Science & Business Media, 2013.

[83] S.-K. Chan and V. Heine, "Spin density wave and soft phonon mode from nesting Fermi surfaces," *Journal of Physics F: Metal Physics*, vol. 3, no. 4, p. 795, 1973.

[84] M. D. Johannes and I. I. Mazin, "Fermi surface nesting and the origin of charge density waves in metals," *Phys. Rev. B*, vol. 77, p. 165135, Apr 2008.

[85] V. Brouet, W. L. Yang, X. J. Zhou, Z. Hussain, N. Ru, K. Y. Shin, I. R. Fisher, and Z. X. Shen, "Fermi surface reconstruction in the CDW state of $CeTe_3$ observed by photoemission," *Phys. Rev. Lett.*, vol. 93, p. 126405, Sep 2004.

[86] V. Brouet, W. L. Yang, X. J. Zhou, Z. Hussain, R. G. Moore, R. He, D. H. Lu, Z. X. Shen, J. Laverock, S. B. Dugdale, N. Ru, and I. R. Fisher, "Angle-resolved photoemission study of the evolution of band structure and charge density wave properties in RTe_3 (R=Y, La, Ce, Sm, Gd, Tb, and Dy)," *Phys. Rev. B*, vol. 77, p. 235104, Jun 2008.

[87] S. B. Dugdale, "Life on the edge: a beginners guide to the fermi surface," *Physica Scripta*, vol. 91, no. 5, p. 053009, 2016.

[88] L. D. Landau and E. M. Lifshitz, *Statistical physics: V. 5: course of theoretical physics*. Pergamon press, 1968.

[89] N. D. Mermin and H. Wagner, "Absence of ferromagnetism or antiferromagnetism in one- or two-dimensional isotropic heisenberg models," *Phys. Rev. Lett.*, vol. 17, pp. 1133–1136, Nov 1966.

[90] P. A. Lee, T. M. Rice, and P. W. Anderson, "Fluctuation effects at a Peierls transition," *Phys. Rev. Lett.*, vol. 31, pp. 462–465, Aug 1973.

[91] M. Rice and S. Strässler, "Theory of a quasi-one-dimensional band-conductor," *Solid State Communications*, vol. 13, no. 1, pp. 125–128, 1973.

[92] D. Allender, J. W. Bray, and J. Bardeen, "Theory of fluctuation superconductivity from electron-phonon interactions in pseudo-one-dimensional systems," *Phys. Rev. B*, vol. 9, pp. 119–129, Jan 1974.

[93] J. Kröger, "Electron–phonon coupling at metal surfaces," *Reports on Progress in Physics*, vol. 69, no. 4, p. 899, 2006.

[94] M. Tinkham, *Introduction to superconductivity*. Courier Corporation, 1996.

[95] J.-P. Pouget, "Aspects de la physique des conducteurs quasi-unidimensionnels," 1995.

[96] K. Motizuki, *Structural phase transitions in layered transition metal compounds*, vol. 8. Springer Science & Business Media, 2012.

[97] N. Doran, D. Titterington, B. Ricco, M. Schreiber, and G. Wexler, "The electronic susceptibility and charge density waves in 2H layer compounds," *Journal of Physics C: Solid State Physics*, vol. 11, no. 4, p. 699, 1978.

[98] W. L. McMillan, "Microscopic model of charge-density waves in 2H-$TaSe_2$," *Phys. Rev. B*, vol. 16, pp. 643–650, Jul 1977.

[99] C. Haas, "Chemical bond model of lattice distortions in hexagonal layers," *Solid State Communications*, vol. 26, no. 11, pp. 709–712, 1978.

[100] J. Inglesfield, "Bonding and charge density wave phase transitions," *Physica B+ C*, vol. 99, no. 1-4, pp. 238–242, 1980.

[101] H. Hughes, "Structural distortion in $TiSe_2$ and related materials-a possible Jahn-Teller effect?," *Journal of Physics C: Solid State Physics*, vol. 10, no. 11, p. L319, 1977.

[102] M. H. Whangbo and E. Canadell, "Analogies between the concepts of molecular chemistry and solid-state physics concerning structural instabilities. electronic origin of the structural modulations in layered transition metal dichalcogenides," *Journal of the American Chemical Society*, vol. 114, no. 24, pp. 9587–9600, 1992.

[103] M. Holt, P. Zschack, H. Hong, M. Y. Chou, and T.-C. Chiang, "X-ray studies of phonon softening in $TiSe_2$," *Phys. Rev. Lett.*, vol. 86, pp. 3799–3802, Apr 2001.

[104] W. Kohn, "Many body physics," *Gordon and Breach, New York*, p. 351, 1968.

[105] B. I. Halperin and T. M. Rice, "Possible anomalies at a semimetal-semiconductor transistion," *Rev. Mod. Phys.*, vol. 40, pp. 755–766, Oct 1968.

[106] M. J. Rice and Y. N. Gartstein, "The excitonic ground state of the half-filled Peierls insulator," *Journal of Physics: Condensed Matter*, vol. 17, no. 29, p. 4615, 2005.

[107] T. Rohwer, S. Hellmann, M. Wiesenmayer, C. Sohrt, A. Stange, B. Slomski, A. Carr, Y. Liu, L. M. Avila, M. Kalläne, *et al.*, "Collapse of long-range charge order tracked by time-resolved photoemission at high momenta," *Nature*, vol. 471, no. 7339, p. 490, 2011.

[108] K. Rossnagel, L. Kipp, and M. Skibowski, "Charge-density-wave phase transition in 1T-$TiSe_2$: Excitonic insulator versus band-type Jahn-Teller mechanism," *Physical Review B*, vol. 65, no. 23, p. 235101, 2002.

[109] E. Morosan, H. W. Zandbergen, B. Dennis, J. Bos, Y. Onose, T. Klimczuk, A. Ramirez, N. Ong, and R. J. Cava, "Superconductivity in Cu_xTiSe_2," *Nature Physics*, vol. 2, no. 8, p. 544, 2006.

[110] A. F. Kusmartseva, B. Sipos, H. Berger, L. Forró, and E. Tutiš, "Pressure induced superconductivity in pristine 1T-$TiSe_2$," *Phys. Rev. Lett.*, vol. 103, p. 236401, Nov 2009.

[111] Y. I. Joe, X. Chen, P. Ghaemi, K. Finkelstein, G. de La Peña, Y. Gan, J. Lee, S. Yuan, J. Geck, G. MacDougall, *et al.*, "Emergence of charge density wave domain walls above the superconducting dome in 1T-$TiSe_2$," *Nature Physics*, vol. 10, no. 6, pp. 421–425, 2014.

[112] H. Cercellier, C. Monney, F. Clerc, C. Battaglia, L. Despont, M. G. Garnier, H. Beck, P. Aebi, L. Patthey, H. Berger, and L. Forró, "Evidence for an excitonic insulator phase in 1T-$TiSe_2$," *Phys. Rev. Lett.*, vol. 99, p. 146403, Oct 2007.

[113] T. E. Kidd, T. Miller, M. Y. Chou, and T.-C. Chiang, "Electron-hole coupling and the charge density wave transition in $TiSe_2$," *Phys. Rev. Lett.*, vol. 88, p. 226402, May 2002.

[114] J. F. Zhao, H. W. Ou, G. Wu, B. P. Xie, Y. Zhang, D. W. Shen, J. Wei, L. X. Yang, J. K. Dong, M. Arita, H. Namatame, M. Taniguchi, X. H. Chen, and D. L. Feng, "Evolution of the electronic structure of 1T-Cu_xTiSe_2," *Phys. Rev. Lett.*, vol. 99, p. 146401, Oct 2007.

[115] J. C. E. Rasch, T. Stemmler, B. Müller, L. Dudy, and R. Manzke, "1T-$TiSe_2$: Semimetal or semiconductor?," *Phys. Rev. Lett.*, vol. 101, p. 237602, Dec 2008.

[116] J. van Wezel, P. Nahai-Williamson, and S. S. Saxena, "An alternative interpretation of recent ARPES measurements on $TiSe_2$," *EPL (Europhysics Letters)*, vol. 89, no. 4, p. 47004, 2010.

[117] C. Monney, H. Cercellier, F. Clerc, C. Battaglia, E. F. Schwier, C. Didiot, M. G. Garnier, H. Beck, P. Aebi, H. Berger, L. Forró, and L. Patthey, "Spontaneous exciton condensation in 1T-$TiSe_2$: BCS-like approach," *Phys. Rev. B*, vol. 79, p. 045116, Jan 2009.

[118] J. Voit, L. Perfetti, F. Zwick, H. Berger, G. Margaritondo, G. Grüner, H. Höchst, and M. Grioni, "Electronic structure of solids with competing periodic potentials," *Science*, vol. 290, no. 5491, pp. 501–503, 2000.

[119] J. van Wezel, P. Nahai-Williamson, and S. S. Saxena, "Exciton-phonon interactions and superconductivity bordering charge order in $TiSe_2$," *Phys. Rev. B*, vol. 83, p. 024502, Jan 2011.

[120] C. Monney, E. Schwier, M. G. Garnier, N. Mariotti, C. Didiot, H. Beck, P. Aebi, H. Cercellier, J. Marcus, C. Battaglia, *et al.*, "Temperature-dependent photoemission on 1T-$TiSe_2$: Interpretation within the ex-

citon condensate phase model," *Physical Review B*, vol. 81, no. 15, p. 155104, 2010.

[121] B. Hildebrand, T. Jaouen, C. Didiot, E. Razzoli, G. Monney, M.-L. Mottas, A. Ubaldini, H. Berger, C. Barreteau, H. Beck, D. R. Bowler, and P. Aebi, "Short-range phase coherence and origin of the 1T-$TiSe_2$ charge density wave," *Phys. Rev. B*, vol. 93, p. 125140, Mar 2016.

[122] S. Hellmann, T. Rohwer, M. Kalläne, K. Hanff, C. Sohrt, A. Stange, A. Carr, M. Murnane, H. Kapteyn, L. Kipp, *et al.*, "Time-domain classification of charge-density-wave insulators," *Nature communications*, vol. 3, p. 1069, 2012.

[123] C. Giannetti, M. Capone, D. Fausti, M. Fabrizio, F. Parmigiani, and D. Mihailovic, "Ultrafast optical spectroscopy of strongly correlated materials and high-temperature superconductors: a non-equilibrium approach," *Advances in Physics*, vol. 65, no. 2, pp. 58–238, 2016.

[124] S. Sundaram and E. Mazur, "Inducing and probing non-thermal transitions in semiconductors using femtosecond laser pulses," *Nature materials*, vol. 1, no. 4, p. 217, 2002.

[125] M. Porer, U. Leierseder, J.-M. Ménard, H. Dachraoui, L. Mouchliadis, I. Perakis, U. Heinzmann, J. Demsar, K. Rossnagel, and R. Huber, "Non-thermal separation of electronic and structural orders in a persisting charge density wave," *Nature materials*, vol. 13, no. 9, p. 857, 2014.

[126] C. Monney, M. Puppin, C. W. Nicholson, M. Hoesch, R. T. Chapman, E. Springate, H. Berger, A. Magrez, C. Cacho, R. Ernstorfer, and M. Wolf, "Revealing the role of electrons and phonons in the ultrafast recovery of charge density wave correlations in 1T-$TiSe_2$," *Phys. Rev. B*, vol. 94, p. 165165, Oct 2016.

[127] A. Einstein, "Über einen die erzeugung und verwandlung des lichtes betreffenden heuristischen gesichtspunkt," *Annalen der physik*, vol. 322, no. 6, pp. 132–148, 1905.

[128] K. Roßnagel, L. Kipp, and M. Skibowski, "Angle-resolved photoelectron spectroscopy: From photoemission imaging to spatial resolution," *Solid-State Photoemission and Related Methods: Theory and Experiment*, pp. 159–176, 2003.

[129] A. Damascelli, "Probing the electronic structure of complex systems by ARPES," *Physica Scripta*, vol. 2004, no. T109, p. 61, 2004.

[130] J. Braun, "The theory of angle-resolved ultraviolet photoemission and its applications to ordered materials," *Reports on Progress in Physics*, vol. 59, no. 10, p. 1267, 1996.

[131] T. Giamarchi, A. Iucci, and C. Berthod, "Introduction to many body physics," *Lecture Notes, University of Geneva (2008-2009)*, 2008.

[132] A. L. Fetter and J. D. Walecka, *Quantum theory of many-particle systems*. Courier Corporation, 2003.

[133] W. Schattke, M. Van Hove, F. de Abajo, R. D. Muiño, and N. Mannella, "Overview of core and valence photoemission," *Solid-State Photoemission and Related Methods: Theory and Experiment*, pp. 50–115.

[134] T. Valla, A. V. Fedorov, P. D. Johnson, B. O. Wells, S. L. Hulbert, Q. Li, G. D. Gu, and N. Koshizuka, "Evidence for quantum critical behavior in the optimally doped cuprate Bi_2 Sr_2 $CaCu_2$ $O_{8+\delta}$," *Science*, vol. 285, no. 5436, pp. 2110–2113, 1999.

[135] J. Stöhr, R. Jaeger, and J. J. Rehr, "Transition from adiabatic to sudden core-electron excitation: N_2 on Ni(100)," *Phys. Rev. Lett.*, vol. 51, pp. 821–824, Aug 1983.

[136] J. D. Koralek, J. F. Douglas, N. C. Plumb, Z. Sun, A. V. Fedorov, M. M. Murnane, H. C. Kapteyn, S. T. Cundiff, Y. Aiura, K. Oka, H. Eisaki, and D. S. Dessau, "Laser based angle-resolved photoemission, the sudden approximation, and quasiparticle-like spectral peaks in $Bi_2Sr_2CaCu_2O_{8+\delta}$," *Phys. Rev. Lett.*, vol. 96, p. 017005, Jan 2006.

[137] E. Beaurepaire, J.-C. Merle, A. Daunois, and J.-Y. Bigot, "Ultrafast spin dynamics in ferromagnetic nickel," *Phys. Rev. Lett.*, vol. 76, pp. 4250–4253, May 1996.

[138] E. Carpene, E. Mancini, C. Dallera, M. Brenna, E. Puppin, and S. De Silvestri, "Dynamics of electron-magnon interaction and ultrafast demagnetization in thin iron films," *Phys. Rev. B*, vol. 78, p. 174422, Nov 2008.

[139] J. K. Freericks, H. R. Krishnamurthy, and T. Pruschke, "Theoretical description of time-resolved photoemission spectroscopy: Application to pump-probe experiments," *Phys. Rev. Lett.*, vol. 102, p. 136401, Mar 2009.

[140] C. L. Smallwood, C. Jozwiak, W. Zhang, and A. Lanzara, "An ultrafast angle-resolved photoemission apparatus for measuring complex materials," *Review of Scientific Instruments*, vol. 83, no. 12, 2012.

[141] J. Faure, J. Mandchain, E. Papalazarou, W. Yan, J. Pinon, M. Marsi, and L. Perfetti, "Full characterization and optimization of a femtosecond ultraviolet laser source for time and angle-resolved photoemission on solid surfaces," *Review of Scientific Instruments*, vol. 83, no. 4, 2012.

[142] P. Siffalovic, M. Drescher, M. Spieweck, T. Wiesenthal, Y. C. Lim, R. Weidner, A. Elizarov, and U. Heinzmann, "Laser-based apparatus for extended ultraviolet femtosecond time-resolved photoemission spectroscopy," *Review of Scientific Instruments*, vol. 72, no. 1, pp. 30–35, 2001.

[143] G. L. Dakovski, Y. Li, T. Durakiewicz, and G. Rodriguez, "Tunable ultrafast extreme ultraviolet source for time- and angle-resolved photoemission spectroscopy," *Review of Scientific Instruments*, vol. 81, no. 7, 2010.

[144] P. Wernet, J. Ganddin, K. Godehusen, O. Schwarzkopf, and W. Eberhardt, "Femtosecond time-resolved photoelectron spectroscopy with a vacuum-ultraviolet photon source based on laser high-order harmonic generation," *Review of Scientific Instruments*, vol. 82, no. 6, 2011.

[145] J. Ojeda, C. Arrell, J. Grilj, F. Frassetto, L. Mewes, H. Zhang, F. Van Mourik, L. Poletto, and M. Chergui, "Harmonium: A pulse preserving source of monochromatic extreme ultraviolet (30–110 eV) radiation for ultrafast photoelectron spectroscopy of liquids," *Structural Dynamics*, vol. 3, no. 2, p. 023602, 2016.

[146] A. Crepaldi, S. Roth, G. Gatti, C. A. Arrell, J. Ojeda, F. Van Mourik, P. Bugnon, A. Magrez, H. Berger, M. Chergui, *et al.*, "Time-resolved ARPES at LACUS: Band structure and ultrafast electron dynamics of solids," *CHIMIA International Journal for Chemistry*, vol. 71, no. 5, pp. 273–277, 2017.

[147] S. Hellmann, K. Rossnagel, M. Marczynski-Bühlow, and L. Kipp, "Vacuum space-charge effects in solid-state photoemission," *Phys. Rev. B*, vol. 79, p. 035402, Jan 2009.

[148] M. Puppin, Y. Deng, O. Prochnow, J. Ahrens, T. Binhammer, U. Morgner, M. Krenz, M. Wolf, and R. Ernstorfer, "500 kHz OPCPA

delivering tunable sub-20 fs pulses with 15 W average power based on an all-ytterbium laser," *Optics express*, vol. 23, no. 2, pp. 1491–1497, 2015.

[149] A. K. Mills, S. Zhdanovich, E. Rampi, R. Comin, G. Levy, A. Damascelli, and D. J. Jones, "Studying correlated electron systems with a new tunable 25 ev tabletop xuv source," in *CLEO: 2014*, p. FM4B.6, Optical Society of America, 2014.

[150] P. Miotti, F. Cilento, R. Cucini, A. D. Luisa, A. Fondacaro, F. Frassetto, D. Kopić, D. Payne, A. Sterzi, T. Pincelli, G. Panaccione, F. Parmigiani, G. Rossi, and L. Poletto, "A novel high order harmonic source for time- and angle-resolved photoemission experiments," in *High-Brightness Sources and Light-driven Interactions*, p. EW2B.5, Optical Society of America, 2018.

[151] F. Boschini, E. da Silva Neto, E. Razzoli, M. Zonno, S. Peli, R. Day, M. Michiardi, M. Schneider, B. Zwartsenberg, P. Nigge, *et al.*, "Collapse of superconductivity in cuprates via ultrafast quenching of phase coherence," *Nature materials*, vol. 17, p. 416, 2018.

[152] J. Braun, R. Randsch, M. Potthoff, J. Minár, and H. Ebert, "One-step theory of pump-probe photoemission," *Phys. Rev. B*, vol. 91, p. 035119, Jan 2015.

[153] S. Kushwaha, I. Pletikosić, T. Liang, A. Gyenis, S. Lapidus, Y. Tian, H. Zhao, K. Burch, J. Lin, W. Wang, *et al.*, "Sn-doped $Bi_{1.1}Sb_{0.9}Te_2s$ bulk crystal topological insulator with excellent properties," *Nature communications*, vol. 7, p. 11456, 2016.

[154] S. Dal Conte, L. Vidmar, D. Golež, M. Mierzejewski, G. Soavi, S. Peli, F. Banfi, G. Ferrini, R. Comin, B. M. Ludbrook, *et al.*, "Snapshots of the retarded interaction of charge carriers with ultrafast fluctuations in cuprates," *Nature Physics*, vol. 11, no. 5, p. 421, 2015.

[155] N. P. Butch, K. Kirshenbaum, P. Syers, A. B. Sushkov, G. S. Jenkins, H. D. Drew, and J. Paglione, "Strong surface scattering in ultrahigh-mobility Bi_2Se_3 topological insulator crystals," *Phys. Rev. B*, vol. 81, p. 241301, Jun 2010.

[156] M. Neupane, S.-Y. Xu, L. A. Wray, A. Petersen, R. Shankar, N. Alidoust, C. Liu, A. Fedorov, H. Ji, J. M. Allred, Y. S. Hor, T.-R. Chang,

H.-T. Jeng, H. Lin, A. Bansil, R. J. Cava, and M. Z. Hasan, "Topological surface states and Dirac point tuning in ternary topological insulators," *Phys. Rev. B*, vol. 85, p. 235406, Jun 2012.

[157] C. Chen, Z. Xie, Y. Feng, H. Yi, A. Liang, S. He, D. Mou, J. He, Y. Peng, X. Liu, *et al.*, "Tunable Dirac fermion dynamics in topological insulators," *Scientific reports*, vol. 3, p. 2411, 2013.

[158] R. Yoshimi, A. Tsukazaki, Y. Kozuka, J. Falson, K. Takahashi, J. Checkelsky, N. Nagaosa, M. Kawasaki, and Y. Tokura, "Quantum Hall effect on top and bottom surface states of topological insulator $(Bi_{1-x}Sb_x)_2Te_3$ films," *Nature communications*, vol. 6, p. 6627, 2015.

[159] B. Xia, P. Ren, A. Sulaev, P. Liu, S.-Q. Shen, and L. Wang, "Indications of surface-dominated transport in single crystalline nanoflake devices of topological insulator $Bi_{1.5}Sb_{0.5}Te_{1.8}Se_{1.2}$," *Phys. Rev. B*, vol. 87, p. 085442, Feb 2013.

[160] Y. Xu, I. Miotkowski, C. Liu, J. Tian, H. Nam, N. Alidoust, J. Hu, C.-K. Shih, M. Z. Hasan, and Y. P. Chen, "Observation of topological surface state quantum Hall effect in an intrinsic three-dimensional topological insulator," *Nature Physics*, vol. 10, no. 12, p. 956, 2014.

[161] K. Sumida, Y. Ishida, S. Zhu, M. Ye, A. Pertsova, C. Triola, K. A. Kokh, O. E. Tereshchenko, A. V. Balatsky, S. Shin, *et al.*, "Prolonged duration of nonequilibrated Dirac fermions in neutral topological insulators," *Scientific reports*, vol. 7, no. 1, p. 14080, 2017.

[162] P. Roushan, J. Seo, C. V. Parker, Y. S. Hor, D. Hsieh, D. Qian, A. Richardella, M. Z. Hasan, R. J. Cava, and A. Yazdani, "Topological surface states protected from backscattering by chiral spin texture," *Nature*, vol. 460, pp. 1106–1109, 2009.

[163] F. Meier and B. P. Zakharchenya, *Optical orientation*, vol. 8. Elsevier, 2012.

[164] J. Sánchez-Barriga, E. Golias, A. Varykhalov, J. Braun, L. V. Yashina, R. Schumann, J. Minár, H. Ebert, O. Kornilov, and O. Rader, "Ultrafast spin-polarization control of Dirac fermions in topological insulators," *Phys. Rev. B*, vol. 93, p. 155426, Apr 2016.

[165] J. Mauchain, Y. Ohtsubo, M. Hajlaoui, E. Papalazarou, M. Marsi, A. Taleb-Ibrahimi, J. Faure, K. A. Kokh, O. E. Tereshchenko, S. V. Eremeev, E. V. Chulkov, and L. Perfetti, "Circular dichroism and

superdiffusive transport at the surface of BiTeI," *Phys. Rev. Lett.*, vol. 111, p. 126603, Sep 2013.

[166] S. Ulstrup, A. G. c. v. a. c. Čabo, D. Biswas, J. M. Riley, M. Dendzik, C. E. Sanders, M. Bianchi, C. Cacho, D. Matselyukh, R. T. Chapman, E. Springate, P. D. C. King, J. A. Miwa, and P. Hofmann, "Spin and valley control of free carriers in single-layer WS_2," *Phys. Rev. B*, vol. 95, p. 041405, Jan 2017.

[167] R. Bertoni, C. W. Nicholson, L. Waldecker, H. Hübener, C. Monney, U. De Giovannini, M. Puppin, M. Hoesch, E. Springate, R. T. Chapman, C. Cacho, M. Wolf, A. Rubio, and R. Ernstorfer, "Generation and evolution of spin-, valley-, and layer-polarized excited carriers in inversion-symmetric WSe_2," *Phys. Rev. Lett.*, vol. 117, p. 277201, Dec 2016.

[168] N. Smith, "Image states, surface states and inverse photoemission," *Physica Scripta*, vol. 1987, no. T17, p. 214, 1987.

[169] T. Fauster and W. Steinmann, "Two-photon photoemission spectroscopy of image states," *Electromagnetic Waves: Recent Developments in Research*, vol. 2, pp. 347–411, 1995.

[170] Y. Cao, J. Waugh, X. Zhang, J.-W. Luo, Q. Wang, T. Reber, S. Mo, Z. Xu, A. Yang, J. Schneeloch, *et al.*, "Mapping the orbital wavefunction of the surface states in three-dimensional topological insulators," *Nature Physics*, vol. 9, no. 8, p. 499, 2013.

[171] N. Munisa, E. E. Krasovskii, Y. Ishida, K. Sumida, J. Chen, T. Yoshikawa, E. V. Chulkov, K. A. Kokh, O. E. Tereshchenko, S. Shin, and A. Kimura, "Ultrafast dynamics of an unoccupied surface resonance state in Bi_2Te_2Se," *Phys. Rev. B*, vol. 97, p. 115303, Mar 2018.

[172] J. A. Sobota, S.-L. Yang, D. Leuenberger, A. F. Kemper, J. G. Analytis, I. R. Fisher, P. S. Kirchmann, T. P. Devereaux, and Z.-X. Shen, "Distinguishing bulk and surface electron-phonon coupling in the topological insulator Bi_2Se_3 using time-resolved photoemission spectroscopy," *Phys. Rev. Lett.*, vol. 113, p. 157401, Oct 2014.

[173] S. Mathias, S. Eich, J. Urbancic, S. Michael, A. Carr, S. Emmerich, A. Stange, T. Popmintchev, T. Rohwer, M. Wiesenmayer, *et al.*, "Self-amplified photo-induced gap quenching in a correlated electron material," *Nature communications*, vol. 7, p. 12902, 2016.

[174] M. Hellgren, J. Baima, R. Bianco, M. Calandra, F. Mauri, and L. Wirtz, "Critical role of the exchange interaction for the electronic structure and charge-density-wave formation in $TiSe_2$," *Physical review letters*, vol. 119, no. 17, p. 176401, 2017.

[175] T. Limmer, J. Feldmann, and E. Da Como, "Carrier lifetime in exfoliated few-layer graphene determined from intersubband optical transitions," *Physical review letters*, vol. 110, no. 21, p. 217406, 2013.

[176] K. Sugawara, Y. Nakata, R. Shimizu, P. Han, T. Hitosugi, T. Sato, and T. Takahashi, "Unconventional charge-density-wave transition in monolayer 1T-$TiSe_2$," *ACS nano*, vol. 10, no. 1, pp. 1341–1345, 2015.

[177] J. van Wezel, P. Nahai-Williamson, and S. S. Saxena, "Exciton-phonon-driven charge density wave in $TiSe_2$," *Phys. Rev. B*, vol. 81, p. 165109, Apr 2010.

[178] P. Chen, Y.-H. Chan, X.-Y. Fang, S.-K. Mo, Z. Hussain, A.-V. Fedorov, M. Chou, and T.-C. Chiang, "Hidden order and dimensional crossover of the charge density waves in $TiSe_2$," *Scientific reports*, vol. 6, p. 37910, 2016.

[179] E. Möhr-Vorobeva, S. L. Johnson, P. Beaud, U. Staub, R. De Souza, C. Milne, G. Ingold, J. Demsar, H. Schäfer, and A. Titov, "Nonthermal melting of a charge density wave in $TiSe_2$," *Physical review letters*, vol. 107, no. 3, p. 036403, 2011.

[180] J. Feng, D. Biswas, A. Rajan, M. D. Watson, F. Mazzola, O. J. Clark, K. Underwood, I. Markovi, M. McLaren, A. Hunter, D. M. Burn, L. Duffy, S. Barua, G. Balakrishnan, F. Bertran, P. Le Fevre, T. Kim, G. van der Laan, T. Hesjedal, P. Wahl, and P. D. King, "Electronic structure and enhanced charge-density wave order of monolayer VSe_2," *Nano Letters*, no. 10.1021/acs.nanolett.8b01649.

List of Figures